Catalysis of Neurotransmitter Release is a Target of Alzheimer's Disease: Etiologic Mechanism and Novel Therapeutic Potential

by
Daniel Jack Adams
B.A., Clark University, 2007

A thesis submitted to the
Faculty of the Graduate School of the
University of Colorado in partial fulfillment
of the requirement for the degree of
Doctor of Philosophy
Department of Molecular Cellular and Developmental Biology
2013

This thesis entitled:

Catalysis of Neurotransmitter Release is a Target of Alzheimer's Disease:
Etiologic Mechanism and Novel Therapeutic Potential

written by Daniel Jack Adams

has been approved for
the Department of Molecular Cellular and Developmental Biology

_____

Professor Harald J. Junge Ph.D.
(Thesis Committee Chair)

_____

Professor Michael H. B. Stowell Ph.D.
(Thesis Advisor)

Date_____

The final copy of this thesis has been examined by the signatories, and we
Find that both the content and the form meet acceptable presentation
standards
Of scholarly work in the above mentioned discipline.

ABSTRACT

Adams, Daniel Jack (Ph.D., Molecular Cellular and Developmental Biology)

Catalysis of Neurotransmitter Release is a Target of Alzheimer's Disease: Etiologic Mechanism and Novel Therapeutic Potential

Thesis directed by Professor Michael H. B. Stowell Ph.D.

Alzheimer's disease is a devastating neurodegenerative syndrome that afflicts tens of millions of patients worldwide for which no effective therapy or prevention currently exists. Although the disease mechanisms remain elusive, it is clear that the 42 amino acid ß-amyloid peptide is of central importance. The present work has combined structural, biochemical and *in vivo* analyses to uncover a catalytic role for the major synaptic vesicle protein synaptophysin in neurotransmitter release. We have found that this catalytic activity is directly targeted and inhibited by the ß-amyloid peptide causing synaptic dysfunction early in the progression of Alzheimer's disease. The novel method developed to analyze neurotransmitter release kinetics at individual synapses constitutes a significant improvement in sensitivity, accuracy and reproducibility over currently popular methods. Finally, biophysical studies were carried out to isolate and characterize truncated synthetic byproducts of ß-amyloid which inhibit its aggregation dynamics and neurotoxicity, leading to the identification of two candidates showing great promise as therapeutic agents in the fight against Alzheimer's disease.

DEDICATION

I took my first biology course in 9th grade with Steve Roderick. It was his passion for biology that inspired my original interest in the subject. In his class, learning about the molecular mechanisms of DNA replication, I realized that I wanted to continue on in molecular biology to uncover more about the basic mechanics of life. I dedicate this thesis to Mr. Roderick and other great teachers like him who inspire young minds on a daily basis.

ACKNOWLEDGEMENTS

I have received great support from many individuals and organizations who have made the work presented in this thesis possible, and I wish to express my gratitude here. In addition to general acknowledgements, I have included a section at the end of each chapter to indicate the specific contributions to data I present by individuals other than myself.

I'll start by acknowledging funding support I enjoyed from two sources. Firstly, the peptide project presented in chapter 4 was supported by funding from the Corden Pharma Peptide Research grant. I was also supported by the CU-NIH Molecular Biophysics pre-doctoral training grant which not only provided financial support but was an excellent training program in the discipline of biophysics and provided a rich interdisciplinary community for me to share my work with.

I'd like to thank AmideBio for supplying Aß42 peptide, sharing analytical equipment and technical assistance with handling the peptide.

My first 3 years in MCDB were spent working in the laboratory of Tom Blumenthal. I found the lab to be a nurturing environment in which to begin my scientific training. I greatly appreciate the support and friendship of all the scientists I had the pleasure of working with there. In particular I appreciate Tom's shrewd eye for understanding data and his generally candid demeanor, and I will always fondly remember the time I spent in his lab.

The administrative staff of MCDB is a fantastic team of individuals who make all the work we do possible and I'd like to acknowledge their efforts in particular I'd like to thank Kathy Lozier, Karen Brown and Lee Gutmacher who are always a pleasure to interact with and to so much work behind the scenes to make MCDB run smoothly. Additionally I'd like to thank Erik Hedl and Jen Ryan for their friendship and assistance with various matters during my time in MCDB. There were many labs in MCDB and elsewhere that provided invaluable help by sharing equipment and reagents with me and I'd like to thank them all.

Early during my tenure in Michael Stowell's lab I was doing a lot of electron microscopy work and had the pleasure of working with genuine experts who both provided excellent technical training and were just extremely nice people. I would like to particularly thank Eileen O'toole, Cindy Schwartz, Tom Giddings and especially Mary Morphew who is truly a wizard of electron microscopy.

I enjoyed a number of collaborative efforts with individuals I'd like to thank now. In the Neuroscience department I'd like to thank Tim Chapman, Giuseppe Cortese and Susan Patterson for fun collaboration on a number of small projects. I'd like to thank John Mayer formerly of Lilly Pharmaceuticals, Travis Nemkov formerly of Amidebio and Christopher Ebmeier formerly of the biochemistry department for help with my work on the Aß42 peptide. I enjoyed working with Domenico Galati, a classmate in MCDB, on a variety of projects several of which bore extremely interesting and useful data. I found his scientific rigor inspiring and always appreciated his feedback and advice on my work. I'd like to thank Martha

Bodine, Robert McLoed, Chris Roath and Victor Bright for a fun and eye-opening collaboration on a project designing patterned arrays of neurons for stimulation and recording.

I owe a great deal to the members of Michael Stowell's lab who provided a great environment in which to do science. In particular, Duncan Laverty, Nilanjan Ghosh, Chris Arthur and Stephen Eisenberg all made significant contributions to the work presented here. I would also like to thank Kerri Ball, Kelly Grounds, Dada Pisconti, James Mapes, Arieann DeFazio, Tamara Basta, Taylor Mills, Paula Roberts, Gretchen Stein, Ray Wu and John Caruthers for helpful discussions and camaraderie during my time in the lab.

I will always appreciate the support and guidance from my thesis committee: Michael Klymkowsky, Harald Junge, Marv Caruthers and Bob McLoed. Thank you for being critical and pushing me to do the right experiments and for the time and effort you gave in committee meetings, reading my thesis to help me through this process.

Finally I would like to express my great appreciation for the mentorship I enjoyed from Michael Stowell. Working in your lab has been a very fun experience. As I generated new data, the sessions at the chalk board drawing up ideas to make sense of them will always be a fond memory of the way science should be done. I thank you for taking me into your lab and giving me an opportunity to work on exciting questions. Your enthusiasm for the work and constant flow of new ideas

and approaches was truly an inspiration to me and I appreciate the latitude you gave me to take those suggestions (or not).

I'd like to end by thanking my friends and family whose support made it possible for me to complete this work. In particular I thank my wife Joey for her patient support and companionship through this process.

CONTENTS

TABLES

FIGURES

CHAPTER 1: INTRODUCTION

SYNAPTIC VESICLE LIFE CYCLE AND FUSION

The central and peripheral nervous systems found in virtually all metazoan organisms are required for basic biological activities like locomotion, circulation and respiration as well as more complex and subtle functions such as memory, computation and emotion. These systems are intricate networks of specialized cells which meet at well conserved, highly polarized and remarkably stable structures known as synapses. The number of neurons in a mammalian brain ranges from the tens of millions in rodents up to tens of billions in humans[1] and contains as many as ~5×10^{14} synapses[2] as well as a few glial cell types found in similar numbers to neurons[3]. Neurons are electrically active cells which utilize ion channels, exocytic vesicles and extracellular receptors to propagate a series of voltage and ligand based signals throughout their network. These signals are in turn responsible for the gross functions of the nervous system and it is generally the goal of neuroscience to understand how these discrete molecular events sum to the complex traits observed on the organismal and behavioral scale.

Neurons generally signal to each other through all-or-none depolarization events known as action potentials. Through mechanisms that are not fully understood a complex set of excitatory and inhibitory inputs are integrated into a single coherent stereotyped response wherein a wave of opening Na^+ channels allows influx of the positive ions to momentarily reverse the resting membrane

potential in a chain reaction that propagates down the length of the axons to their termini at the boutons or presynaptic terminals. When this wave reaches the synapse, voltage-gated ion channels are opened to allow influx of Ca^{++} ions which in turn cause release of neurotransmitter into the synaptic cleft. The postsynaptic membrane contains ligand-gated ion channels which are opened by the binding of neurotransmitter resulting in postsynaptic potentials that make either excitatory (depolarizing) or inhibitory (hyperpolarizing) contributions to firing outcome of the postsynaptic cell.

Neurotransmitter release is carried out by small trafficking organelles known simply as synaptic vesicles. Synaptic vesicles have a highly uniform structure and a carefully regulated lifecycle (Figure 1) which allows them to efficiently perform this essential function. Synaptic vesicles are 40 nm spheres and their membranes are densely packed with a collection of resident membrane proteins and highly enriched in the sterol lipid cholesterol. The synaptic vesicle life cycle begins with the acidification of the lumen driven by a V-type ATPase. The proton gradient across the vesicular membrane is used to drive the loading of neurotransmitter through specific channels. There are many different types of neurotransmitters but each synapse tends to be specific for a particular neurotransmitter molecule. In each synapse the relevant neurotransmitters are loaded from the cytoplasm into the lumen of the synaptic vesicles where they are packaged at high density. Once loaded with their cargo, the synaptic vesicles are trafficked to an area of the presynaptic membrane known as the active zone. At the active zone, synaptic

vesicle proteins that extend from the surface dock with a protein scaffold on the plasma membrane where they are prepared for fusion in a process known as priming. The docked and primed vesicles are then described as readily releasable only awaiting the influx of Ca^{++} ions. The synaptotagmin proteins then activate fusion upon binding to calcium via their C2 domains. Like many other membrane fusion events in the cell, synaptic vesicle fusion is mediated by soluble NSF attachment protein receptor (SNARE) proteins. SNARE proteins on the vesicle (v-SNAREs) interact with SNAREs on the target membrane (t-SNAREs) in a tight coiled-coil four-helix bundle. The energy released by this bundling is believed to be responsible for initiating the lipid flipping required to initially open a fusion pore to join the two juxtaposed bilayers. As soon as the fusion pore is opened, the densely packed cargo of neurotransmitter molecules are released into the synaptic cleft where they bind their cognate receptors on the post-synaptic cell. It is believed by some that vesicles can re-close the fusion pore and be directly recycled back for reloading in a process known as kiss-and-run fusion. According to the competing model known as full fusion, the vesicle fuses fully with the plasma membrane. Following full fusion, the synaptic vesicle membrane and protein components are recovered from the plasma membrane by clathrin-mediated endocytosis. These endosomes then undergo maturation and are prepared for acidification and neurotransmitter loading again.

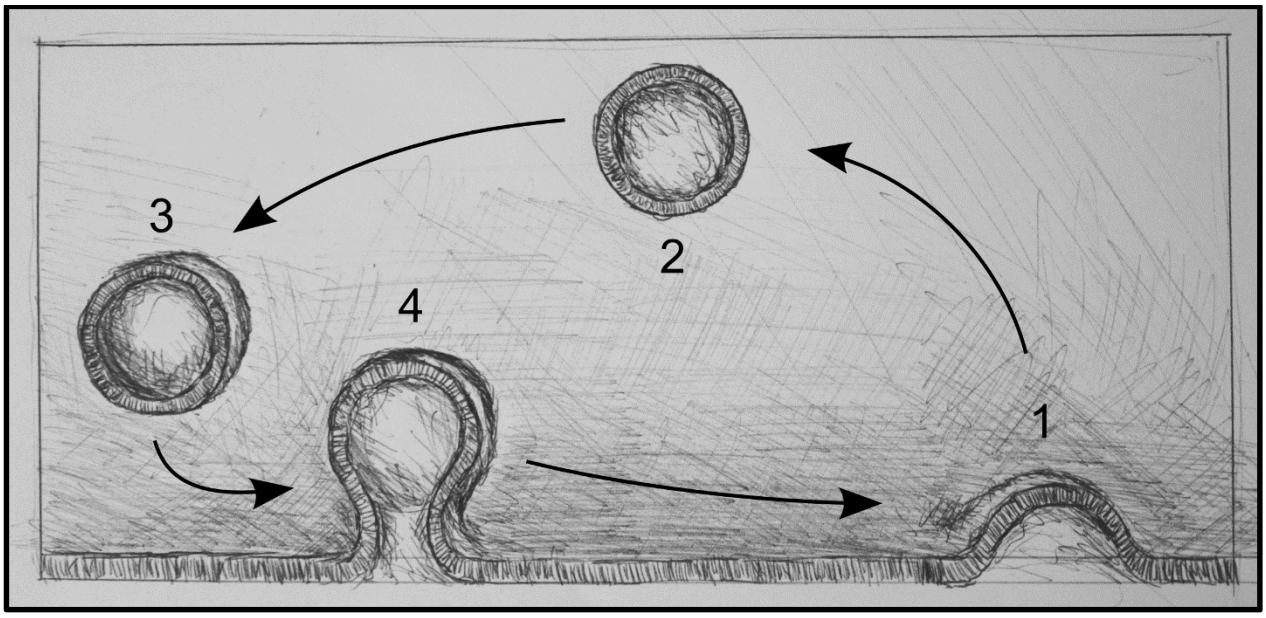

Figure 1: Synaptic Vesicle Cycle
Vesicles cycle from clathrin-mediated endocytosis (1) through maturation and cargo loading (2), docking/priming (3) and calcium mediated fusion (4).

The exact biophysical mechanisms of synaptic vesicle fusion are still the subject of intense investigation, but many important details have already been described. Docking and priming involves interaction of the v-SNARE synaptobrevin2 (VAMP2), with the t-SNAREs syntaxin-1 and SNAP-25 in a 1:1:1 stoichiometry assisted by accessory proteins Munc18, Munc13, RIM, complexin and the calcium sensor synaptotagmin. It is believed that Munc18, complexin and synaptotagmin participate in stalling the zippering of the SNARE domains until calcium triggering which then shifts those proteins into conformations that allow and promote complete winding of the SNAREs into a tight four helix bundle. The energy derived from the exothermic SNARE coiling[4] is believed to be responsible for overcoming the electrostatic barrier faced in flipping lipid tails through the

cytoplasm to first join the outer leaflet of the vesicle with the inner leaflet of the plasma membrane forming the hemifused intermediate and subsequently the mirrored process of joining the inner leaflet of the vesicle with the outer leaflet of the plasma membrane to open the fusion pore. The many players in this complex process are not randomly distributed in their respective membranes but rather they are spatially organized into micro-domains to allow efficient progression of fusion. Syntaxin-1 is found in many stages of clustering dependent on cholesterol which provides a vesicle docking site to ensure multiple trans-snare interactions can form which is necessary for the fast physiologic fusion kinetics observed. The presence of ordered syntaxin-1 arrays on the plasma membrane predicts that a similar analogous structure may exist to organize VAMP2 in the vesicle prior to docking and fusion. It has been suggested that the major synaptic vesicle protein synaptophysin serves to cluster many copies of the v-SNARE[5] however this model remains untested.

SYNAPTOPHYSIN

Due to its high abundance and ubiquitous expression in presynaptic terminals, synaptophysin was one of the first synaptic proteins identified and studied, however despite many years of research, to many it is still regarded simply as a marker protein with no biochemical function. The very first work on synaptophysin identified that it was highly expressed at presynaptic terminals in the central nervous system (brain and spinal cord), neuromuscular junction and

retina as well as the adrenal medulla[6] and that it was quite specific to synaptic vesicles[7]. It was also observed to be glycosylated which was later shown to occur on a luminal loop at asparagine 53 and was important for its localization[8]. Subsequent work on synaptophysin uncovered tyrosine phosphorylation on the cytoplasmic c-terminal tail which may function in vesicle cycling[9]. The four-pass integral membrane protein exists as a four-helix bundle which has a hexameric quaternary structure that resembles a channel pore[5]. Indeed purified synaptophysin was reconstituted into a membrane and a conductance was measured leading to the hypothesis that the protein served as a neurotransmitter channel[10].

Despite extensive description of the physical characteristics of synaptophysin, the function of this protein has remained controversial and unclear since its discovery. The strongest evidence that led to the belief that synaptophysin was non-functional came from a genetic null mouse. The knockout mouse had no overt phenotype in development, behavior, synaptic structure and apparent function[11]. These findings have been difficult to reconcile with the fact that synaptophysin is highly conserved in vertebrates (>75% identity) with a recognizable homolog in nematodes[12] and constitutes ~10% of the mass of the synaptic vesicle proteome[13]. The most parsimonious explanation to arise from the literature to date points to the presence of redundant homologs which can substitute for synaptophysin in its absence[14,15], but these data fail to pinpoint the exact biochemical function of the protein. Gross behavioral phenotypes were eventually observed in the synaptophysin knockout mouse[16] but it wasn't until recently that a cellular level

defect was reported[17]. Synaptophysin null neurons displayed a modest deficiency in endocytosis during and after neuronal stimulation suggesting that the protein functions in vesicle recovery at several phases of activity.

It has long been known that synaptophysin physically interacts with VAMP2 in synaptic vesicles[18], but the implications of this association were not immediately apparent. Several studies have demonstrated that synaptophysin binding is mutually exclusive with assembly of VAMP2 into the SNARE complex[18,19] but the mechanism that underlies this observation is still unknown. This suggests that the interaction is not related to the fusion event but by no means rules out that possibility. New evidence indicates that synaptophysin is important for loading VAMP2 into endosomes to recover it into the synaptic vesicle pool[20]. This activity could explain the lapse in endocytosis kinetics attributed to synaptophysin depletion because retrieval of VAMP2 seems to be a limiting step in the process[21,22]. VAMP2 lacks a recognizable clathrin adapter AP2 recognition site suggesting that it requires another protein to load it into recycling synaptic vesicles. A number of putative cargo motifs were identified on the synaptophysin carboxy-termianl cytoplasmic tail further suggestive that it serves to ensure retrieval of VAMP2 during endocytosis[20,23].

The physin family of proteins, which appears to exhibit some measure of functional redundancy, is conserved across over 550 million years of evolution[12,24]. The selective pressure required to drive maintenance of a family of redundant proteins expressed at extremely high levels in such a tightly regulated cellular

compartment suggests that synaptophysin plays a critical role in a process indispensable for metazoan life. Despite recent advances proposing new functions for synaptophysin, none seem sufficient to explain its impressive evolutionary footprint, indicating that perhaps other more fundamental functions of the protein remain undiscovered.

METHODS FOR STUDY OF SYNAPTIC VESICLE DYNAMICS

Since synaptic vesicles were first observed by EM[25] and suggested to be the structural units correlating to quantal synaptic release[26], the nature of their dynamics in the nerve terminal has been of great interest. For decades improved electron histology allowed increasingly detailed physical description of the vesicles but still only allowed limited understanding of their dynamics. Because the small synapses of the hippocampus and cortex are relatively inaccessible to electrophysiological techniques, it wasn't until the 1990s, when optical tools were developed, that major progress in this area was made.

Because of the Abbe diffraction limit, traditional fluorescent microscopy cannot resolve individual synaptic vesicles (~40 nm). However, light microscopy provides an ideal tool for imaging pools of these organelles *in vivo* in real time. Under a standard fluorescent microscope, a single presynaptic terminal (hundreds of nanometers across although varying in morphology) containing a pool of labeled vesicles is easily resolved as a single fluorescent punctum. Styryl dyes such as FM 1-43 and genetically encoded pH-sensitive fluorescent proteins (known as

pHlourins) can both be used to label synaptic vesicles and reflect their dynamics as changes in fluorescent signal intensity. As with other live-cell fluorescent imaging techniques, both methods face the common challenge of balancing signal to noise considerations with phototoxicity and photobleaching effects. Signal to noise in a given sample is impacted by many factors, but is generally proportional to exposure time. Whereas fixed samples may be amenable to long exposure times, biologically meaningful temporal resolution of synaptic events in live cells may require integration times on the order of seconds or even milliseconds. Each fluorophore has an intrinsic property known as quantum yield (Φ) which is simply the ratio of photons emitted to photons absorbed. Because Φ is a constant, a simple way to increase the number of photons emitted by a sample per unit time is to apply more photons i.e. increase illumination intensity. Aside from the technical contstraints of the illumination source, the most common limitations encountered when increasing photon dosage to a living specimen are phototoxicity and photobleaching. The exact mechanisms of phototoxicity are controversial but the most probable explanation involves generation of reactive oxygen species that cause oxidative damage to the cellular machinery and may inhibit the biological processes being studied. However, phototoxicity is generally a more significant concern for long term imaging experiments on the order of hours and therefore less of a concern for study of synaptic events occurring on short time scales. Photobleaching is a stochastic decay process resulting from photochemical destruction of the fluorophore. Photostability is the intrinsic property of the fluorophore that determines the rate of

photobleaching in response to a given rate of photon absorption. The physical structure of a fluorophore determines both Φ and the photostability, so modified versions of fluorophores are often generated to improve these properties while maintaining the characteristic excitation and emission spectra. Beyond these common attributes, styryl dyes and pHlourins have unique and largely complementary benefits and limitations and are therefore frequently combined for study of synaptic vesicle dynamics.

Styryl dyes are linear molecules which contain several chemical moieties that give them their characteristic properties. Their amphipathic nature is essential to allow the dyes to partition between aqueous solution and the cellular membrane freely. Affinity for the bilayer is achieved by a tail of short branched hydrocarbon groups, however, two nitrogen cations prevent free diffusion through the membrane. The core of the molecule is a pair of aromatic fluorochromes conjugated by a bridge of one or more ethene linkers. A dramatic increase in quantum yield is observed upon insertion into the membrane which provides low background signal for high contrast staining. By far, the most popular styryl dye has been FM 1-43 followed by some of its derivative dyes modified for spectral shifts or partitioning efficiencies.

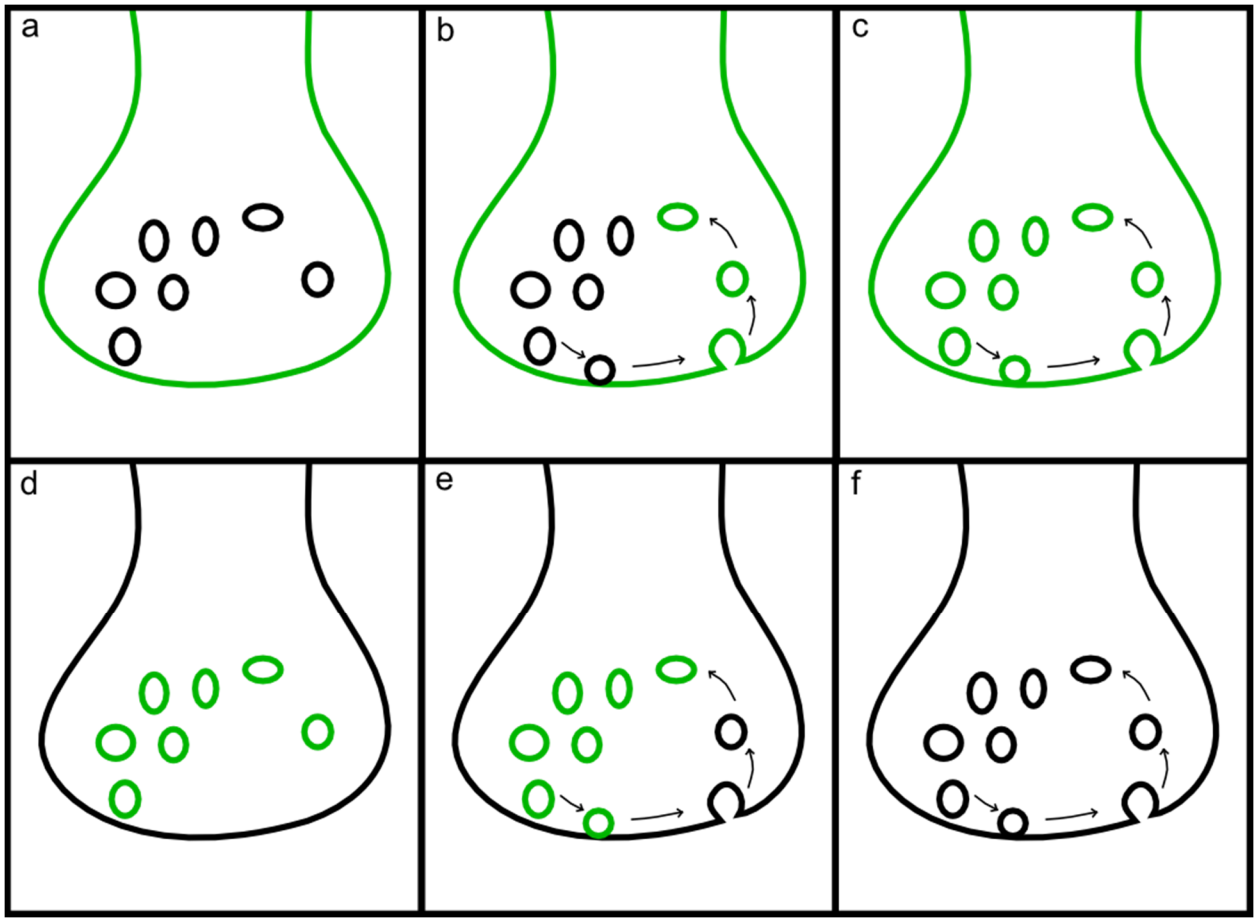

Figure 2: FM Dye Staining/Destaining Method
a, *FM dye is applied in the medium and binds to all external cellular membranes.* ***b and c,*** *Neurons are depolarized to induce endocytosis until readily releasable pool is loaded with labeled vesicles.* ***d,*** *Neurons are washed to remove dye which was not internalized.* ***e and f,*** *Neurons are again stimulated to induce release of pool of labeled vesicles until none remain.*

Styryl dyes are readily dissolved into medium and applied directly to living preparations of cells or tissue and are immediately adsorbed to all lipid membranes (Figure 2a). To specifically load synaptic vesicles, the sample is stimulated to fire action potentials in the presence of dye. These stimulated release events are coupled to endocytosis and recycling of synaptic vesicles. As vesicles are recycled from the

exterior membrane, they incorporate molecules of the dye (Figure 2b). When stimulation ceases, the plasma membrane can be washed of dye and only the internalized dye remains (Figure 2d and Figure 3). To observe the dynamics of exocytosis, the sample is again stimulated (Figure 2e). The dye is at high concentration in the vesicle and is therefore visible above background, however when stimulation is applied, labeled vesicles fuse with the membrane and the dye diffuses throughout the plasma membrane and extracellular solution which results in a loss of intensity in the punctate staining of each terminal (Figure 2f). It is this change in signal over time that can be used to deduce the dynamics of pools and thus individual vesicles during the destaining event. With neuronal preparations, this procedure is specific for synaptic vesicles although the dyes are used widely in other systems to study other endocytic compartments.

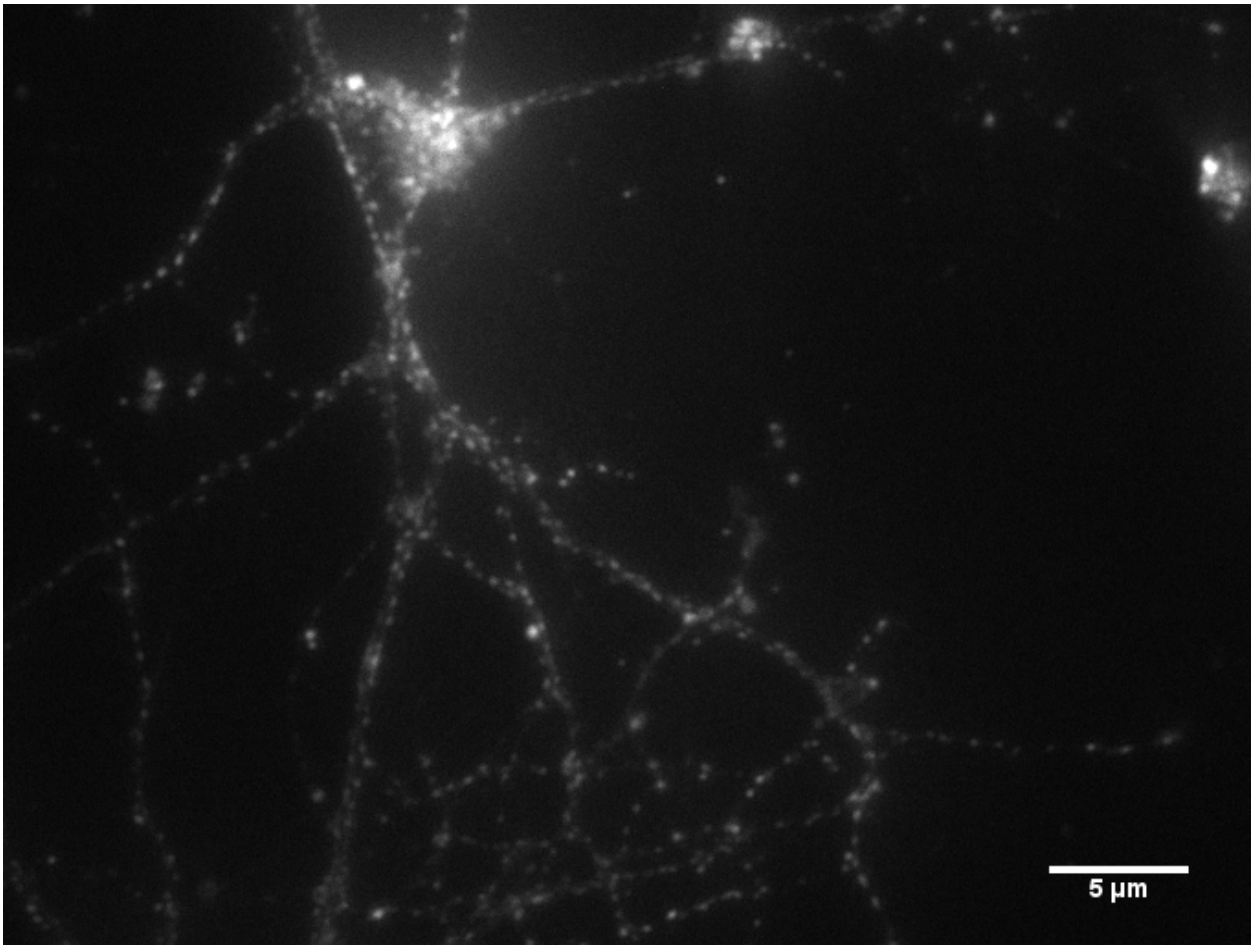

Figure 3: FM 1-43 Loaded Neuron
The standard punctate appearance of FM 1-43 staining of a hippocampal neuron.

FM 1-43 was first used to label vesicle pools at the ranine neuromuscular junction and observe unloading dynamics[27,28]. It has since been widely used to observe both endocytic and exocytic pathways in many systems and remains one of the best ways to study synaptic vesicles. FM dye loading/unloading has a few unique advantages that make it well suited to many experimental questions. FM staining and washing can be accomplished in minutes making it a very fast procedure and permitting rapid analysis of many samples. Because the dye binds

native cellular membranes, FM experiments can be performed without introduction of ectopically expressed tagged proteins. It is often difficult to control protein levels in overexpression systems so the ability to avoid genetic manipulation of the sample can avoid artifactual results. Because the FM dye labels all membranes contacted by the medium, the entire sample becomes evenly labeled during a loading experiment. This is advantageous for experiments requiring comprehensive labeling as compared to labeling with transfected markers which are typically sparse. The nature of styryl dyes is that they primarily label actively cycling vesicles in the readily releasable pool which are collected at or near the active zone in a presynaptic bouton. Experiments concerned with synaptic vesicle dynamics most typically focus on vesicles in the terminal so this specificity represents an advantage over the traditional pHlourin-based system which selectively labels vesicle components during or after fusion with the plasma membrane but not throughout the rest of their lifecycle. This feature of styryl dyes also permits use of many different stimulation protocols. While the effects of single action potentials can be observed, FM dyes also enable imaging of bulk exocytosis induced by exhaustive depolarization such as long trains of stimulating bursts or bath application of hyperkalemic medium. Intensity of FM staining at a terminal gives a quantitative measure of the number of labeled vesicles present and destaining during stimulation provides a faithful correlate of synaptic currents measured by traditional electrophysiological techniques[29]. Because of this relationship, FM destaining can be used as a direct proxy for vesicular release and therefore allows

differential quantitative analysis of release kinetics at spatially discrete loci. Due to the popularity of FM 1-43 both in neuroscience and other areas of cell biology, a number of derivatives have been developed with altered properties. For example, modified fluorochrome chemistry has led to a red-shifted version of the dye known as FM 4-64 which allows dual labeling with another marker such as FITC or green fluorescent protein (GFP). Lengthened hydrophobic tails make FM 1-48 more lipophilic than FM 1-43. This results in altered membrane association kinetics which can be applied to quantify the exact timescales of membrane trafficking events. Finally, FM dyes with primary amine groups have been developed to allow chemical fixation of the dye after use in living cells. The fixable FM dyes are a powerful tool that has greatly facilitated retrospective analysis by enabling post-fix staining for markers of interest and correlating their distribution with dynamic events observed *in vivo*.

Despite their many benefits and wide popularity, styryl dyes suffer several key limitations. Because the entire cellular limiting membrane is stained during the loading phase, no real-time information is available regarding endocytosis. FM dyes are still used to quantify endocytosis efficiency by taking endpoint measurements, but are not well suited to acquisition of detailed kinetic and dynamics data. The requirement for a washout phase after loading also dictates a non-physiologic decoupling of exocytosis from endocytosis. This is effectively accomplished by washing in a calcium depleted buffer to attenuate spontaneous release of labeled vesicles, but requires several minutes before the preparation is suitably washed to

allow study of exocytosis. This decoupling makes FM experiments unideal for observing dynamics occurring in the transition from recently retrieved vesicles into the readily releasable pool. Once exocytosis has occurred and labeled vesicles are all released, imaging subsequent rounds of release would require the terminal to be re-loaded. This constraint makes FM dyes not well suited to experiments requiring many rounds of endocytosis and exocytosis. Practically, FM loading/unloading is typically only performed one or two times per sample.

Within only five years of the introduction of FM 1-43, a new and very different approach to imaging synaptic vesicle dynamics was developed[30], which was able to overcome some of the technical limitations of styryl dyes and extend the types of scientific questions that could be experimentally approached. Rather than labeling the membranes, the fluorochrome is targeted via direct translational fusion to resident synaptic vesicle proteins. The original construct, which is still widely used, consists of ecliptic GFP fused to the luminal end of the single pass transmembrane SNARE protein VAMP2 (synaptobrevin2) which was termed synapto-pHluorin. The so called 'ecliptic GFP' is one of a class of engineered GFP derivatives with a modified chromophore that display a dramatic but reversible attenuation of emission at 508 nm when protonated by exposure to acidic solution. This feature was developed to take advantage of the natural pH cycle that synaptic vesicles undergo (Figure 4). Immediately following endocytosis, recycling synaptic vesicles are rapidly acidified from pH 7.4 to pH 5.5. The lumen of the vesicle remains at pH 5.5 until fusion with the plasma membrane exposes the luminal

leaflet of the membrane to the synaptic cleft at pH 7.4. With ecliptic GFP targeted to the synaptic vesicle lumen, the fluorochrome is quenched while the synaptic vesicle is intact, and undergoes a massive increase in emission after exocytosis that is re-quenched upon subsequent endocytosis.

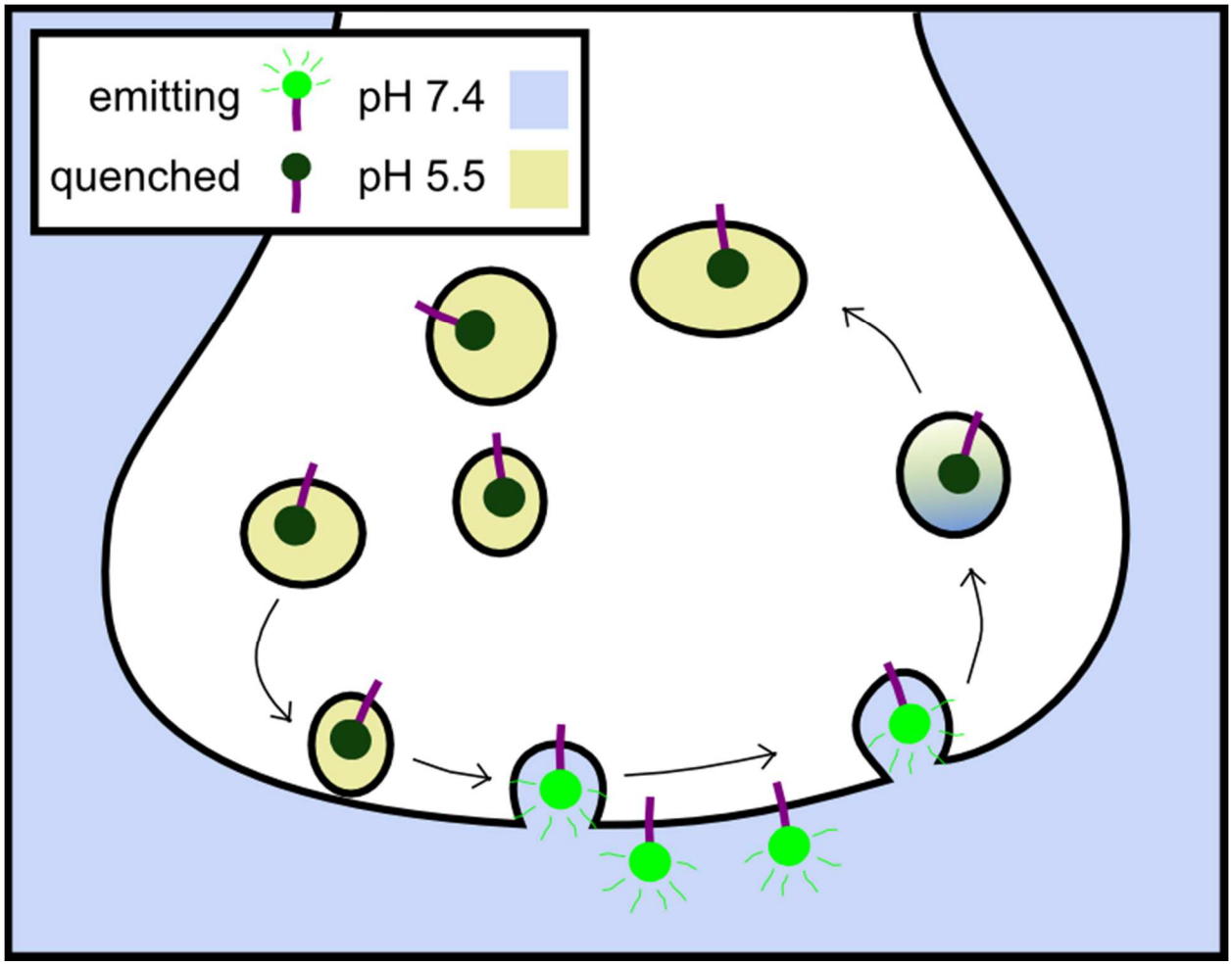

Figure 4: pHlourin Labeling
A schematic of a synaptic bouton where pHlourin molecules fluoresce brightly at pH 7.4 but are quenched in the synaptic vesicle lumen at pH 5.5.

One of the major advantages of the pHluorin probes over FM dyes is the ability to directly observe endocytosis kinetics. After a single action potential, a

rapid rise in signal can be observed as pHlourin molecules are exocytosed. This peak of signal then quenches back to the resting background level as the pHlourin probes are taken back up into vesicles which are then rapidly acidified. The ability to observe many rounds of coupled exocytosis and endocytosis events is another major advantage of pHlourin probes over FM-based methods. Because the pHlourin is tagged onto a specific protein, this technique allows dissection of the vesicle pool by resident protein. For example, it would be possible to determine if vesicles containing one protein of interest exhibit different dynamics from vesicles labeled with another protein. This type of experiment could determine if subpopulations of vesicles containing these different proteins exist and are differentially regulated. These types of experiments allow direct interrogation of the role specific proteins play in synaptic vesicle trafficking. A sometimes favorable feature of pHlourin experiments is the sparse labeling inherent to transfection of cultured neurons – the method typical for introduction of pHlourin probes. A particularly useful iteration of the original synapto-pHlourin takes advantage of a different pH-sensitive GFP derivative. Ratiometric GFP exhibits pH-dependent quenching of 508 nm emission when excited at 395 nm just as with ecliptic GFP. However, at low pH the ratiometric GFP shows a great increase in emission at 508 nm when excited at 475 nm[30]. Because of this property, ratiometric pHlourin probes permit visualization of intact vesicles while they are inside the bouton.

Although the genetically encoded nature of pHlourin probes has advantages, it also introduces several technical complications. Introducing recombinant DNA

into samples may be difficult or inefficient. For example, standard lipid-based transfection of cultured neurons rarely exceeds 25% efficiency. DNA can be introduced to e*x vivo* hippocampal slice cultures via biolistics and viral methods but these are difficult procedures that often require extensive optimization. Another caveat of protein overexpression is the difficulty of achieving a suitable expression level. A common problem seen in overexpressed proteins is mis-localization. In particular, synaptic vesicles have a highly regulated proteome and ectopic overexpression of one resident protein can alter native localization patterns of other synaptic proteins[31]. The other major limitation of pHlourin probes is that the signal generated by protein on the cell surface at neutral pH represents a convolution of signal increase from exocytosis and signal decrease from endocytosis. With a single action potential it is possible to separate these features, however, sustained stimulation provides only a noisy general increase in signal without much specific information about dynamics. This limitation has been partially overcome with the use of bafilomycin. Bafilomycin is a potent inhibitor of the ATPase family responsible for re-acidification of synaptic vesicles. Under acute treatment of bafilomycin, vesicles remain at pH 7.4 and therefore pHlourin signal accumulates with stimulation time providing a measure of exocytosis without convolution of endocytosis.

Since their introduction in the 1990s, FM dyes and pHlourin probes have become standard tools for analyzing synaptic vesicle dynamics. Each has unique advantages and limitations which has led many researchers to combine the two

approaches. Generally speaking, FM dyes are best suited to providing detailed kinetic information about exocytosis whereas pHlourins are most well suited to studying endocytic events.

ALZHEIMER'S DISEASE AND B-AMYLOID PEPTIDE

Alzheimer's disease (AD) is a neurodegenerative disorder characterized by progressive loss of nervous tissue; this loss occurs initially in the hippocampus and temporal lobe, however as the disease advances substantial wasting occurs in many brain regions[32,33]. Initial AD symptoms present as decreased recall of recently encoded memories; this deficiency progresses into more severe systemic memory loss, decline of many executive functions and eventually failure of motor and autonomic functions leading to death. The disease is aggressive, as symptomatic progression typically leads to death within less than 9 years of initial presentation[34]. AD accounts for 60% - 80% of cases of dementia[33] but is distinguished from other forms of cognitive decline by a unique histopathological signature. The behavioral symptoms of AD are varied and highly overlapping with other dementias, and definitive diagnosis can only be obtained by autopsy and examination of brain tissue for evidence of these distinctive pathologies[35]. Although diagnosis of AD is a rapidly growing field of study, the hallmarks of AD traditionally include two major features. The first of these features, known as senile plaques, are extracellular aggregates largely comprised of the short (36 – 43 amino acid) cleavage product of the amyloid precursor protein (APP) by ß and then γ

secretases; this peptide is commonly referred to as the amyloid ß peptide or simply Aß. The other important marker of AD is an intracellular structure known broadly as neurofibrillary tangles (NFTs). NFTs are also protein aggregates and they are composed of the microtubule binding protein tau in its hyperphosphorylated form. Intracellular accumulations of tau protein are also found in a family of other disorders known collectively as tauopathies, but nonetheless are an important part of AD diagnosis. Despite significant research efforts to link these pathologies to causal events and therapeutic targets, no effective treatment or preventative strategy for AD has yet been approved for clinical use.

AD is often broken into two categories based on a small number of important genetic markers[36]. Familial AD affects individuals with these rare alleles and typically confers extremely high risk of early disease onset (prior to age 60). However, the majority of AD cases (> 95%) are described as spontaneous because they lack any obvious genetic risk factors and typically present after age 65[37]. This means that for most AD cases, the only apparent major risk factor is advanced age. As life expectancy increases and improved prevention, diagnosis and treatment diminishes the prevalence of other leading causes of death, AD is a rapidly growing public health concern in industrialized nations. In fact, AD is now the 6th leading cause of death in the US afflicting an estimated 5.5 million patients[38]. Furthermore, these numbers are projected to grow significantly over the next 50 to 100 years[39,40]. In addition to a growing population of patients with this incurable disease, AD is somewhat unique in the burden it places on the community surrounding an afflicted

individual. As the patient loses cognitive abilities, friends and family often provide care at great financial and emotional cost to themselves. In addition to the $172,000,000,000 paid in health costs associated with care of patients suffering dementia in 2010, an estimated 12,500,000,000 hours of unpaid care were given by friends and family[37]. As healthcare policy makers and the general public alike become increasingly aware of these trends, the pressure to understand and cure AD grows ever higher.

The Aß peptide was proposed as causal in AD over 20 years ago[41], yet despite great progress in understanding, effective therapies against its effects are still lacking. The most dramatic data implicating Aß in AD comes from the two extreme genetic cases. Most of the mutations associated with early-onset familial AD are found in the proteins directly driving formation of the Aß peptide. These include mutations in APP that favor cleavage by ß secretase which prevents the normal physiologic cleavage by the α secretase, as well as mutations in the γ secretase complex which favor production of the more toxic 42-residue peptide (Aß42) over Aß40[42]. Additionally, because APP is harbored on chromosome 21, human patients with the relatively common aneuploidy for this chromosome, known as trisomy 21 or Down's syndrome, bear an extra copy of the APP gene. Although individuals with Down's syndrome typically have reduced lifespan, greater than 50% of those who do live into their 50s develop AD by that age[43]. These extreme examples of genetically driven overproduction of Aß42 causing severe disease progression helped to solidify the so called amyloid hypothesis based around this molecule. Further evidence came

from the ability to recapitulate many of the cellular, neurotoxic and behavioral phenotypes associated with AD in various Aß42-based models of the disease. Mice expressing human APP and/or PSEN1 bearing familial AD associated mutations develop loss of working spatial memory in a degenerative fashion[44]. Aß42 potently induces the AD-associated tauopathies in cultured neurons[45] and induces cell death[46]. For this reason, Aß42 is widely believed to be upstream of neurotoxicity caused by tau hyperphosphorylation. Direct application of Aß42 to acute hippocampal slices significantly impairs plasticity[47] and injection into rat brain causes cognitive defects specifically associated with AD pathology[48]. Cumulatively, these data have placed Aß42 as the central focus of research on the mechanisms of AD.

Initial hypotheses regarding the role of Aß42 in AD focused on the plaques because they were the visible hallmark of the disease. However, after hundreds of studies continued to find that plaques are not causal of disease symptoms, the target of inquiry shifted towards other forms of Aß42 peptide. Highly compelling amongst these findings was a study that showed very poor correlation between Aß42 plaque load and symptoms of dementia[49]. Aß42 is highly aggregation-prone and therefore technically challenging to work with, but a literature has emerged demonstrating that low order oligomers (dimers and trimers) are the bioactive disease-relevant species[50–60]. These forms of Aß42 can be isolated from patient brains or generated synthetically, and they potently recapitulate all of the symptoms of AD that can reasonably be observed under laboratory conditions from

altered plasticity[61] to frank neurotoxicity[62,63]. Once it had become clear that soluble Aβ42 oligomers were the disease-relevant toxin, the field moved towards trying to understanding what cellular processes and targets were directly impacted by the peptide.

Application of Aβ42 to a biological sample causes many changes but the major challenge in deriving mechanistic insights comes in distinguishing its primary effects and targets from secondary events induced by these primary changes. One approach to overcome this challenge has been to identify cellular proteins which physically interact with Aβ42 and therefore may be direct functional targets as well. Aβ42 contains several patches of highly hydrophobic residues which contribute to its propensity to self-aggregate, but also drive promiscuous hetero-oligomerization. Despite this promiscuity, several specific binding partners have been reported[64–66], and binding to NMDA receptors and perturbing glutamate trafficking[67] is only one of the many plausible mechanisms of Aβ42 toxicity that have been proposed in the literature. From these myriad studies, the salient conclusion is that Aβ42 is likely a pleiotropic effector of cellular dysregulation, and that it likely binds many different targets in different cellular compartments.

CHAPTER 2: ANALYSIS OF SYNAPTIC VESICLE RELEASE KINETICS

INTRODUCTION

Assays to analyze dynamics of synaptic vesicles are common tools for the modern neuroscientist. In particular, optical methods to measure the kinetics of synaptic vesicle release have grown in popularity especially FM dye unloading. While many elements of these methodologies have become optimized throughout their use, no standards exist for analysis of imaging, data and currently popular methods suffer several major shortcomings. These experiments are typically carried out using a monolayer of primary neurons grown on a substrate suitable for microscopy such as a coverslip. Once labeled, the synapses appear each as a single fluorescent punctum (Figure 3), however there is also frequently staining of other structures for various reasons depending on the sample and staining method. Faithful discrimination between signal contributed by real synapses and that from other sources is a non-trivial task of image processing, but is often accomplished in ways that result in overrepresentation of the real synapses (false positive identifications) and can introduce a number of biases for features such as staining intensity or synaptic density of the sample. Once synaptic puncta have been identified in an image, quantitative measurements are made to describe the dynamics. This is accomplished by a wide variety of methodologies, but most face the common challenge of deriving detailed information from a very large sample of

individuals and compiling that into meaningful, easily compared parametric data. A typical imaging experiment may have hundreds or thousands of synaptic puncta in a single field of view. Most studies of synaptic vesicle release determine the normalized change in fluorescence over time at each individual synapse, and average those values together to derive a single release curve to describe the kinetics of the entire sample. While effective, this technique ignores the biological heterogeneity inherent in the sample and therefore neglects a large amount of potentially informative data. The present work presents a method for analyzing synaptic release kinetics data which constitutes a significant improvement over current state-of-the-art techniques. This tool is simple and was built on an open-source platform to allow straightforward adoption by others in the hopes of encouraging more representative and reproducible analyses of these commonly used assays.

Generally, bona fide synaptic puncta stained with FM dye are identified as such by a characteristic morphology and dynamics. True synaptic puncta are typically between 0.5 μm and 5 μm and tend to be fairly circular. Healthy cells are firmly attached to the substrate, so the synaptic puncta should not move significantly during an unloading experiment which lasts only several minutes. Signals that increase during unloading or suddenly disappear are typically artifactual. Finally, non-specific FM staining of debris or internal cellular membranes other than synaptic vesicles generally will not respond to depolarizing stimuli whereas true synaptic puncta would be expected to. Thus, at the moment of

stimulation, genuine synaptic puncta should simultaneously undergo rapid decay of signal intensity while other puncta simply decay at the background rate of photobleaching (Figure 5). These criteria are typically imposed on the data in one of two ways. The first method is to simply examine the data by eye and manually select synaptic puncta; the second is to apply some type of automated computer-based image analysis tool.

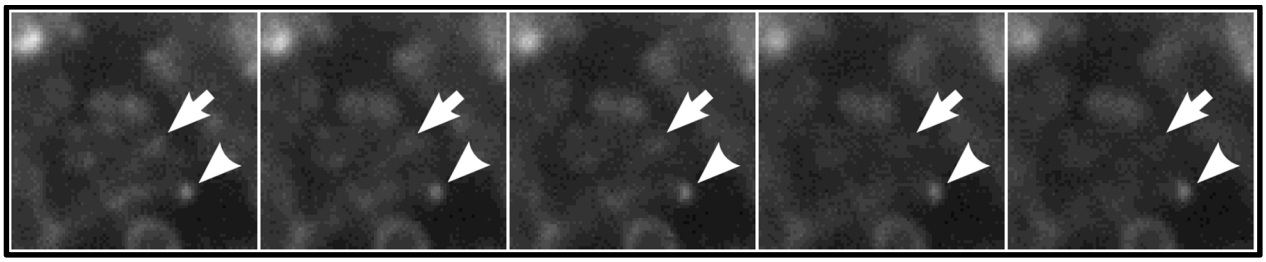

Figure 5: Synaptic Punctum Selection
True synaptic puncta (arrow) undergo rapid decay upon stimulation whereas non-synaptic particles (arrowhead) only decay at the slow rate of photobleaching. Each frame is 5 seconds of an unloading experiment.

The human eye is extremely adept at pattern recognition and threshold detection. These attributes make a trained human highly competent to simultaneously apply all of the morphological and dynamics criteria and identify true synaptic puncta with high fidelity. While this method produces an extremely low false positive rate, a major limitation is throughput. Exhaustive examination of every fluorescent punctum in a dataset is not technically feasible, and only selecting a subset can easily introduce sampling bias. Automated selection of sub-fields could help overcome this sampling bias but omission of many data points is still a significant drawback. Additionally, puncta that have poor contrast above

background may still contain biologically meaningful data but are not easily recognized by eye.

Automated methods of selecting synaptic puncta are quite varied but typically share several features. First, potential synapses are identified as high contrast local maxima and then the morphologic and dynamics criteria are applied. While extremely high signal to noise can be achieved, some preparations may have high background making automated threshold detection of puncta boundaries difficult. For this reason some type of background removal is often applied. To identify puncta, typical algorithms will look for a sudden steep (typically nonlinear) gradient of signal intensity along the X Y plane. A threshold point along such a gradient must be set manually to instruct the computer where to draw the border between signal and background. Once these parameters are set, the computer can automatically trace all regions where such a border exists. This set of regions of interest (ROIs) can then be further processed according to the criteria above.

One additional method of selecting true synaptic puncta exists but is not feasible in all cases and is technically challenging and time intensive and therefore not generally employed. This last method requires retrospective analysis of puncta that were analyzed in living cells. Once the unloading data is collected, the cells are fixed and stained for any of several presynaptic markers. During the retrospective imaging of the fixed synaptic markers, it is essential to find the exact same field of view imaged in the FM unloading experiment which can prove the most technically challenging part of the procedure. Use of fixable FM dyes can assist in aligning the

retrospective image with the original live-cell data, however these dyes exhibit poor staining intensity and specificity relative to their non-fixable analogs. Once the images are properly aligned, a colocalization method must be employed to determine which FM puncta are coincident with staining of synaptic markers. Although many options exist to accomplish this, the best methods typically determine a center of mass for the punctum identified in each image and determine if the two points fall within a certain radius (typically 0.1 – 0.5 μm) in 2 or 3 dimensional space depending on the type of image acquired. The other option to assist with image alignment is to rely on a genetically encoded fluorescent marker, but this introduces a number of complications and is not generally capable of dense labeling. Although it is technically challenging, this method provides the most robust and reliable identification of synaptic puncta and could be used to validate other methods as a benchmark.

IDENTIFICATION OF SYNAPTIC PUNCTA

Here, three methods of identifying synaptic puncta were employed on a sample dataset to provide objective comparison. The sample dataset was derived from B6 murine cortical neurons stained with FM 1-43 and unloaded by profusion with hyperkalemic medium (Figure 6). First, 350 elliptical ROIs were selected by an expert human accustomed to examining such data. Second, we applied a conventional automated puncta selection scheme of the type described above hereinafter refered to as the stringent method. Finally, a novel low-stringency

automated selection method, designed for use with *in silico* downstream particle filtering, was developed and applied to the dataset.

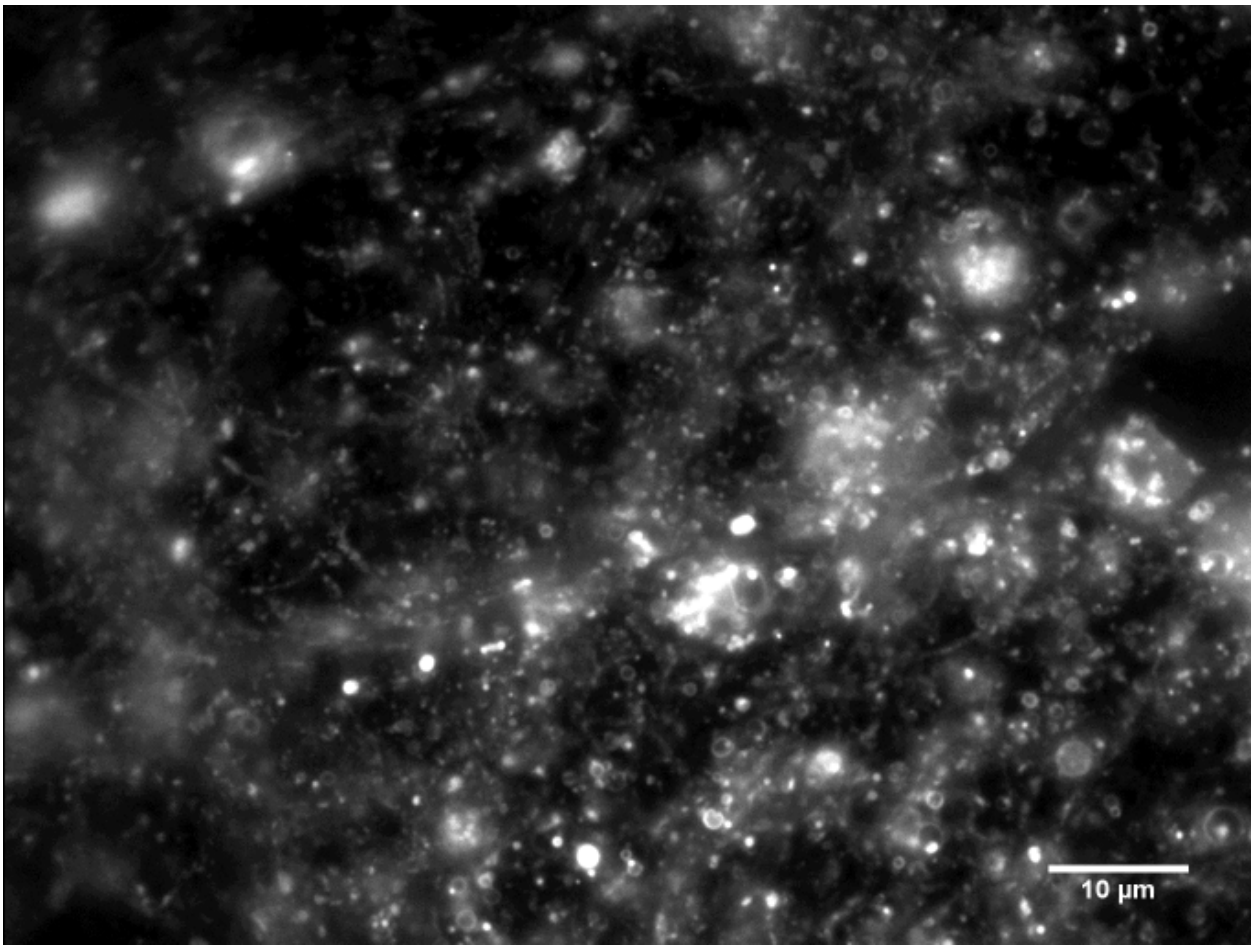

Figure 6: Sample Dataset
The first frame of the unloading sequence from the sample dataset used for this analysis was extracted and contrast was enhanced for clarity.

To manually select synaptic puncta, image contrast was enhanced and the movie was rapidly looped to facilitate the identification of genuine synaptic puncta which display the expected coordinated dynamics. An effort was made to select particles from across the entire field of view including both high and lower density

areas of the image. To the greatest extent possible, particles of varying initial intensity were selected. Heterogeneity in the exact release onset time and rate was apparent by eye, so effort was made to represent this range in particle selection. This selection method was capable of identifying 350 synaptic puncta (Figure 7) in approximately 90 minutes.

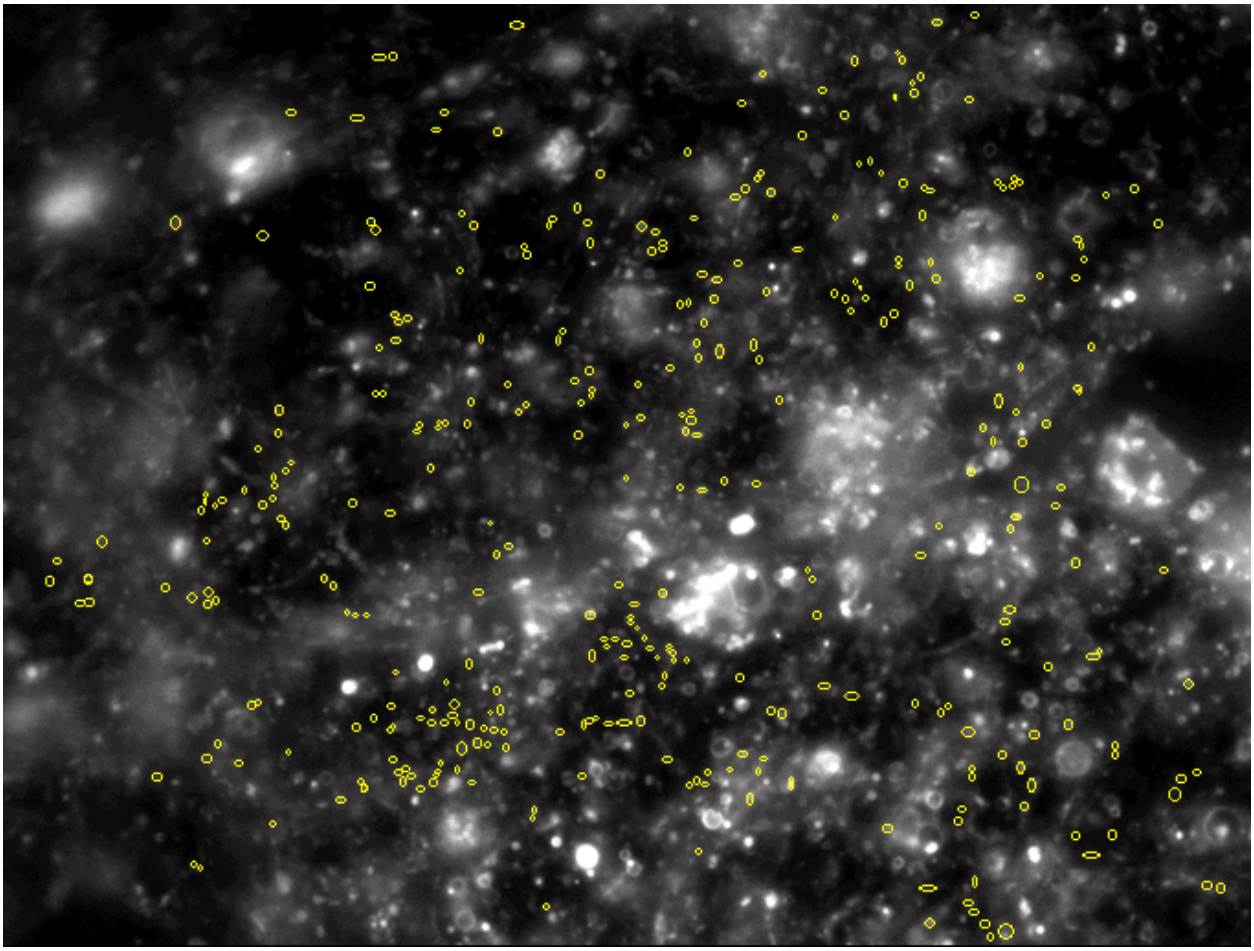

Figure 7: Hand-Picked ROIs
350 hand-selected ROIs outlined in yellow.

One conventional method for selecting regions of the image that change most over a short time is to perform a simple image subtraction. This approach was

applied in the stringent particle selection method. Signal still present immediately after the unloading event was subtracted from signal present at the beginning of the experiment. After this manipulation, only the most dynamic areas of the image remain. Several frames were captured prior to the beginning of unloading to establish a baseline bleaching rate. Floating debris that happens to be present in the first frame of unloading can be mistook for a synapse that rapidly unloads upon stimulation. To remove particles which traverse the field of view during the movie, all of the baseline frames were averaged to generate a starting image from which to select puncta. A rolling ball background subtraction was performed with a radius of 25 pixels (~385 px.). Finally the image was iteratively thresholded to yield a map of all local maxima which display the expected dynamics of a synapse. To apply the morphologic criteria, the ImageJ particle analysis tool was employed. Puncta in the thresholded image were selected from 2 – 200 pixels^2 to remove regions much larger than a typical synapse as well as single pixel noise. Additionally, a filter was applied to only allow selection of particles that were roughly circular ($4\pi(\frac{area}{perimeter^2}) > 0.5$). This highly automated process was capable of rapidly identifying 3819 synaptic puncta (Figure 8).

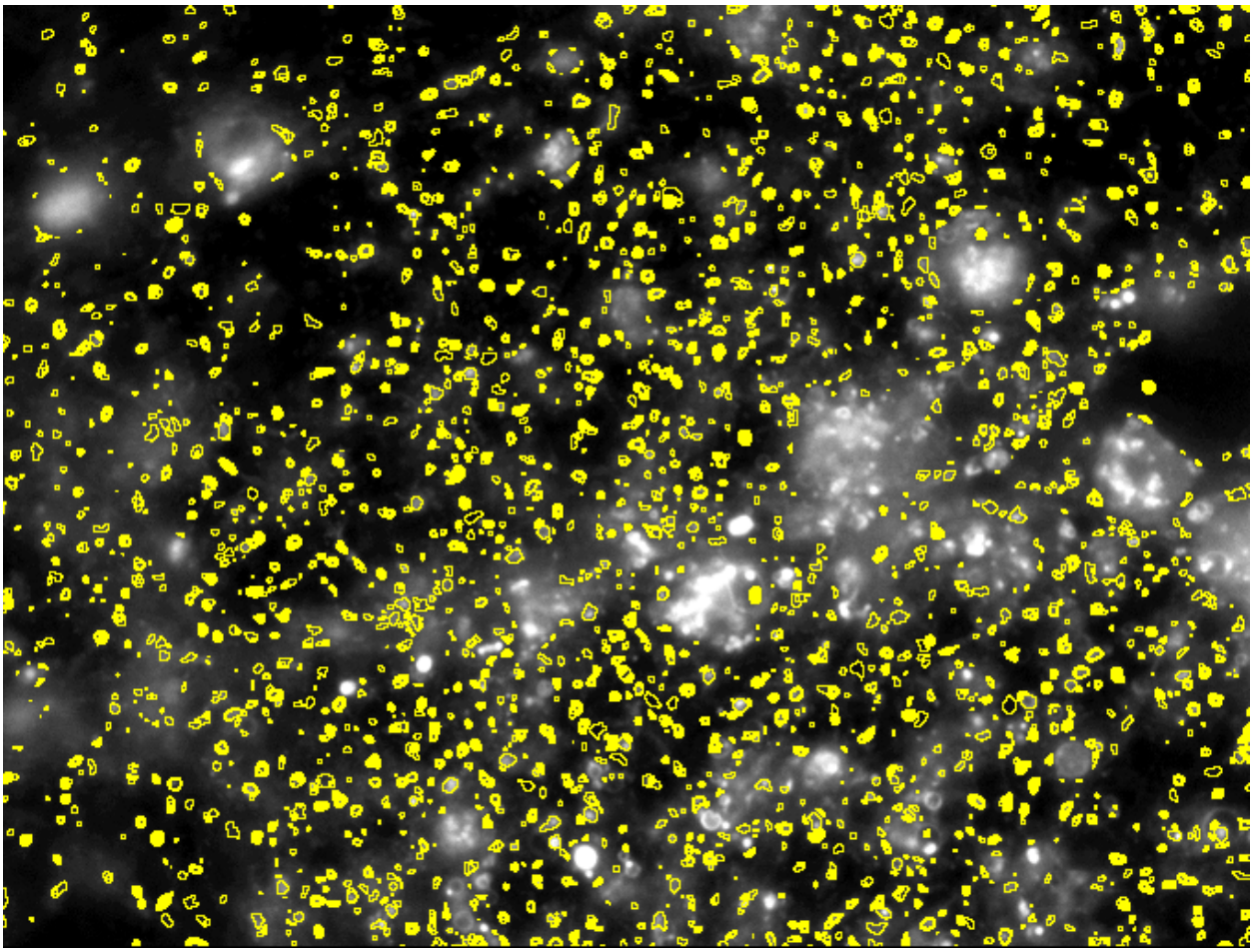

Figure 8: Conventional Automated ROI Selection
3819 synaptic ROIs selected by a conventional automated method outlined in yellow.

The more inclusive novel automated ROI selection tool was developed using the open source image analysis suite ImageJ[68]. In development of this tool, no attempt was made to filter out fluorescent particles on the basis of unexpected dynamics because they are removed in the subsequent analysis step. First, the unloading movie was flattened across time as a maximum Z projection to represent all particles present at any time during the experiment. Next, a standard background subtraction was applied which determines the mean gray value for the

whole image and subtracts half of that value from every pixel. The last step in the method finds local maxima and stores those positions as an ROI map. This method was able to identify 8565 fluorescent puncta (Figure 9) with minimal selectivity to mitigate omission of possible synaptic puncta.

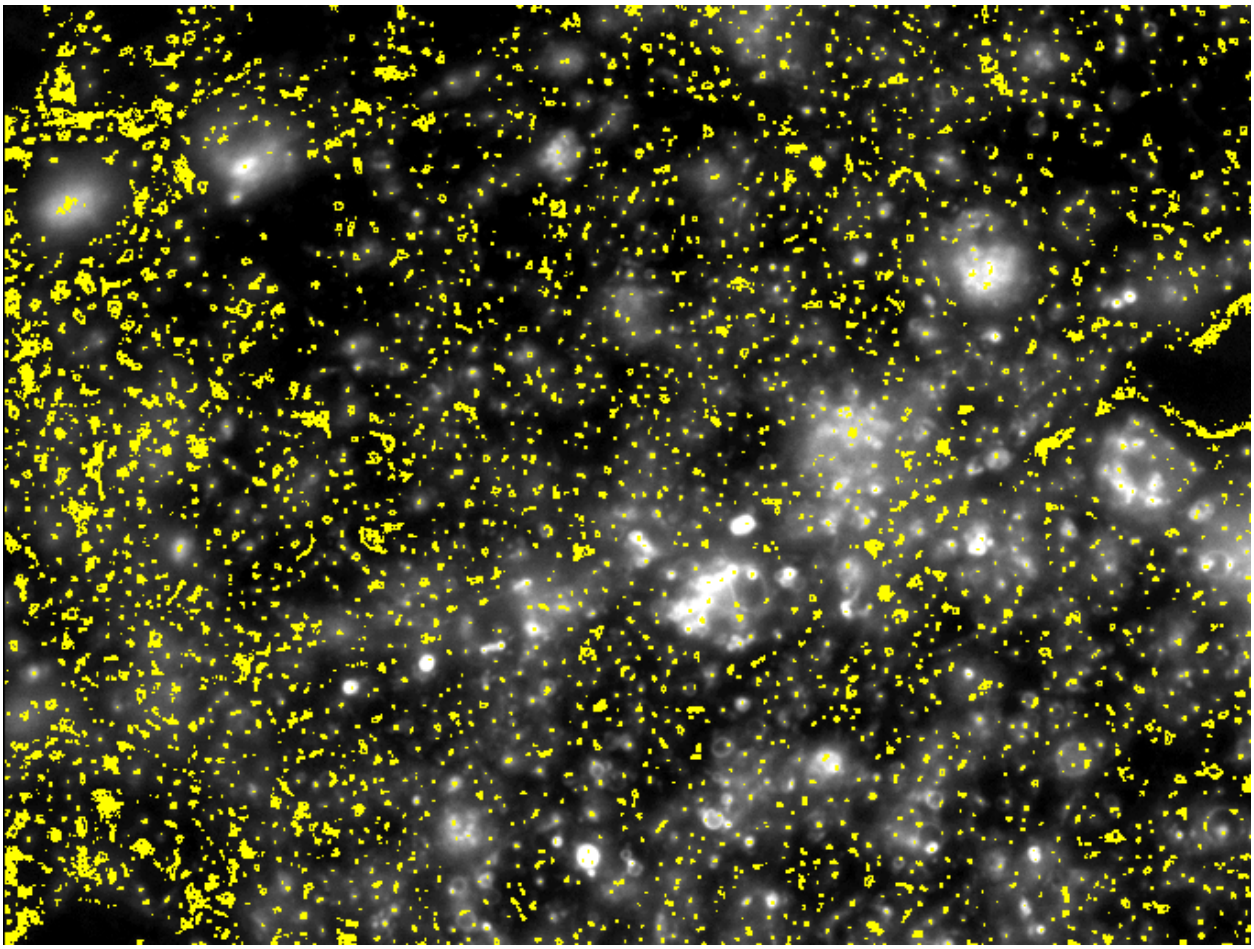

Figure 9: Inclusive Automated ROI Selection
8565 synaptic ROIs selected by novel highly inclusive automated method outlined in yellow.

METHODS FOR KINETIC ANALYSIS

A standard method for analyzing kinetics of synaptic vesicle release by FM dye unloading has been utilized widely in the field since its introduction in the early

1990s[27–29]. This commonly used method is effective in determining a single quantitative kinetic parameter from a large complex sample facilitating direct comparison between samples. However, this attribute is also a major shortcoming of the traditional analysis method. At typical culture density for hippocampal or cortical neurons, a field of view at 100 X magnification contains between 2 and 5 neurons. Each cell in culture typically forms between 500 and 2,000 synapses yielding a total of 1,000 – 10,000 synapses in each field. This collection of synapses is a complex heterogeneous mixture with slight variations in morphology, connectivity and biochemistry as well as other more subtle stochastic parameters. As each cell is depolarized and an action potential is fired, coordinated waves of ion currents reach each presynaptic terminal at slightly different times where variable densities and conformations of synaptic release machinery await the calcium signal. Heterogeneity in the size of the active zones and readily releasable pools of synaptic vesicles may also impact the exact kinetics of release. All of these variables taken together suggest that it is a vast oversimplification to describe a collection of thousands of synapses with a single kinetic parameter. To overcome this limitation, a novel analysis method was developed which extracts a comprehensive profile of release kinetics at all synapses providing a more complete understanding of both the general trend as well as the biological variability and behavior of subpopulations within a complex sample. Here, the novel analysis method is directly compared to the classical method using the three different ROI maps generated above.

The specific kinetics of the unloading event differ depending on the specimen (typically insect or ranine neuromuscular junction, murine hippocampal slice or cultured neurons) and to an extent the stimulation method (direct electrical stimulation, hypertonic sucrose or high potassium). For the murine cortical neurons used in this study, it is established that unloading follows a single exponential decay model and is ~90% complete within 60 seconds[69]. For this reason analysis was limited to data collected in the first minute following application of hyperkalemic buffer.

In the classical analysis method, synaptic puncta are identified as described above in the stringent method. Using image analysis software, the mean gray value of each ROI is individually measured at each frame in the movie during unloading. The raw intensity value at each time point (t) is normalized to the initial raw intensity value to derive a normalized unloading curve of the form $f_{norm}(t) = f_{raw}(t)/f_{raw}(0)$. The normalized values for all synapses in a sample are averaged at each time point to produce a single value. This averaged value is typically plotted against time with the variance indicated at each point.

We developed a novel method based on the idea that non-synaptic puncta could be identified after processing by virtue of their distinct kinetic profiles. Therefore, in this method the inclusive puncta selection scheme (Figure 9) was employed. To extract kinetic information about each synapse, we took advantage of the fact that FM unloading follows a stereotyped exponential decay. A plugin for ImageJ was written to plot the intensity value at each synapse and perform a fit to

a single exponential of the form $f_{fit}(t) = a \cdot e^{\left(\frac{-1}{\tau}\right) \cdot t} + b$ where $f_{raw}(0) = a + b$ (Figure 10).

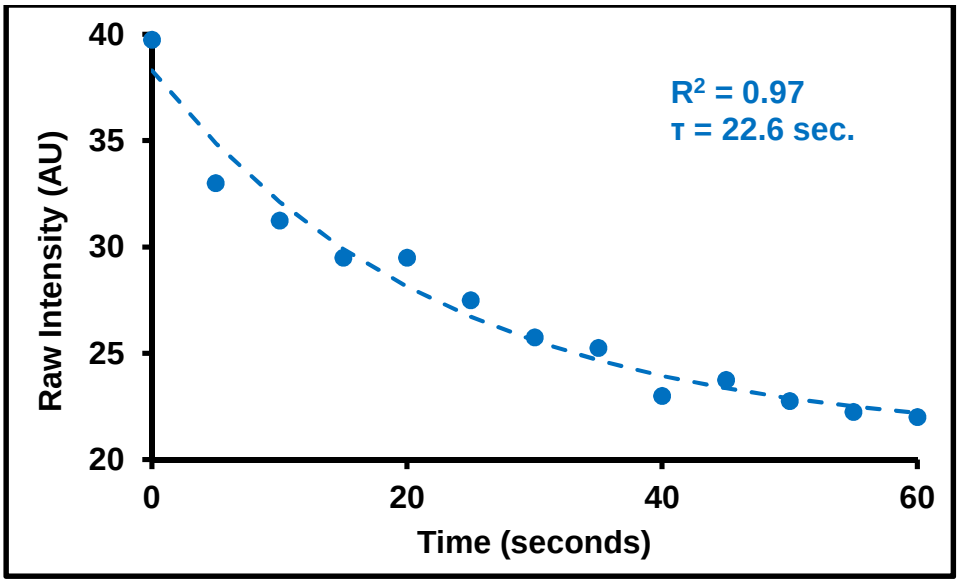

Figure 10: Unloading of Single Synapse and Kinetic Fit
Raw unloading curve of a representative synapse is shown (intensities are arbitrary gray values representing the mean of the ROI at each time point). Raw data was fit to single exponential decay with a residual of 0.97. Extracted time constant, τ = 22.6 seconds.

Because the release profile is well defined ($R^2 \approx 1$) by $f_{fit}(t)$, the characteristic time constant, τ, is sufficient to completely describe the kinetics of release at a single synapse. The plugin reports the values of τ as well as the other parameters of the fit including a residual. These values are then used to remove data which can clearly be discarded as non-synaptic. First, the data is trimmed based on the residual of the fit. ROIs featuring non-exponential behavior typically contain particles of debris traversing the sample under profusion or other spurious events. Across many datasets analyzed by this method (~ 185,000 ROIs), we found that

debris and background ($R^2 < 0.80$) accounted for a small (< 30%) portion of the data (Figure 11). Particles fit with $0.80 < R^2 < 0.95$ were considered low-confidence synapses and were not included in later analysis steps. However, study of many data sets concluded that the low-confidence synapses were likely real because they exhibit equivalent kinetics to the high-confidence cohort. Nonetheless, to ensure the synaptic identity of the particles used in developing this novel method, only puncta with fits where $R^2 > 0.95$ were passed to the next data filtering step.

There are 3 general classes of non-synaptic events which can still be fit with high confidence to the exponential decay equation (Figure 12). Puncta where fit values of $b \leq 0$ and $\tau < 0$ are discarded from the dataset. The remaining trimmed data contains a kinetic time constant of unloading, τ, for each synapse in the original image. To simultaneously visualize kinetic constants for all synapses in a sample, the values of τ are sorted into bins and represented as a histogram (Figure 15, Figure 18 and Figure 21).

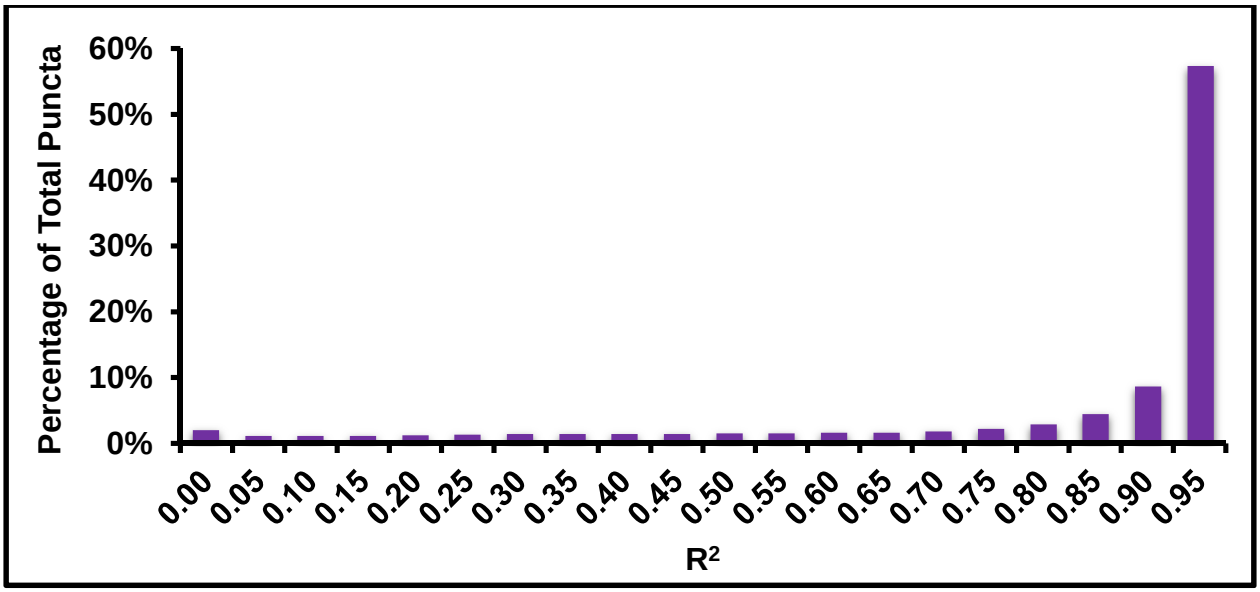

Figure 11: Residuals of Exponential Fits
Across 27 experiments, 184,353 ROIs were fit to an exponential decay model. More than 50% of particles fit with $R^2 > 0.95$. Fits where $R^2 < 0.80$ were considered debris and those where $0.80 < R^2 < 0.95$ were considered low-confidence synapses and were omitted from further analysis.

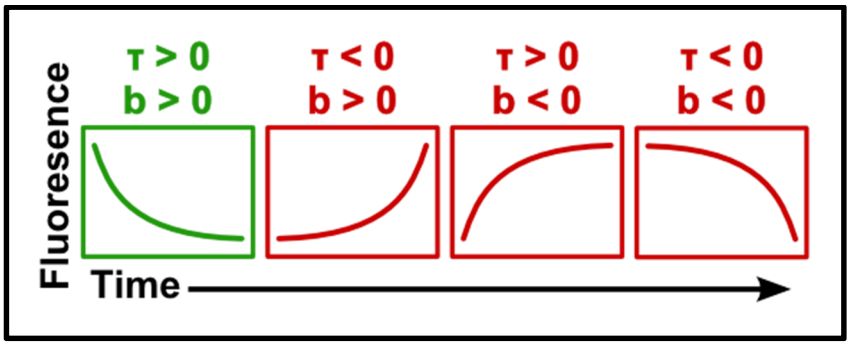

Figure 12: High Confidence Fits of Non-Synaptic Curves
Data can be fit to very high confidence with an exponential equation, however where $b \leq 0$ and/or $\tau < 0$, these puncta are non-synaptic and therefore excluded from analysis. Schematic representation of fluorescence traces derived from particles of these types is shown. Curve of the green type are considered synaptic, the red curves are considered non-synaptic.

Both the classical method of FM destaining analysis, and the novel method presented here, face the common challenge of photobleaching. Depending on the imaging conditions, photobleaching of the FM dye can represent a change in intensity that is significant relative to the signal generated by the biological event. The magnitude of photobleaching must be empirically determined for a given sample type with a particular imaging setup. Provided these elements are held constant, it is safe to assume that the rate of photobleaching will also remain relatively constant between experiments. For the imaging conditions used here, bleaching was determined to be a very minor factor (< 5% of signal) and was therefore not corrected in the analysis.

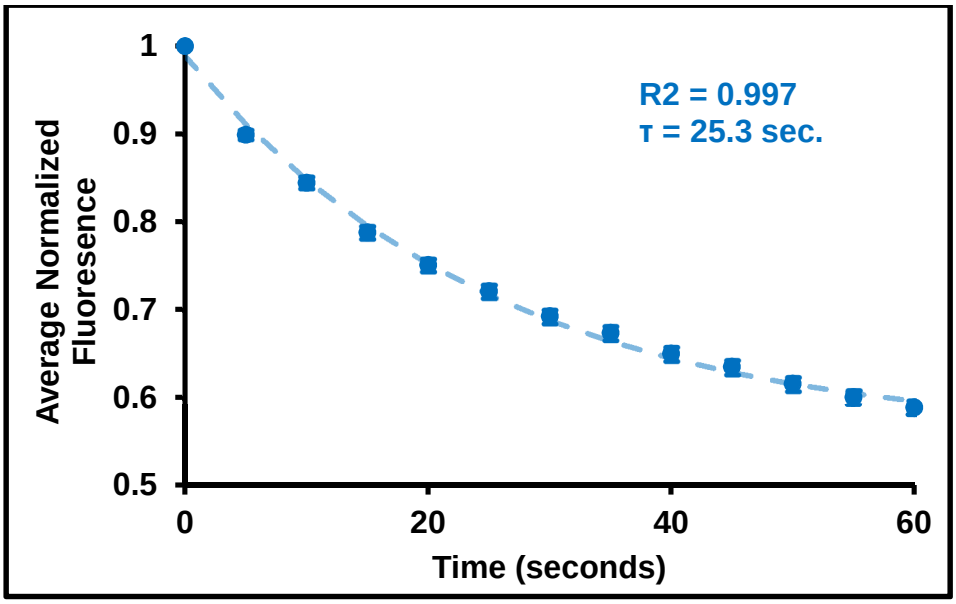

Figure 13: Kinetic Analysis of Averaged Synapses from Manual ROIs
The manually generated ROI map (Figure 7) was analyzed by the standard averaging method. Unloading curve was fit to an exponential yielding an apparent decay constant of 25.3 seconds. Error bars represent SEM.

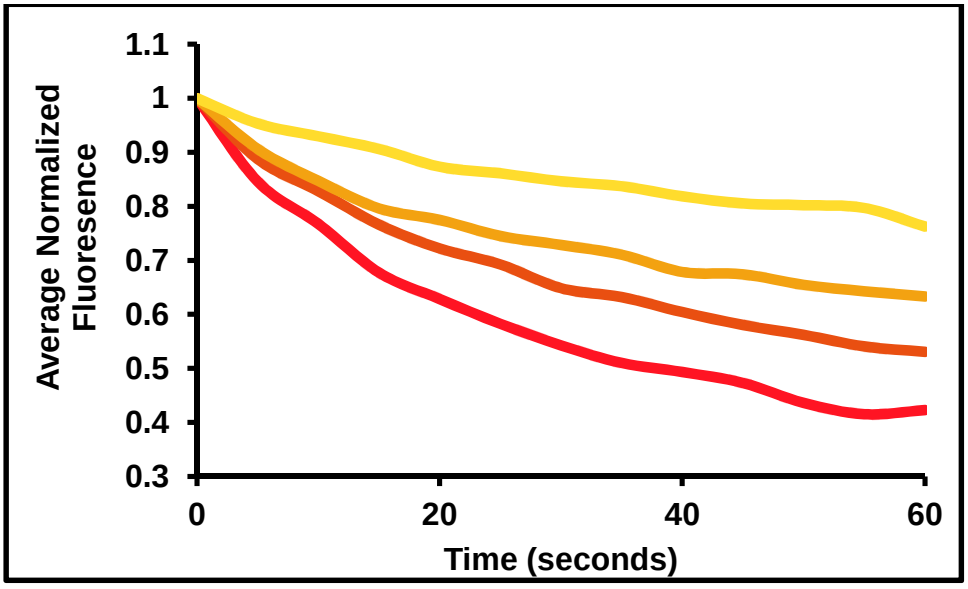

Figure 14: Quartiles of Unloading at Manual ROIs
Data from Figure 13 was split into quartiles sorted by normalized value at the end of the experiment.

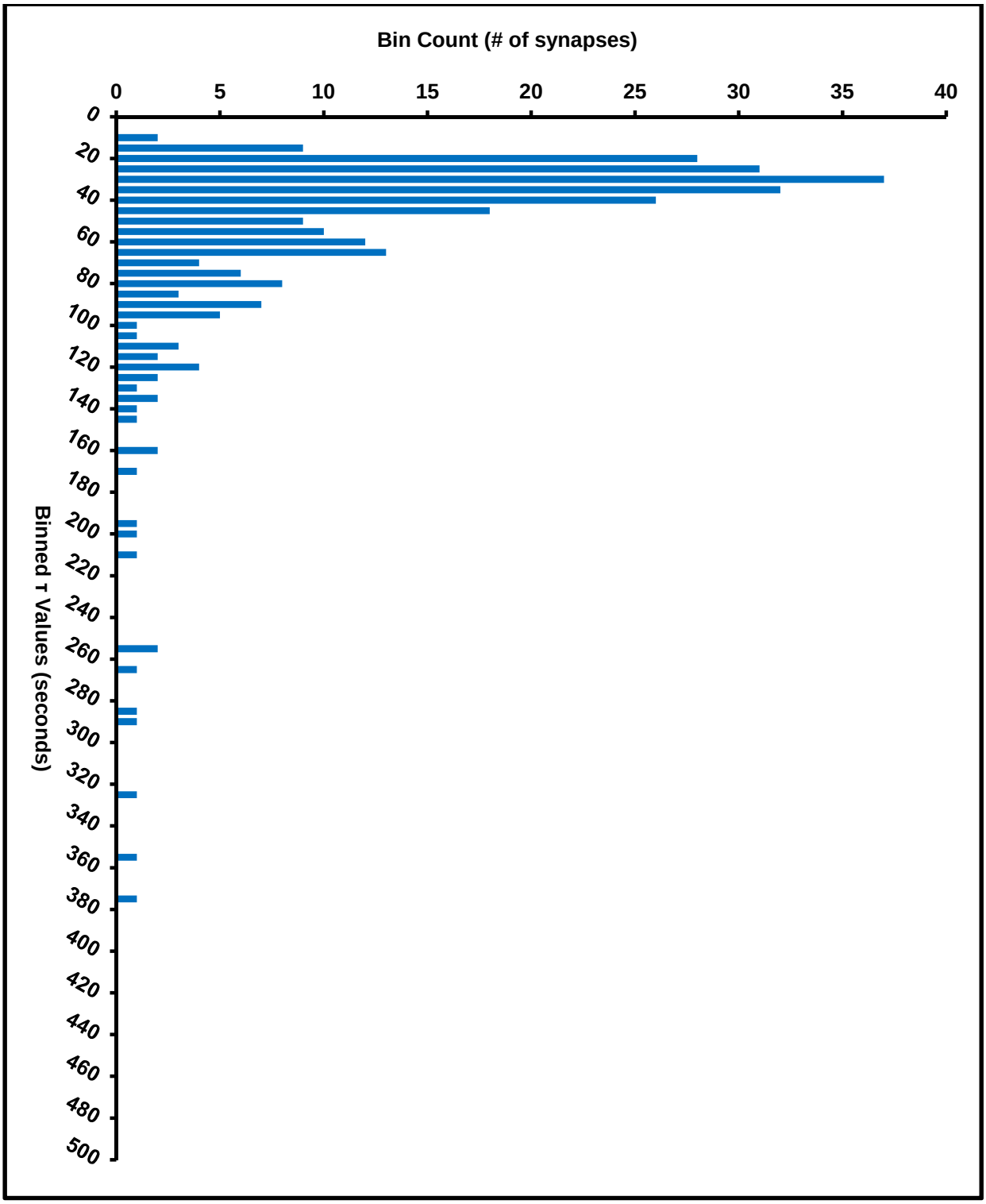

Figure 15: Comprehensive Kinetic Profile of Manual ROIs
Histogram representing distribution of kinetic time constants for each synapse identified from the manual ROI map.

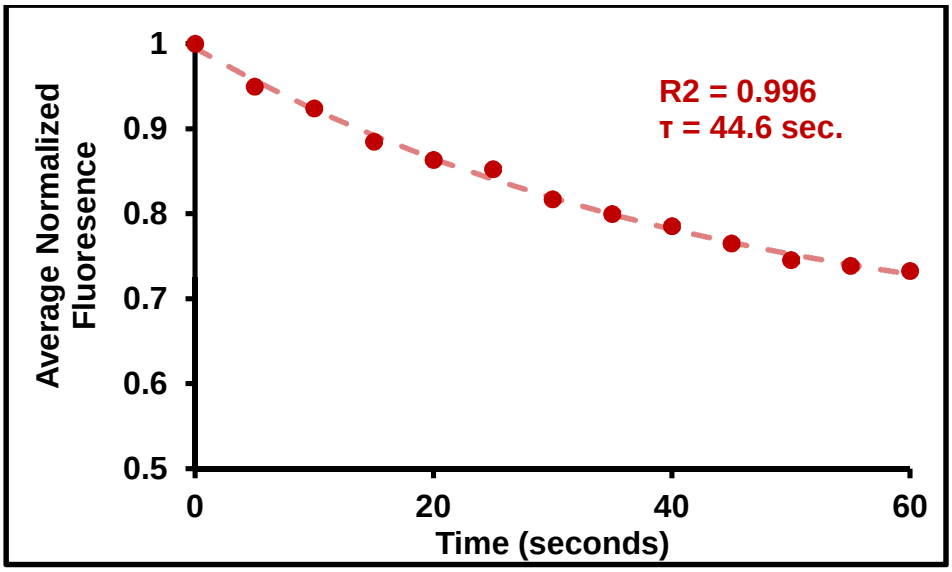

Figure 16: Kinetic Analysis of Averaged Synapses from Stringent ROIs
The ROI map generated by the stringent automated synapse identification scheme (Figure 8) was analyzed by the standard averaging method. Unloading curve was fit to an exponential yielding an apparent decay constant of 44.6 seconds. Error bars represent SEM.

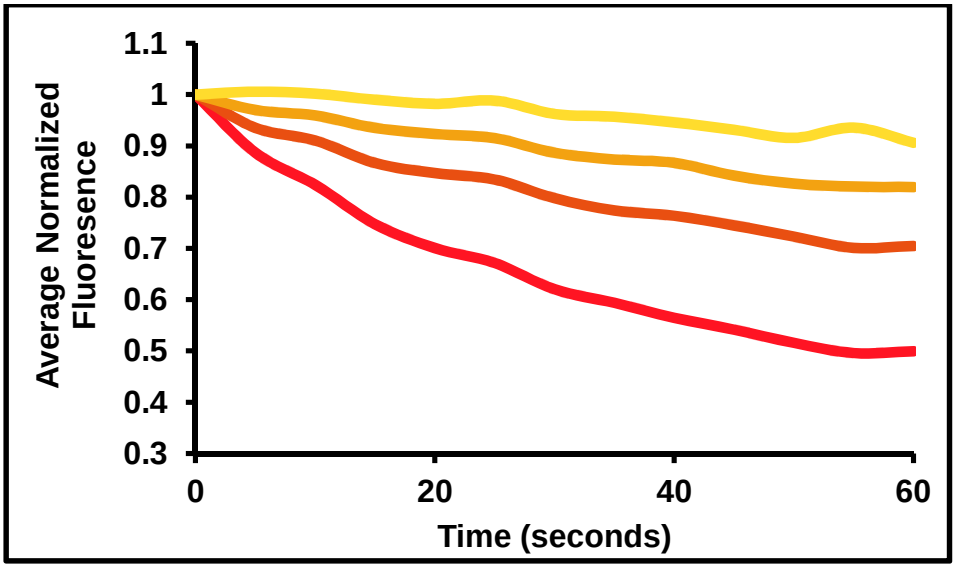

Figure 17: Quartiles of Unloading at Stringent ROIs
Data from Figure 16 was split into quartiles sorted by normalized value at the end of the experiment.

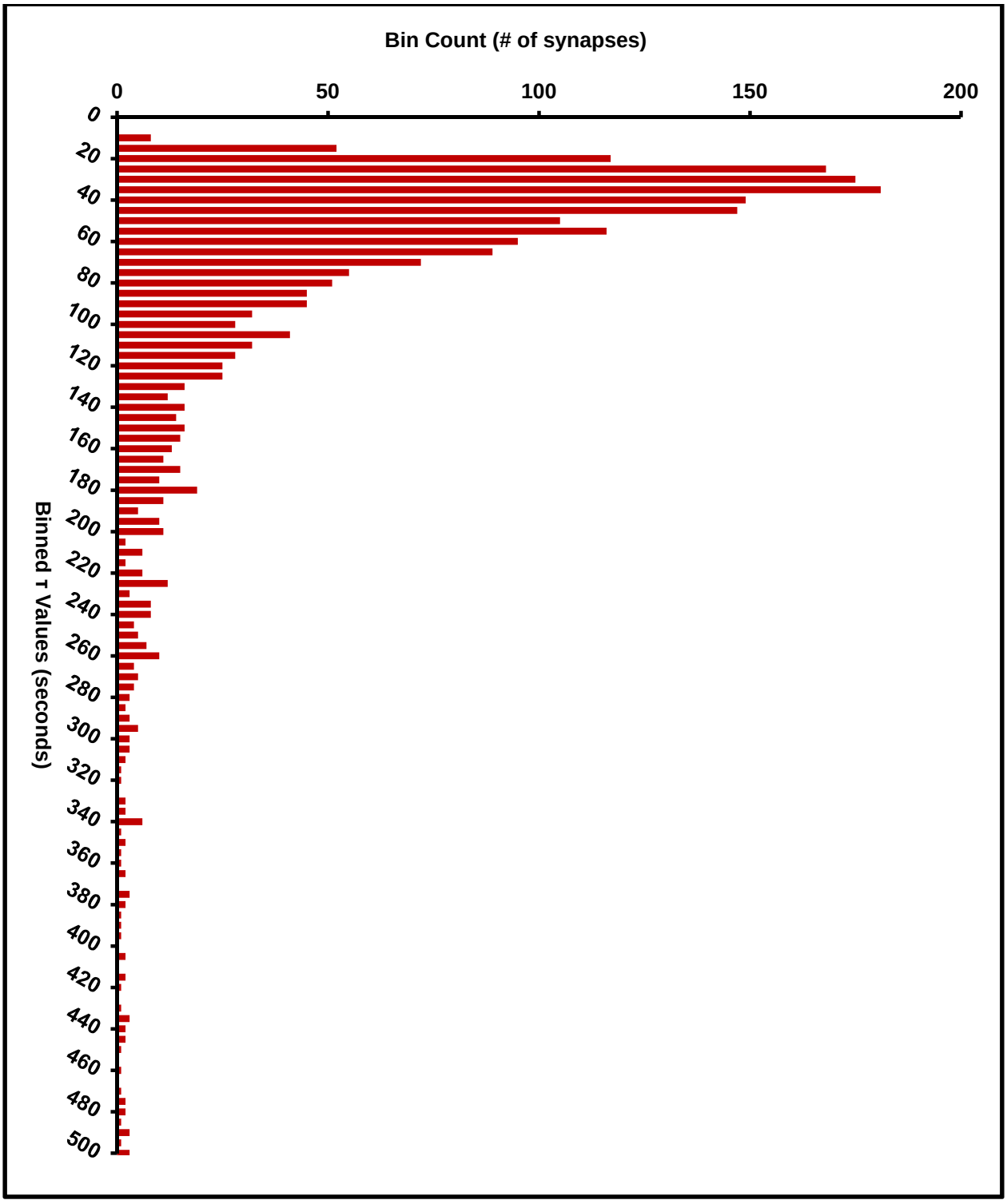

Figure 18: Comprehensive Kinetic Profile of Stringent ROIs
Histogram representing distribution of kinetic time constants for each synapse identified from the stringent automated method.

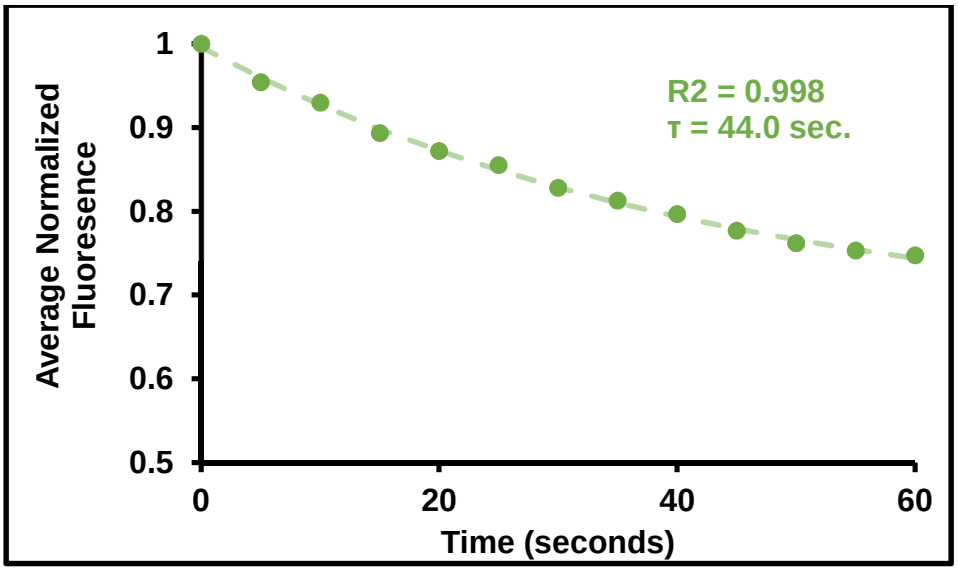

Figure 19: Kinetic Analysis of Averaged Synapses at Inclusive ROIs
The ROI map generated by the inclusive automated synapse identification scheme (Figure 9) was analyzed by the standard averaging method. Unloading curve was fit to an exponential yielding an apparent decay constant of 44.0 seconds. Error bars represent SEM.

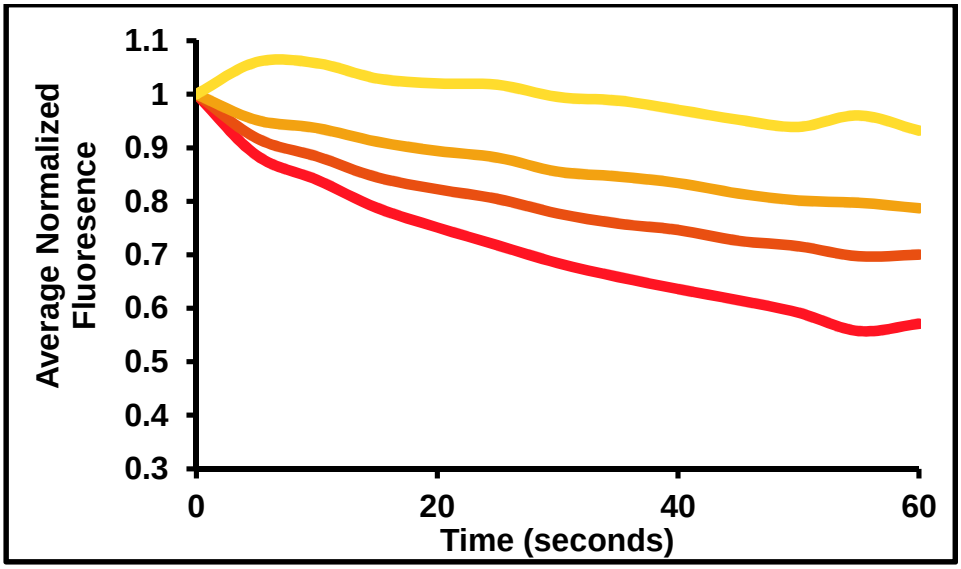

Figure 20: Quartiles of Unloading Inclusive ROIs
Data from Figure 19 was split into quartiles and sorted by normalized value at the end of the experiment.

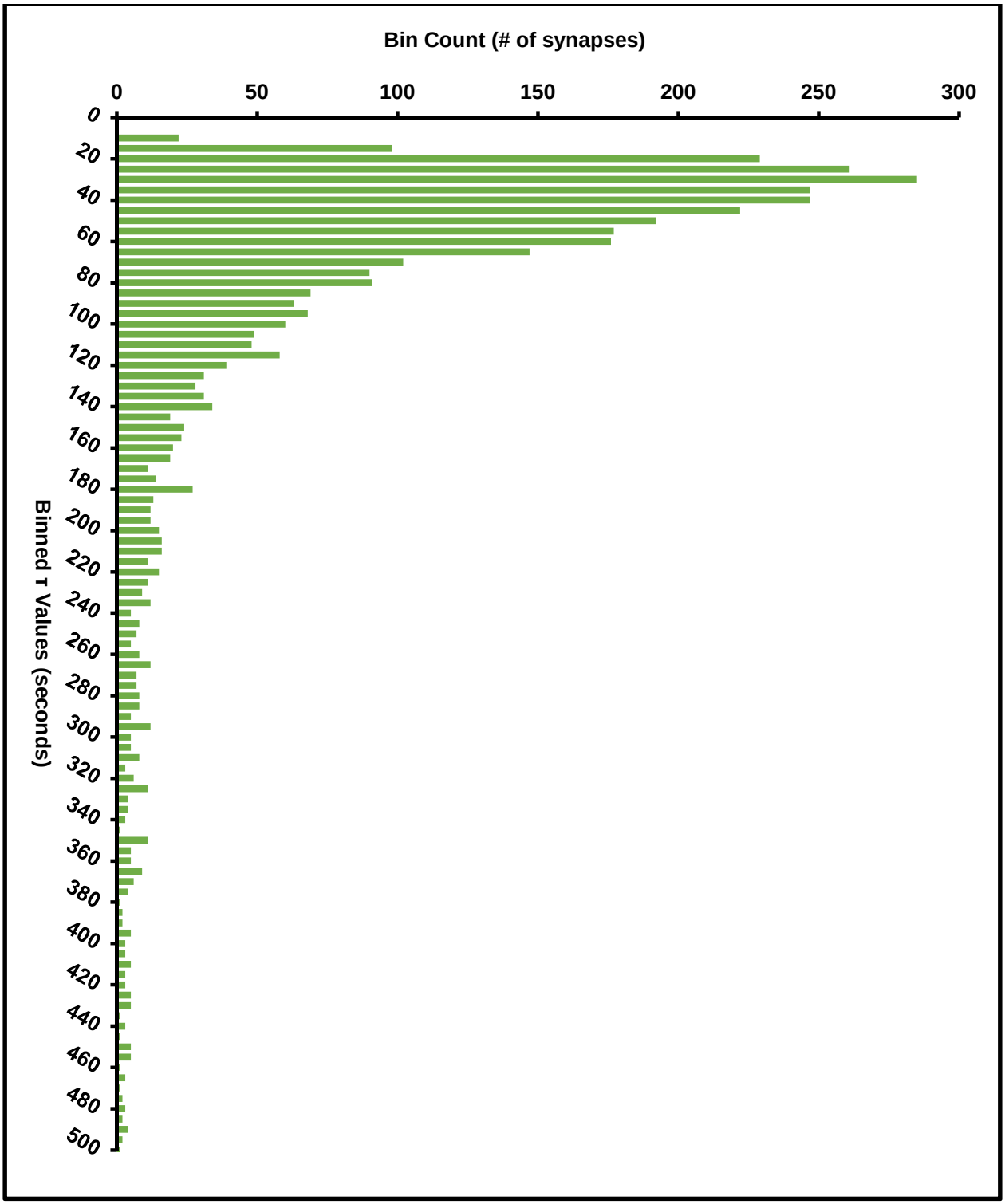

Figure 21: Comprehensive Kinetic Profile of Inclusive ROIs
Histogram representing distribution of kinetic time constants for each synapse identified from the inclusive automated method

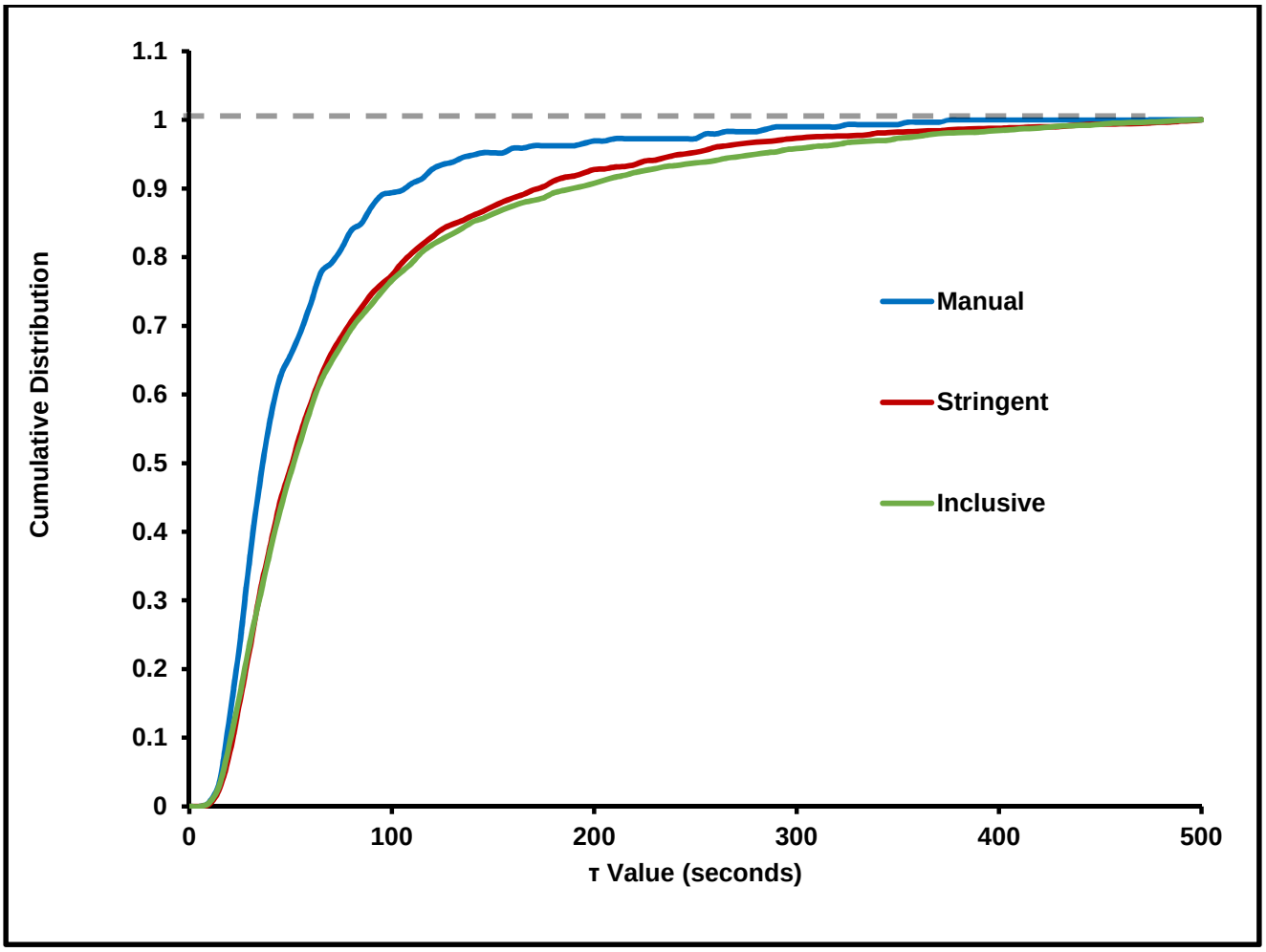

Figure 22: Kinetics Generated from 3 ROI Selection Methods
Cumulative distribution functions from Figure 15, Figure 18 and Figure 21 demonstrate high reproducibility of the novel method derives the true kinetic profile independent of the ROI selection method.

	Manual	Stringent	Inclusive
original ROIs	350	3819	8565
$R^2 < 0.95$	30	812	3364
non-synaptic	0	6	22
final synapse count (%)	320 (91.4%)	3001(78.6%)	5179 (60.5%)

Table 1: Puncta Discarded During Processing

DISCUSSION

Three methods of selecting synaptic puncta were applied to a sample dataset. By simply comparing the ROI set selected between the three different methods (Figure 7, Figure 8 and Figure 9), several features are immediately apparent. First the number of puncta selected by hand is relatively small compared to the other two methods. The manually selected ROIs are more homogenous in size and very few were selected from the most dense areas of the image. ROIs selected by the stringent algorithm tended to be larger than those selected by the inclusive method. The true size of synaptic puncta is likely closer to the smaller end suggesting that the tighter boundaries delineated by inclusive scheme include the least amount of non-synaptic area. Further, it is clear that the inclusive method is capable of selecting synaptic puncta from even the most dense regions of the image allowing the most homogenous sampling across the field of view amongst the three particle selection methodologies.

The classical method of averaging all normalized unloading curves was applied using all three ROI sets (manual, stringent and inclusive). In addition to a trace representing all synapses, a series of curves representing subpopulations were also plotted. For these plots, the individual ROIs were sorted by their normalized intensity at the end of unloading, $f_{norm}(60)$, and broken into quartiles. This is a crude but effective method assaying the heterogeneity of the ROI set used for analysis.

By comparing the average kinetic curves from the manual ROI set (Figure 13) to those from either of the computer generated ROI sets (Figure 16 and Figure 19) it is immediately clear that manual selection of synaptic puncta is strongly biased towards synapses with faster higher contrast dynamics (τ = 25 sec. for manual vs. ~44 sec. for both stringent and inclusive). Both values of τ are roughly within an expected range for samples of this type, but a nearly twofold difference in observed kinetics is quite striking. The bias is not simply towards puncta which change more rapidly (lower values of τ) but also those which undergo larger changes in relative fluorescence regardless of kinetics. The puncta selected by eye lost an average of 41% of signal over 60 seconds whereas the other sets of selected puncta lost an average of roughly 26% in that same time. Based on this we conclude that particles selected by the human eye are both skewed towards fast kinetics as well as large relative dynamics.

By looking at the quartile analysis, the fastest quarter of each ROI set (red trace in Figure 14, Figure 17 and Figure 20) is much more comparable (τ = 22, 28 and 30 sec. for manual, stringent and inclusive respectively). This indicates that it is not a preponderance of extremely fast puncta that generated the twofold difference in the manual ROI set, but simply the absence of slower particles - consistent with selection bias against particles that didn't display fast kinetics and dramatic changes during the manual inspection of the unloading experiment. It is also evident from this analysis that the manual selection yields the least diverse set of puncta. The kinetic trace for the bottom three quartiles is far more similar than

in datasets for puncta selected in either automated scheme. This homogeneity again points towards bias of manual selection and highlights the loss of valuable biological information it suffers particularly with regard to kinetics.

Because of the intentional low selectivity of the inclusive ROI selection method, it is unsurprising that the slowest quartile (yellow trace Figure 20) indicates a population of erratic and slow-decaying puncta relative to the stringent analysis (yellow trace Figure 17). As predicted by the non-exponential behavior of roughly 25% of the particles (Figure 11) we would expect to trim about that much of the dataset before final analysis, so we were encouraged to observe that these two different methods found a similar proportion of non-synaptic puncta. For use with classical population average-based kinetic analysis of FM detaining, the inclusive ROI selection method proved an adequate substitute for the more selective and well tested method in this dataset (τ for inclusive $\approx \tau$ from stringent). It is not obvious that this trend would persist in other samples but it warrants further investigation. The inclusive method requires much less manipulation of the image to derive an ROI map, so it is likely to be less variable from sample to sample and is also more generalizable to other image analysis situations involving similar puncta. Any algorithm designed to sort signals into two classes based on some objective criteria must balance high sampling depth and false positives against poor coverage with high confidence. In this case because the sample size is large it would be acceptable to make a modest sacrifice of coverage if the remaining sample was still representative. By comparing the total distribution of kinetic events called each

algorithm (Figure 18 versus Figure 21) it is clear that both methods selected similar populations despite nearly 60% more synapses identified by the inclusive method (see Table 1). From this we conclude first that the more stringent conditions were capable of selecting a representative sample in this case. Second, it appears that the increased sample population obtained by the inclusive method contained few false positives. Thus, it appears that with this sample dataset, the inclusive method is capable of maximizing sampling depth without sacrificing accuracy and confidence.

The novel population-based kinetic analysis tool presented here brought to the forefront elements of FM unloading data that typically remain unseen. Importantly, the distribution of kinetic profiles at different synapses exhibits significant positive skew. For this reason, the mode of the distribution is a much more biologically relevant descriptor than the mean as is classically reported. We found that for automated synapse selection both in this sample dataset as well as scores of others, the population averaging method leads to an underestimate of the kinetics that describe the majority of synapses (mode $\approx$ 30 sec.; mean $\approx$ 45 sec.). Of course the initial intent of this method was to get away from summing a complex population of events into a single number, so the real strength is the fact that we can simultaneously view the kinetics of all synaptic release events. This additional information dramatically increases the sensitivity of the assay by allowing dissection of subpopulations of synapses. For example, many different types of calcium channels are found at different synaptic terminals and there are a number of pharmacologic ways of targeting specific subsets of these channels. Our novel

analysis method would allow deconvolution of altered kinetics as synapses impacted by disruption of channel function from the unchanged kinetics as other synapses.

Another interesting benefit of the population based kinetic analysis is reduced sensitivity to sampling bias and sample to sample variability. Despite the fact that the manual ROI set vastly underestimated the pool of slower synaptic release events, it still selected more events with a τ = 30 sec. than for any other time bin – same as for the inclusive method. Again, by looking at the mode of each distribution, we can clearly see that all three particle selection methods display the same trend. Even by feeding our algorithm vastly different representations of the same biological event, it is still capable of extracting very similar and descriptive kinetic data. Owing to this feature, it is clearly a much more robust tool to assess the true kinetics of a biological sample.

CONCLUSION

Here we present a novel data analysis method for studying the kinetics of neurotransmitter release using popular and well established optical tools. We have demonstrated superior accuracy, sensitivity and robustness as compared with the current state of the art method. We have found that our method produces data that generally agrees with the trend extracted from population averaging, but provides a much more comprehensive and nuanced perspective. While we believe this new method constitutes a vast improvement over the current method of FM analysis, the power of this tool extends beyond neurotransmitter release kinetics. Many dynamic events in cells and living tissues can directly or indirectly labeled with optical probes that allow high quality imaging. Our approach to FM release analysis is easily modified for studying the dynamics of other puncta and we've built it on a platform consistent with that ambition.

ACKNOWLEDGMENTS AND ATTRIBUTIONS

I'd like to thank and acknowledge Domenico Galati for his important contributions to the work presented in this chapter. He wrote the original ImageJ scripts which I modified into the final versions used for puncta selection and kinetic analysis. The experimental design and specific methods used were generated through discussion with Domenico Galati and Michael Stowell. Additional helpful discussions included many members of the Stowell lab especially Stephen Eisenberg.

CHAPTER 3: SYNAPTOPHYSIN CATALYSIS OF RELEASE IS TARGET OF AB42

INTRODUCTION

Synaptic vesicles (SV) are the organelles that traffic neurotransmitter to the synaptic cleft and propagate signals between neurons upon fusion with the plasma membrane. The SV lifecycle is complex and carefully regulated from endocytosis, maturation and neurotransmitter loading to docking and release. The fusion event is mediated by the interaction of the v-SNARE synaptobrevin2 (VAMP2) with the t-SNAREs syntaxin-1/SNAP-25[70]. Disruption at any point in the SV cycle can result in dysfunction leading to a myriad of neurological and neurodegenerative disorders[71–73]. Alzheimer's disease (AD) is a progressive neurodegenerative disorder and the sixth leading cause of death in the US[38], but despite years of intensive work, the molecular etiology of the disease remains enigmatic. It has, however, become clear that the 42 amino-acid ß-amyloid peptide (Aß42) is key in the disease mechanism[61]. Recent investigation has focused on identifying the molecular and cellular targets of Aß42 in hope of developing therapies for this currently untreatable condition. Recently identified targets include the cellular PrP protein[64], NMDA receptor[65] and PirB[66], yet how such potential targets lead to the disease is unclear.

Synaptophysin (SYP) was one of the first synaptic proteins identified[6,7] and is one of the first proteins to be lost in the progression of AD[74–76], and it is suggestive

that SYP may play a role in the disease. However, despite nearly 30 years of investigation, its biochemical function has remained elusive and ascribing a role for SYP in the synaptic vesicle cycle let alone AD has been problematic. Synaptophysin is a 4-pass integral membrane protein[77] that forms a hexameric channel-like structure[5,78] and comprises ~10% of the SV proteome by weight[13]. Synaptophysin is ubiquitously expressed in synapses throughout the mammalian brain[79] and conserved to nematodes[12], yet is seemingly dispensable for normal CNS development and function as evidenced by the lack of overt phenotypes in the *SYP* -/- mouse[11,16]. This genetic result originally led to the general belief that the protein has no important function. Recently, however, it has been demonstrated that knockout animals compensate for the loss of SYP through the activities of related proteins[14,80]. While this type of compensation has made it difficult to observe phenotypes in single *SYP* -/- mice, modest effects in working memory and SV endocytosis have been reported[16,17].

It has long been known that SYP physically interacts with VAMP2 in SVs[18], but until recently the importance of this interaction has been poorly understood. New evidence has suggested that SYP is involved in trafficking VAMP2 back into SVs upon endocytosis[20] and that this interaction can be disrupted by Aß42[81]. Here we report the first 3D structure of the native SYP/VAMP2 complex as well as biochemical and *in vivo* analyses which demonstrate that SYP functions as an entropic catalyst in neurotransmitter release and that this function is directly targeted by Aß42 causing synaptic dysfunction early in the progression of AD.

SYNAPTOPHYSIN IS A DIRECT TARGET OF AB42

Many cellular and neurological phenotypes have been attributed to excess Aβ42 in the brain, however it has been difficult to conclusively demonstrate that any are directly caused by the peptide. Aβ42 is highly prone to aggregation and is the major constituent of the plaques which are the salient hallmark of AD, yet it is the pre-fibrilar forms that are the toxic drivers of AD pathology (reviewed ref.[50]). To identify direct disease-relevant targets, small soluble Aβ42 oligomers were coupled to a resin and subjected to synaptosomal extracts. We found that immobilized Aβ42 was capable of binding SYP out of brain homogenates (Figure 23), and that the interaction was specific to SYP as no binding was observed for the paralogs synaptoporin (62% identity) or synaptogyrin1 (22% identity) nor for VAMP2 or the loading control MAP2. Silver stain revealed many bands of proteins associated with Aβ42 most of which are high abundance proteins clearly visible in the lysate as well.

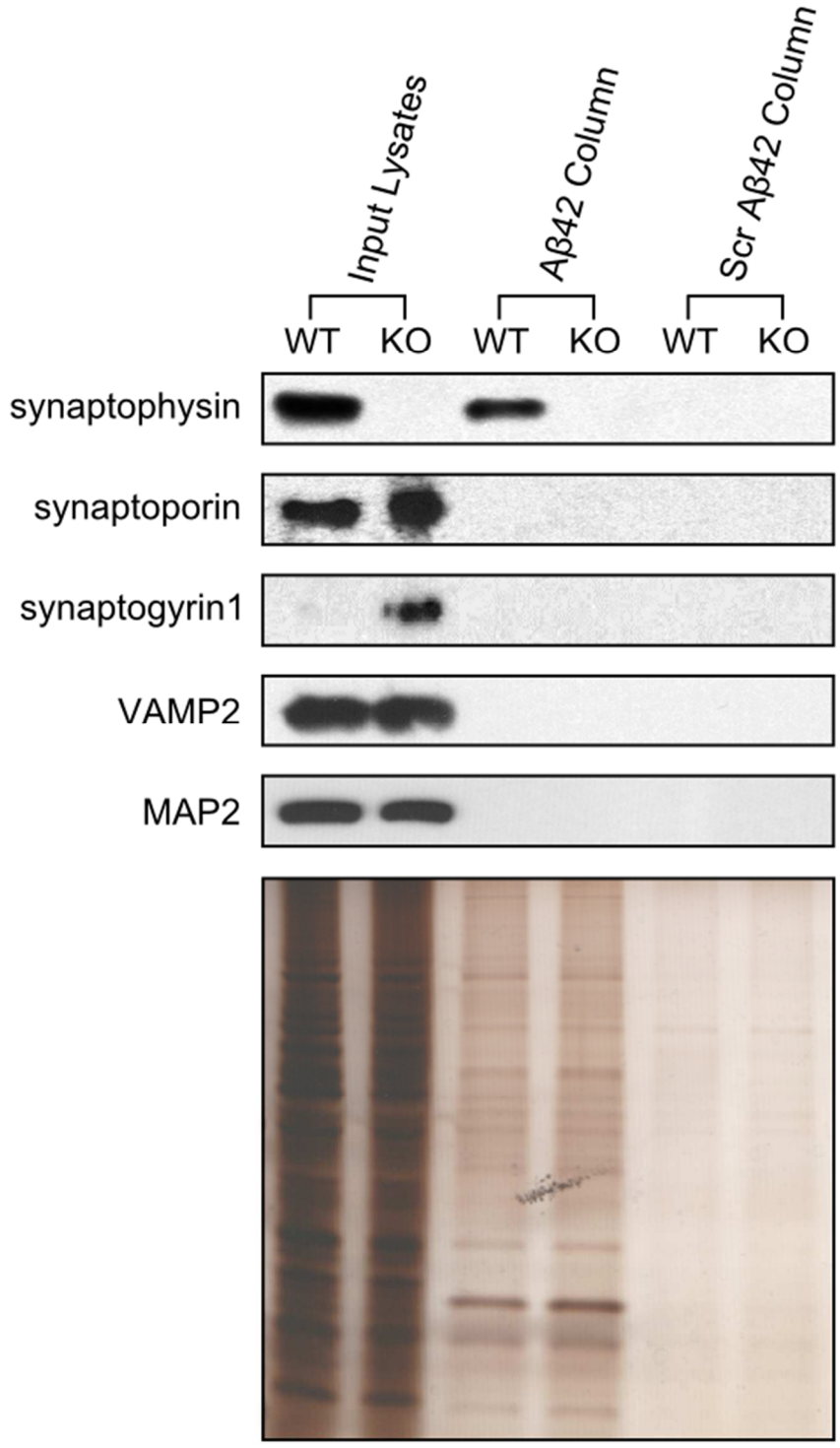

Figure 23: Aβ42 Binds Specifically to SYP
Western blot for synaptic proteins applied and bound to immobilized column of Aβ42 or scrambled peptide. Silver stained of same gel.

To determine if binding was direct, we analyzed the interaction of purified human SYP to immobilized Aß42 by surface plasmon resonance (SPR). A remarkably robust binding was observed over a range of protein concentrations (Figure 24) demonstrating that SYP can bind directly to Aß42 in the absence of other proteins or cofactors. We also failed to observe binding of control proteins of similar membrane topology or isoelectric point (Figure 24) further supporting the specificity of this interaction. We observed an on rate of 835507 sec^{-1} and off rate of 0.003746 M^{-1} sec^{-1} and calculated that Aß42 binds SYP with a K_d of 4.5 nM for the SYP monomer and 750 pM for the native SYP hexamer.

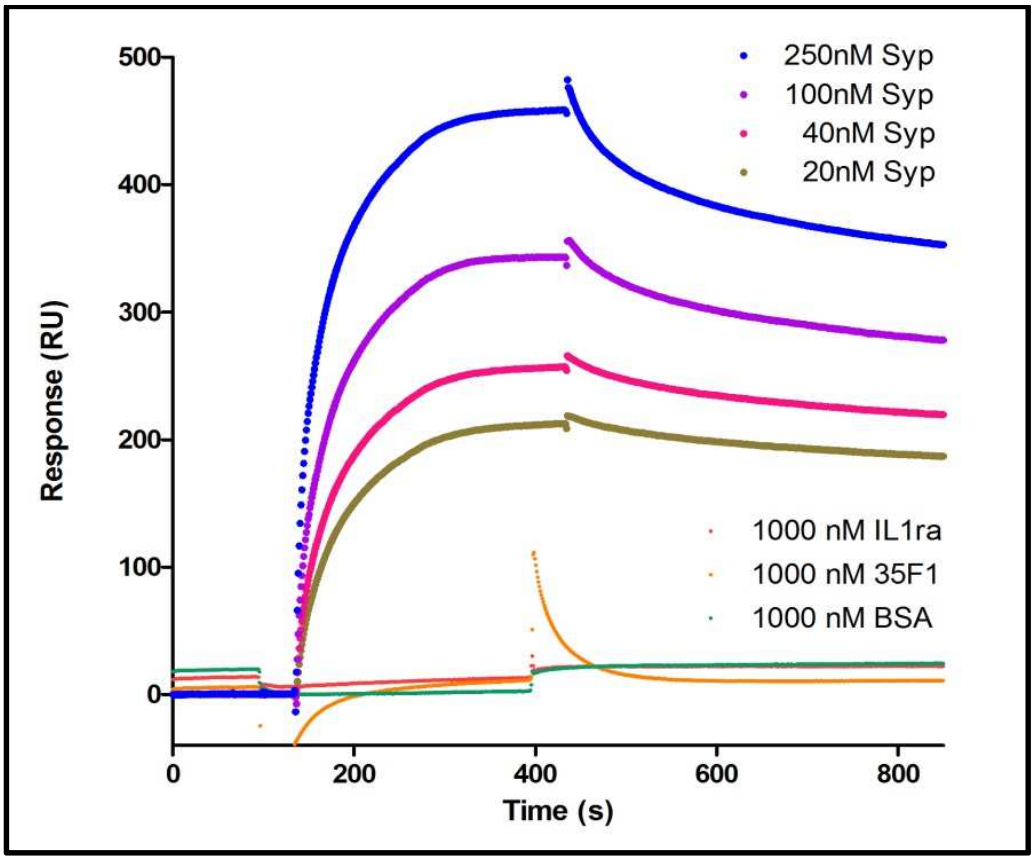

Figure 24: Aβ42 Binds Tightly and Specifically to SYP
SPR sensorgrams indicating binding of recombinant SYP and control proteins with similar isoelectric points (BSA, IL-1ra) or similar membrane topology (SLC35F1) to Aβ42. ***c,*** *Normalized maximal binding of SYP to Aβ at increasing cholesterol concentration. $p < 0.001$ (***); $p < 0.05$ (*).*

Historically, the only biochemical function directly attributed to SYP is its binding to VAMP2, purportedly to modulate the activity of the SNARE protein[18,20,23,82]. To determine if Aß42 association with SYP impaired VAMP2 binding *in vivo*, we treated cultured neurons with Aß42 peptide and performed co-immunoprecipitations. We observed that Aß42 perturbed the robust association between SYP and VAMP2 when immunoprecipitating for either protein by roughly 50% (Figure 25 and Figure 26).

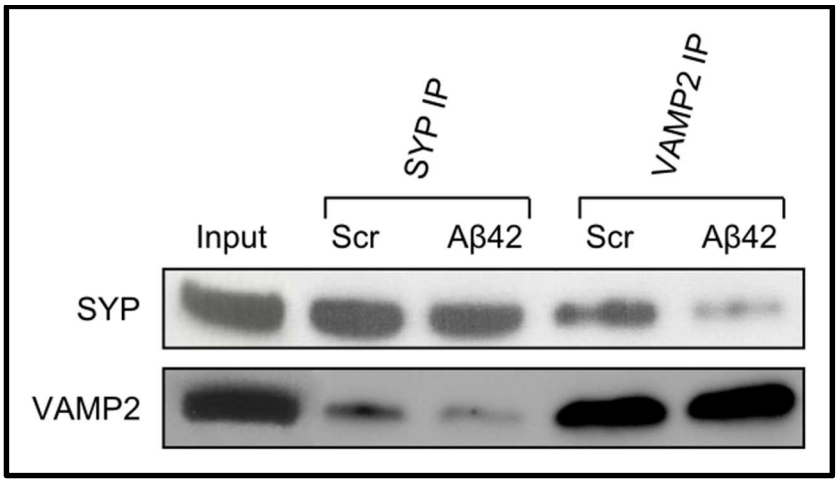

Figure 25: Aβ42 Disrupts SYP/VAMP2 Complex
Representative western blots from immunoprecipitation samples. Multiple experiments were performed and quantified below in Figure 26.

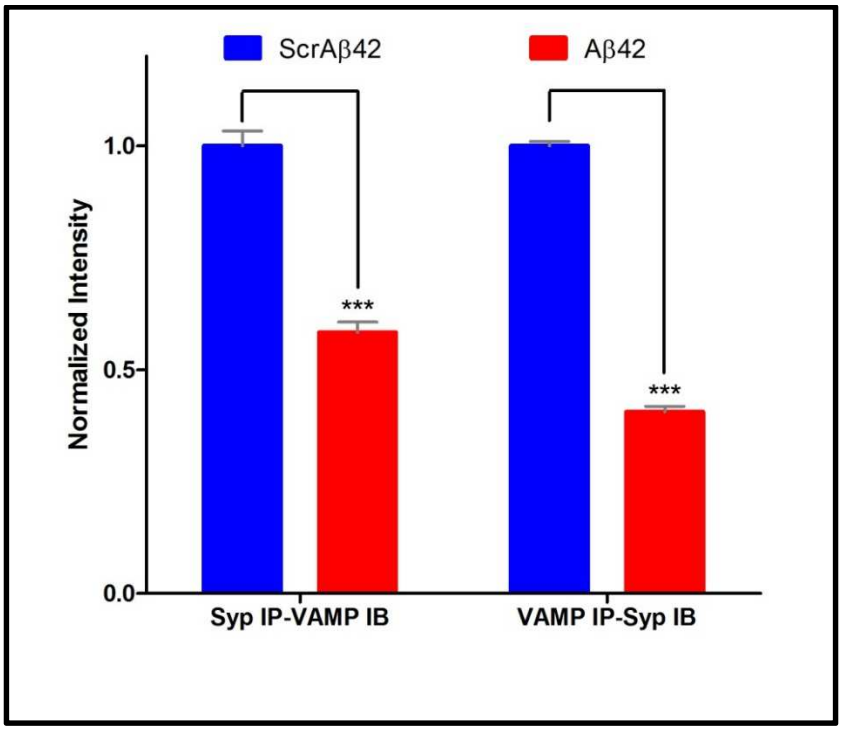

Figure 26: Aβ42 Disrupts SYP/VAMP2 Complex
Cortical neurons treated with Aβ42 (blue bars) or scrambled peptide (red bars) were lysed and immunoprecipitated for SYP (left) or VAMP2 (right) and probed for the other protein. Quantification of western blots from multiple experiments; error shown as SEM (SYP IP N=3, VAMP IP N=2); $p < 0.001$ (***).

Recent evidence has implicated SYP in SV endocytosis[17,20,82], however it has long been hypothesized that SYP also regulates exocytosis by virtue of its association with the SNARE protein VAMP2[18]. To directly test the importance of the SYP/VAMP2 interaction in exocytosis, FM dye unloading from cortical neurons was used to interrogate the release kinetics of more than 175,000 individual synapses. The change in fluorescence over time at each synapse was plotted and fit to an exponential decay described by a characteristic time constant τ (Figure 27). The τ values were then sorted into bins of five seconds and represented as a histogram to visualize the full distribution of release kinetics at all synapses. We observed a fairly tight distribution of kinetic profiles with a maximum at 45 seconds in wild type neurons which significantly shifted upon treatment with Aß42 to a distribution with a maximum at 85 seconds (Figure 28).

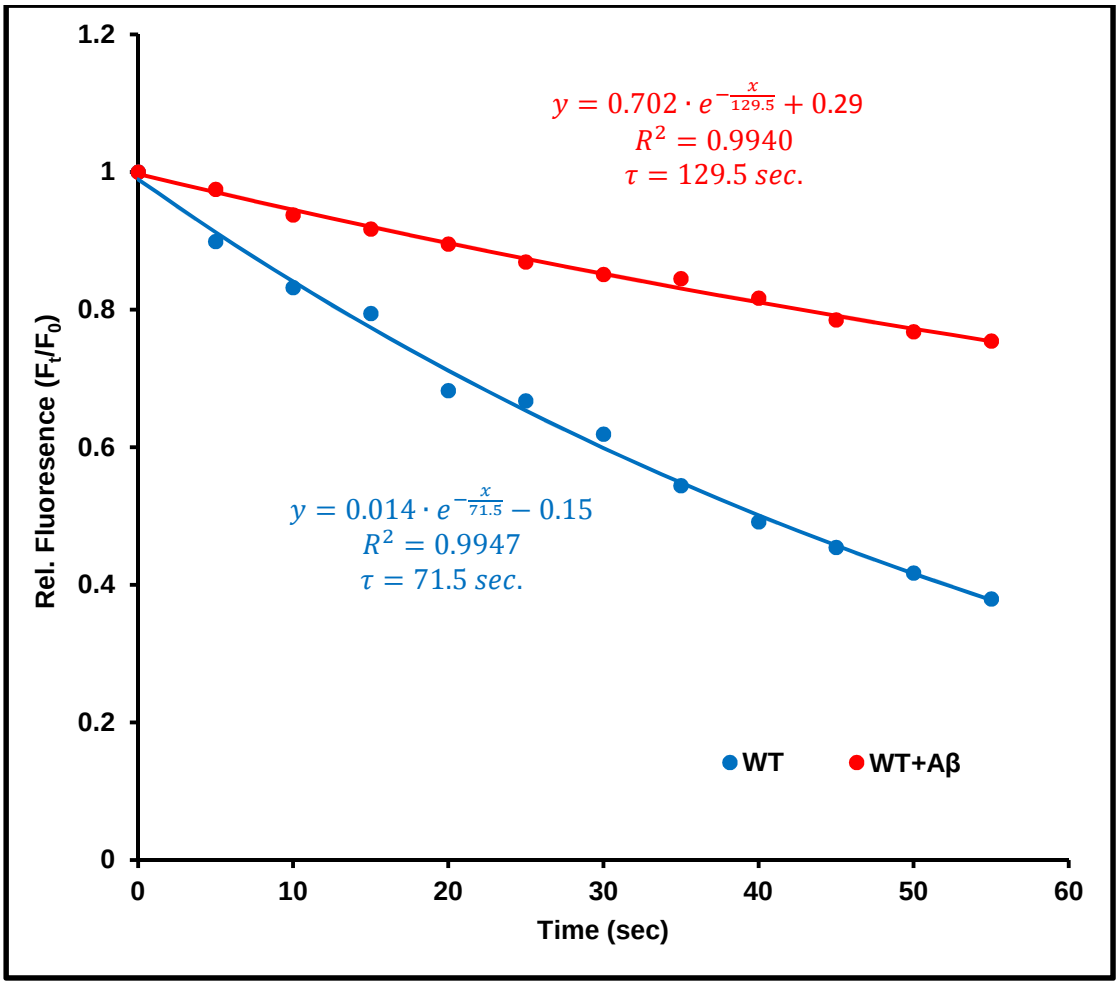

Figure 27: Representative WT Unloading Curves
Representative raw data and single exponential fits of individual synaptic release kinetics nearest the median τ value.

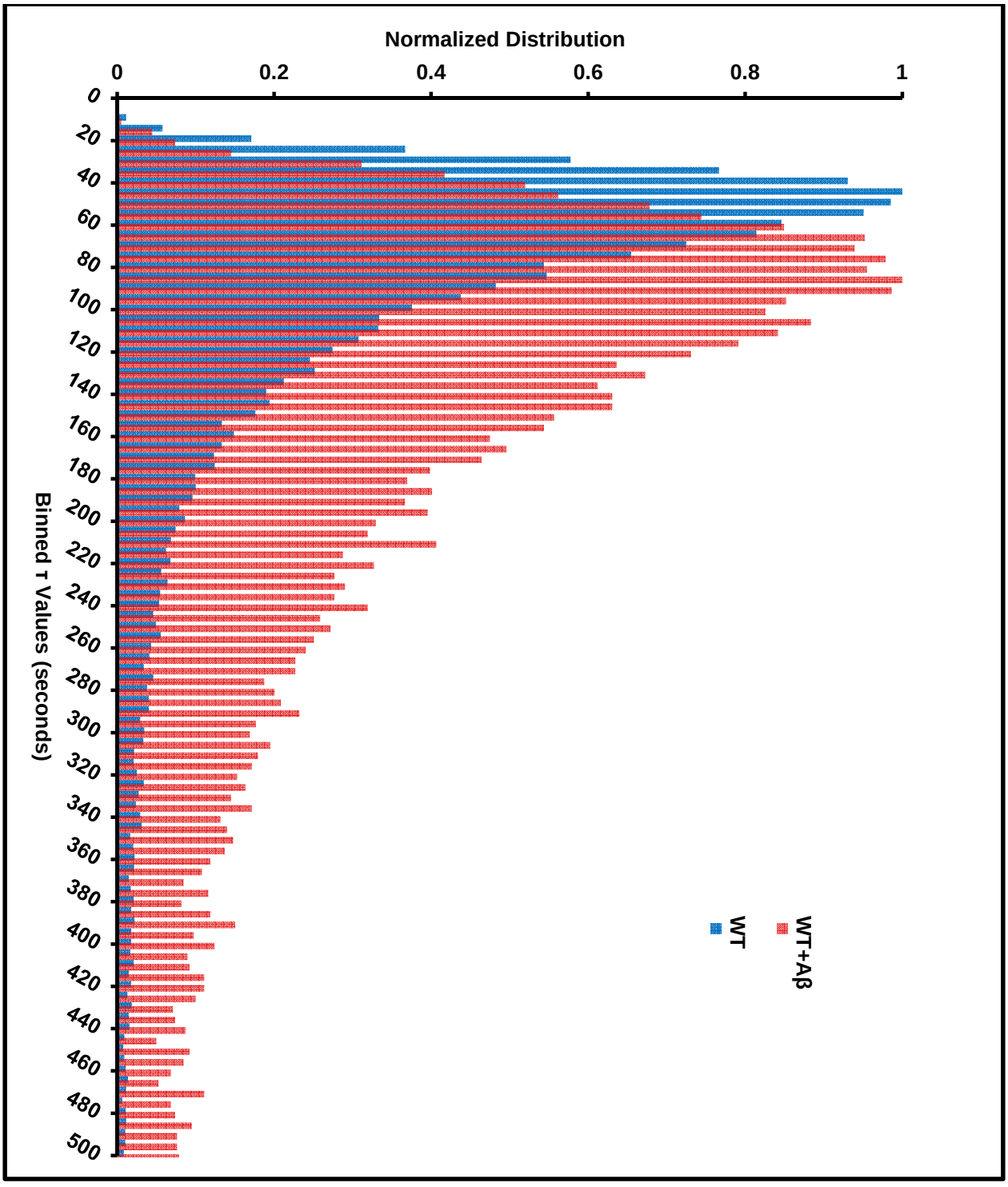

Figure 28: WT Release Kinetics

Distribution of kinetic time constants (τ) for all synapses observed for wild type neurons treated with Aβ42 (red, 12,364 synapses from 16 experiments) or with scrambled Aβ42 (blue, 22,996 synapses from 15 experiments).

We hypothesized that Aß42 binding to SYP and subsequent reduction of intact SYP/VAMP2 complex was responsible for the dramatic perturbation of neurotransmitter release kinetics. To directly test this hypothesis we performed the FM unloading analysis in *SYP* -/- neurons. The loading efficiency was comparable to that observed in WT neurons but consistent with the ~10% decrease in endocytosis kinetics reported by others[17]. As predicted by other functional assays[14,83], the knockout neurons displayed wildtype release kinetics (Figure 30). Remarkably however, we found that *SYP* -/- neurons were nearly insensitive to the exocytosis defects imparted by Aß42 treatment (Figure 30). In the *SYP* -/- neurons, Aß42 treatment had a modest and non-significant impact on kinetics.

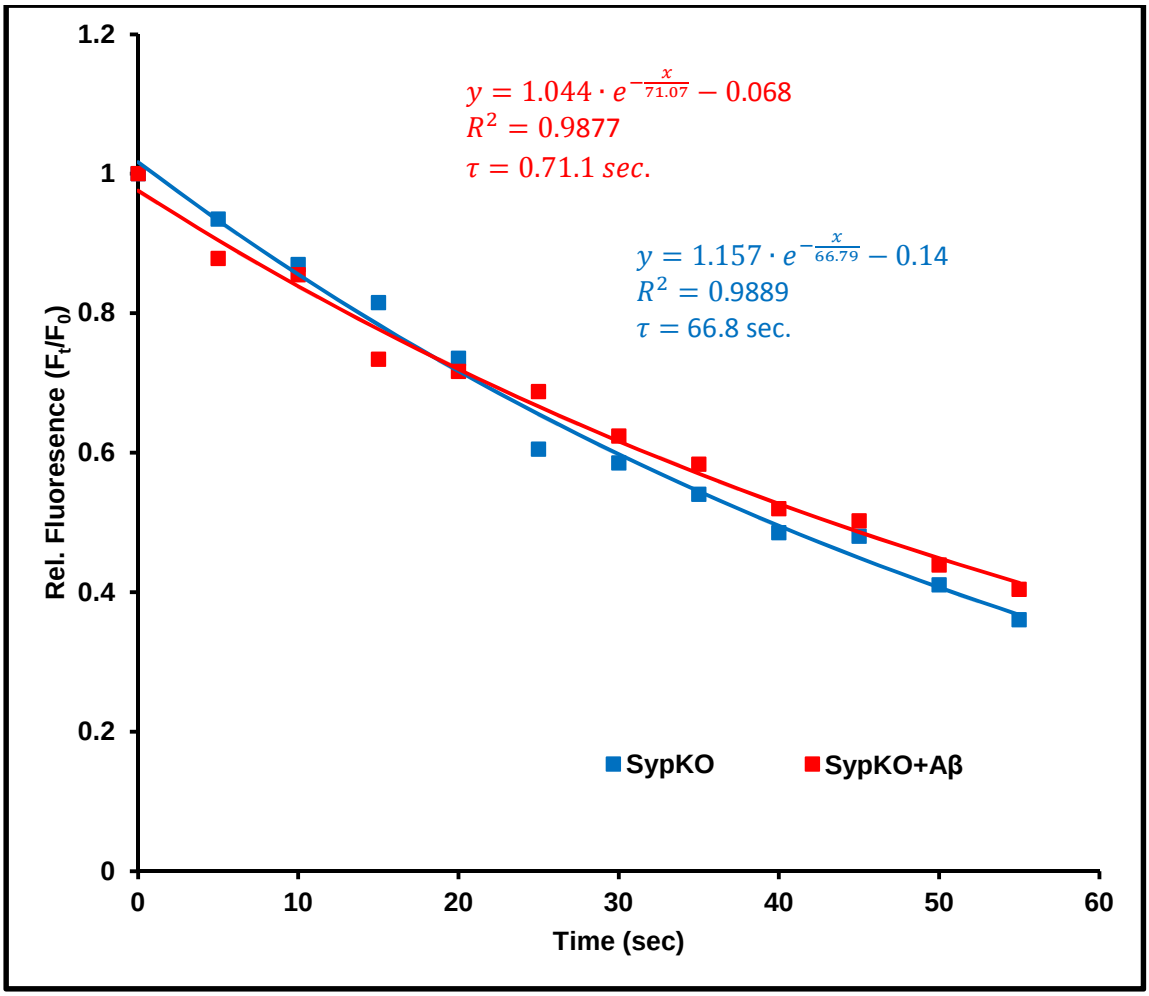

Figure 29: Representative SYP KO Unloading Curves
Representative raw data and single exponential fits of individual synaptic release kinetics nearest the median τ value.

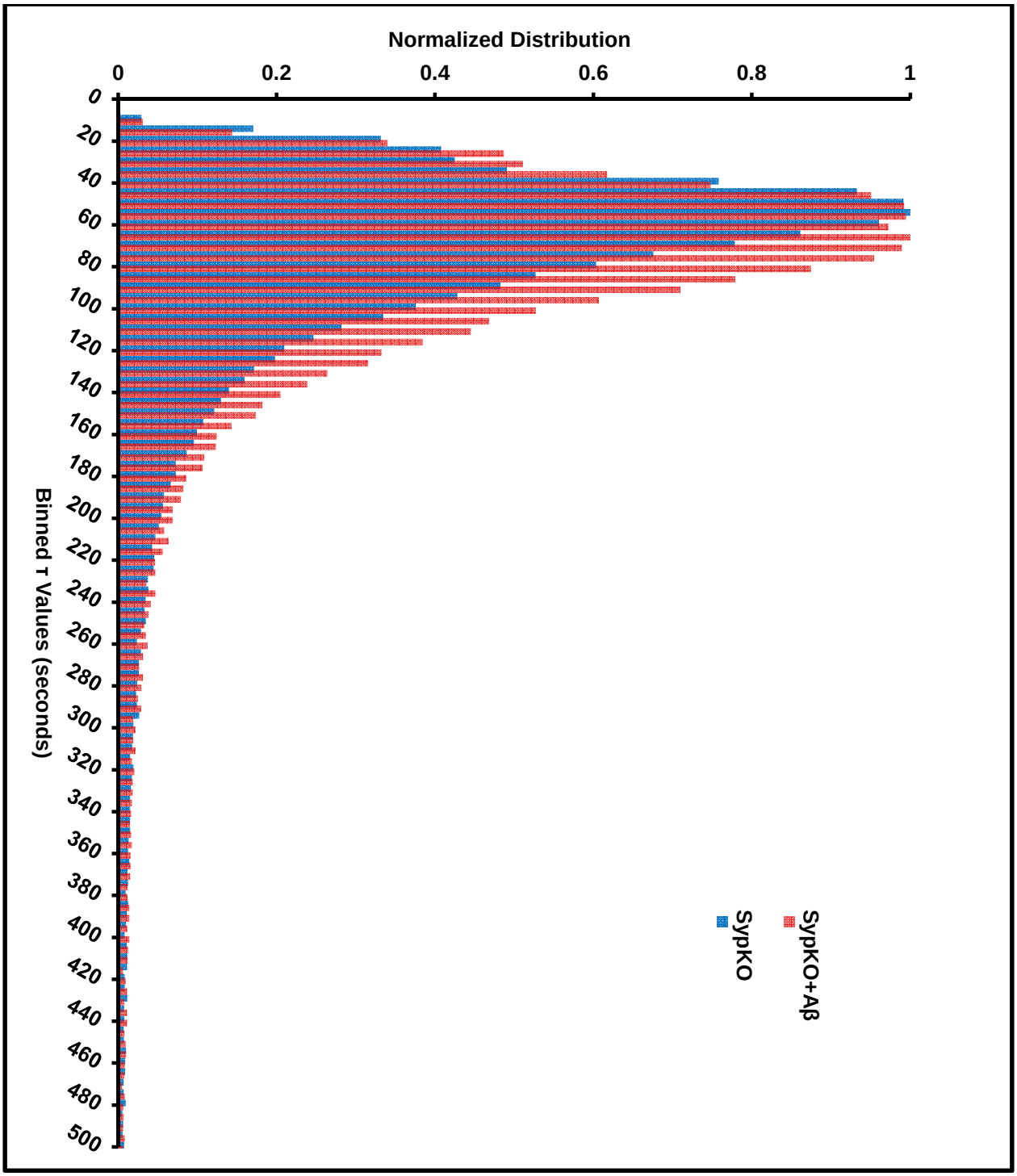

Figure 30: SYP KO Release Kinetics

Distribution of kinetic time constants (τ) for all synapses observed for SYP -/- neurons treated with Aβ42 (red, 68,611 synapses from 14 experiments) or with scrambled Aβ42 (blue, 75,274 synapses from 11 experiments).

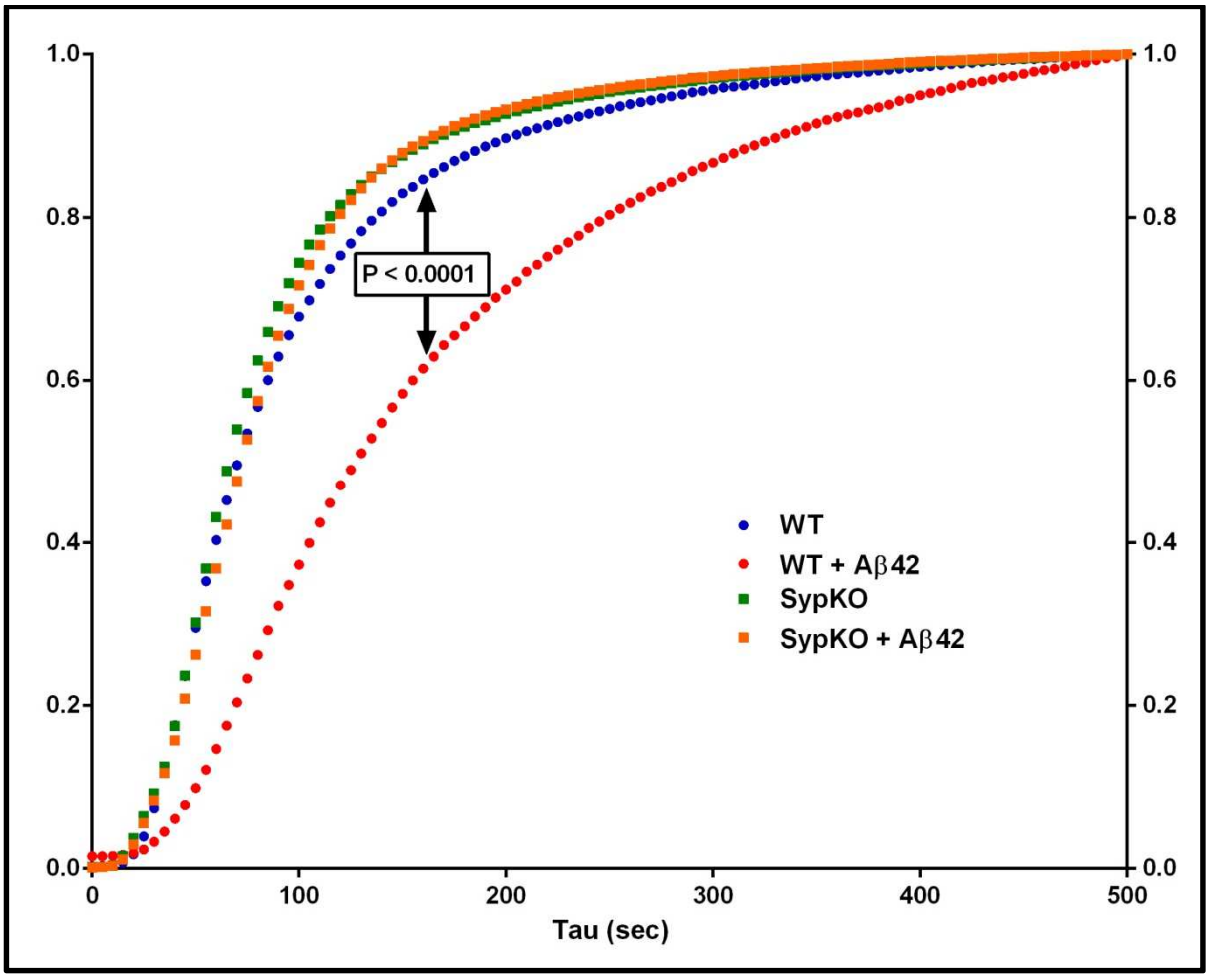

Figure 31: Cumulative Distributions of All Release Kinetics
Cumulative distribution function for all conditions. KS test reveals no significant difference amongst WT, SYPKO and SYPKO + Aβ42 ($p > 0.5$) but highly significant shift from WT to WT + Aβ42 ($p < 10^{-4}$).

SYNAPTOPHYSIN PARALOGS COMPENSATE LOSS IN KO MICE

At least two mammalian paralogs of SYP can functionally substitute in *SYP -/-* mice[14,80], which explains the subtlety of the phenotypes observed. The present study, as well as others[20,84], demonstrates that the cellular function of SYP requires binding to VAMP2, which is known to occur via their transmembrane domains (TMDs)[85]. This led us to predict that the other physin family members compensate

SYP loss through a shared ability to bind VAMP2 via their respective TMDs. As TMDs are not typically conserved with higher fidelity than other protein domains unless they are involved in oligomerization[86], we predicted that an unusually high sequence conservation of the TMDs across the physin family would be observed. Human SYP was aligned with its six neuronal paralogs (Figure 32 and Figure 33) and a conservation score was assigned at each position in the alignment. There are four obvious peaks of conservation which align directly with the four TMDs as shown by a standard hydropathy plot of SYP (Figure 34) demonstrating that those domains have been evolutionarily constrained by an important conserved function.

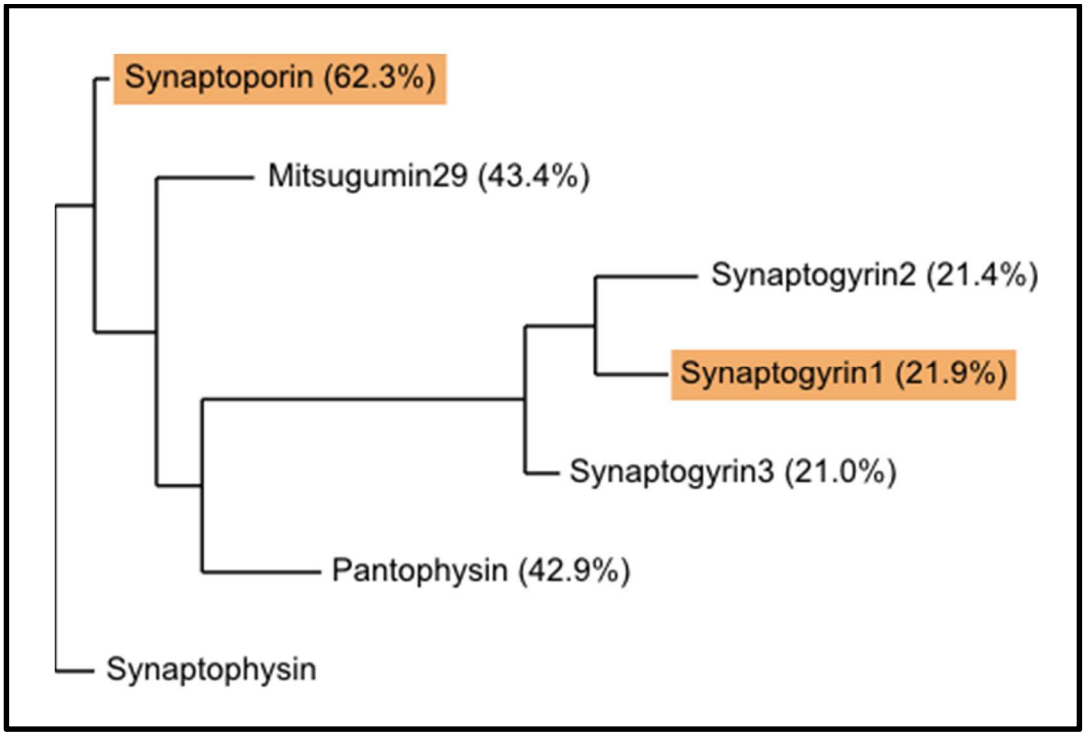

Figure 32: Physin Family Tree
PhyML tree for SYP and all 6 neuronal paralogs, identity to SYP indicated in parentheses. Homologs studied here are highlighted in orange.

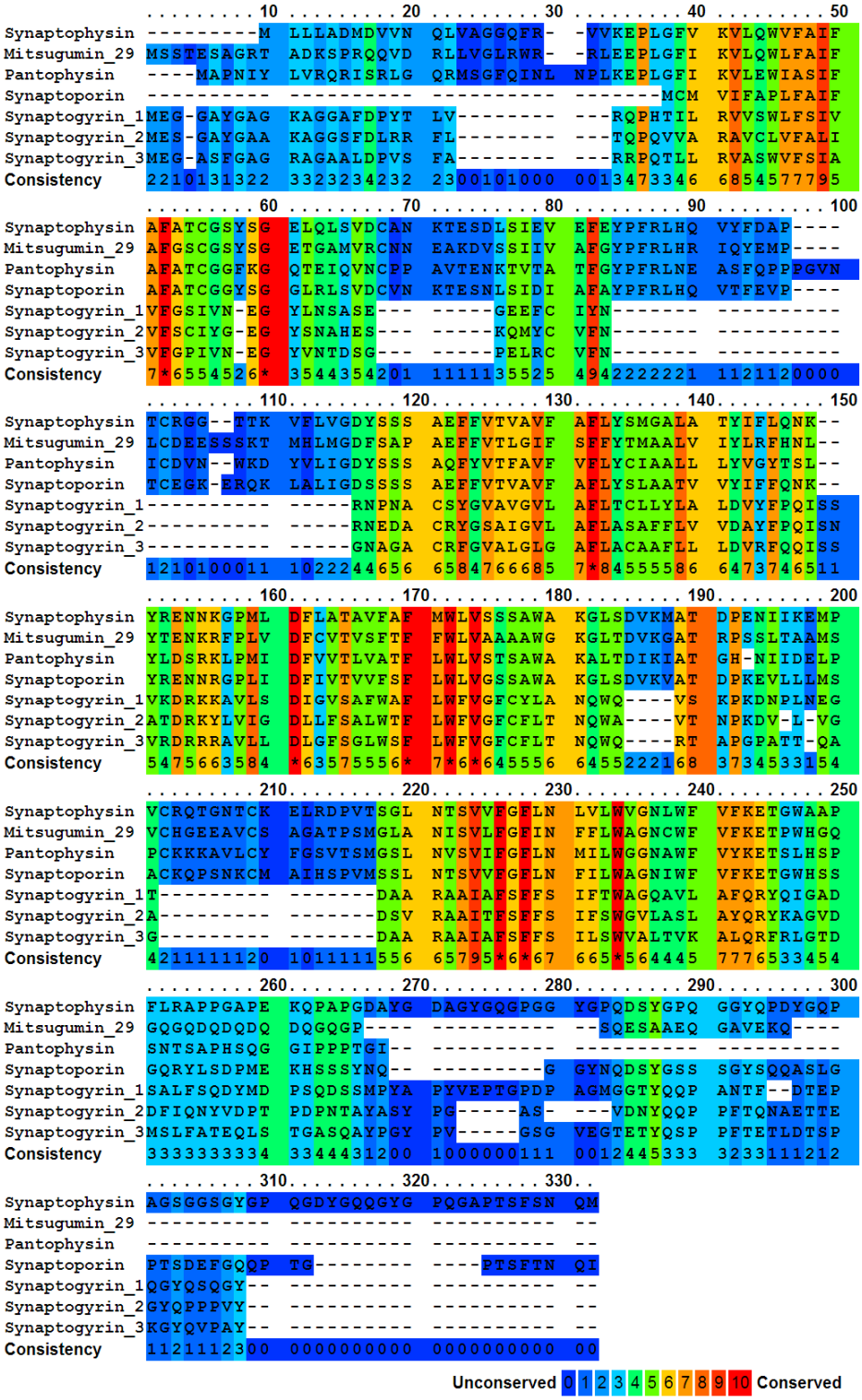

Figure 33: Physin Family Protein Sequence Conservation

ClustalW alignment of human SYP and neuronal homologs colored by conservation at each position assigned by the PRALINE server using the BLOSUM62 similarity matrix.

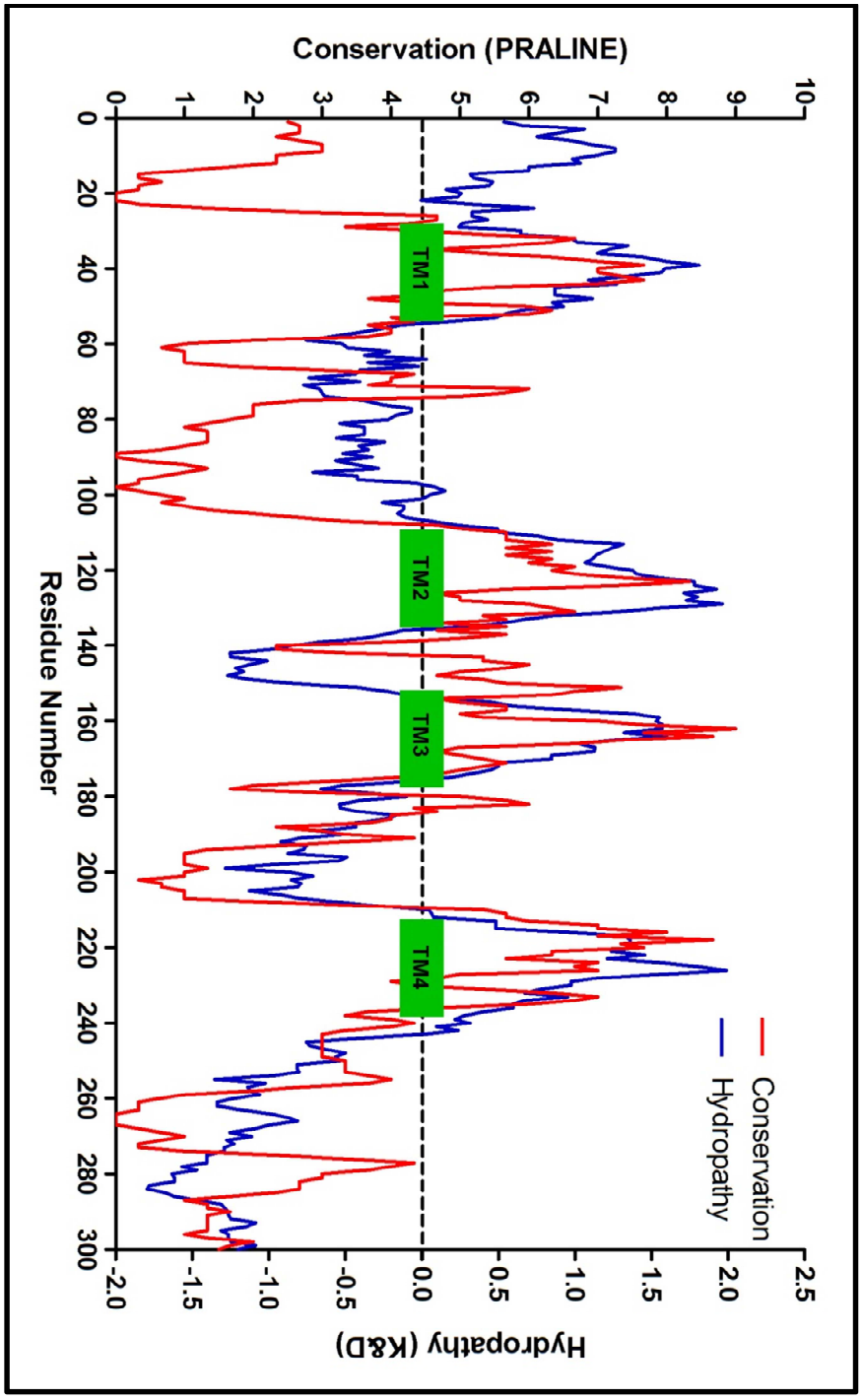

Figure 34: Physin Family TMDs are Conserved
Conservation score of physin family alignment (red) overlaid with SYP hydropathy score by Kyte & Doolittle method (blue) and TMDs indicated by green boxes.

Of the mammalian SYP paralogs, synaptoporin is the most similar and an overlapping role in plasticity has been reported for synaptogyrin1[14], so we evaluated these candidates for ability to substitute in *SYP* -/- mice. Synaptogyrin1 is expressed at very low levels in the wildtype brain whereas synaptoporin is moderately expressed. We observed that both proteins were present at much higher levels in mice lacking SYP (Figure 35). To functionally test the prediction that these proteins also bind VAMP2 we performed a co-immunoprecipitation experiment and, we observed significant copurification of both synaptoporin and synaptogyrin1 with VAMP2 in *SYP* -/- animals (Figure 35).

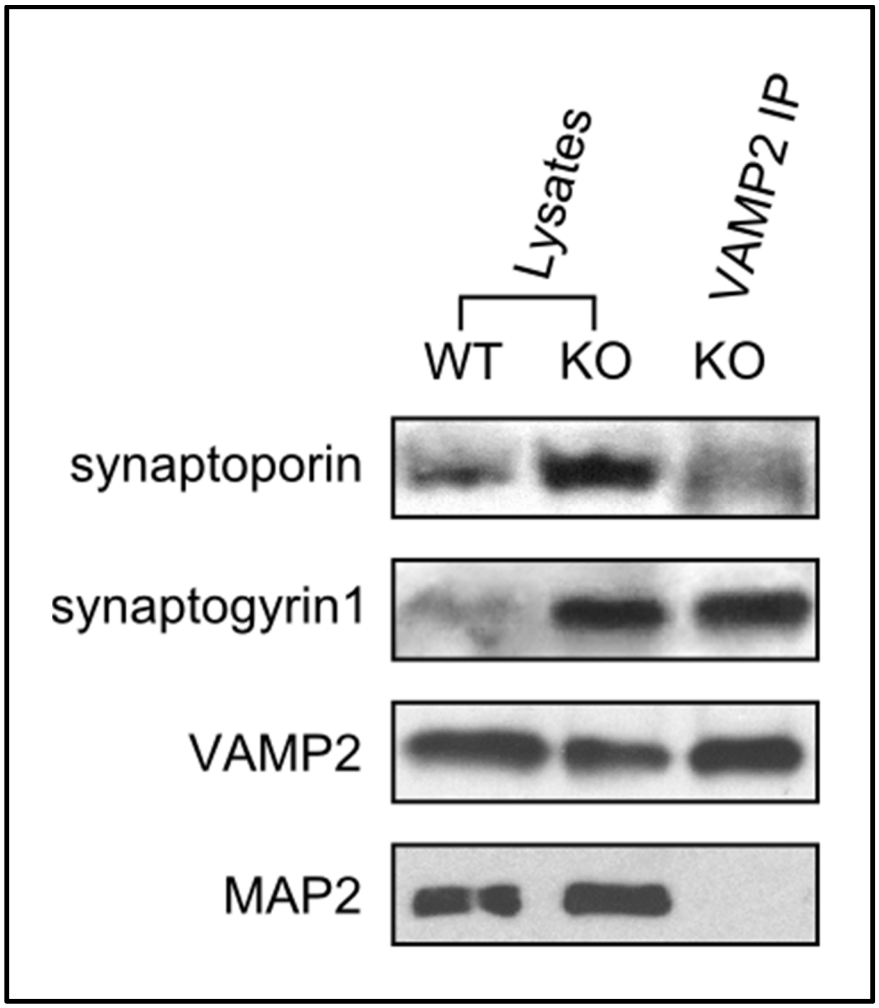

Figure 35: Physin Family Members Substitue in SYP KO
Endogenous levels of synaptic proteins probed from B6 and SYP -/- whole brain synaptosomes. SYP -/- synaptosomes were immunoprecipitated with αVAMP2 and probed for synaptic proteins.

SYNAPTOPHYSIN PRE-CLUSTERS SIX VAMP2 DIMERS FOR EFFICIENT FUSION

It is well established that SYP exists as a homohexamer resembling a channel pore[5,78] but unknown if VAMP2-bound SYP also exhibits this 3D architecture. To gain structural insights into the mechanism by which SYP activates vesicle fusion, we isolated the native SYP/VAMP2 complex from bovine

brain to high purity (Figure 36). Densitometry of protein bands reveals a 1.37 mass ratio of SYP:VAMP consistent with a 6:12 stoichiometry, which would be expected to show a 1.35 ratio based on total number of amino acids. This led us to a model of the complex containing exactly six VAMP2 dimers bound to a single SYP hexamer.

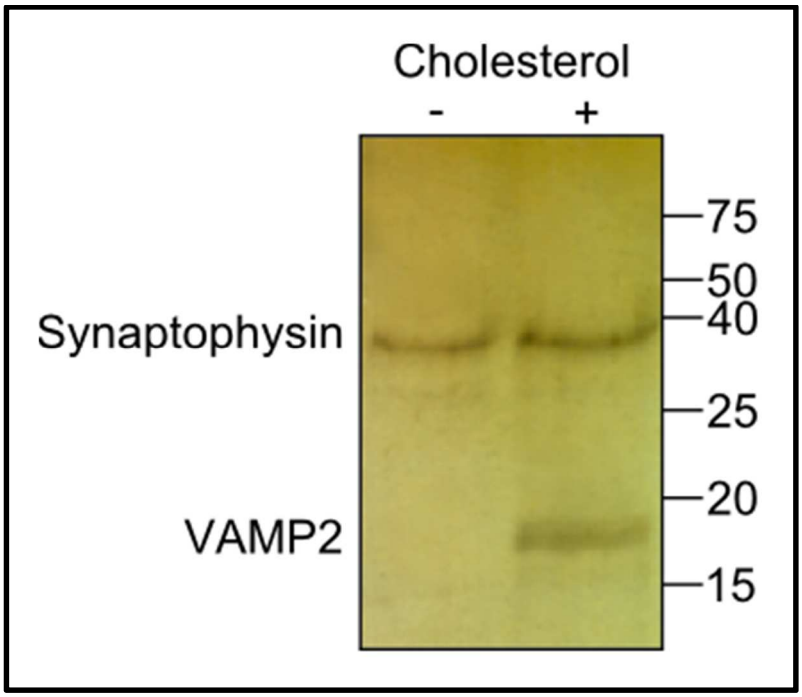

Figure 36: Purity and Stoichiometry of SYP/VAMP2 Complex
Native SYP and SYP/VAMP2 complex was purified from calf brain and analyzed by SDS-PAGE and silver stain.

Purified SYP/VAMP2 complex was then prepared by negative stain for structural analysis by electron microscopy (Figure 37). The high purity of the native complex observed by silver stain was corroborated by the raw micrograph which showed very few particles which did not appear to represent the hexameric pore structure. Using the EMAN software package, 3D structure determination was accomplished by first selecting particles; each of which is an identical copy of the

same protein complex In total, over 1200 particles were used in the analysis. These particles were then sorted into classes of similar particles. It is assumed in the analysis that similar particles are views of the subject from the same angle. Therefore, particles within a class were aligned and averaged to increase signal to noise and contrast resulting in a set of class-averaged particles (Figure 38). The class averages each represent a refined 2D projection of the 3D protein complex from a distinct angle. From these projections the EMAN software package can back-calculate the shape of the 3D object that might lead to those projections. Finally, a bootstrapping refinement process was carried out to generate the final density map at approximately 28 Å resolution (Figure 39 and Figure 40).

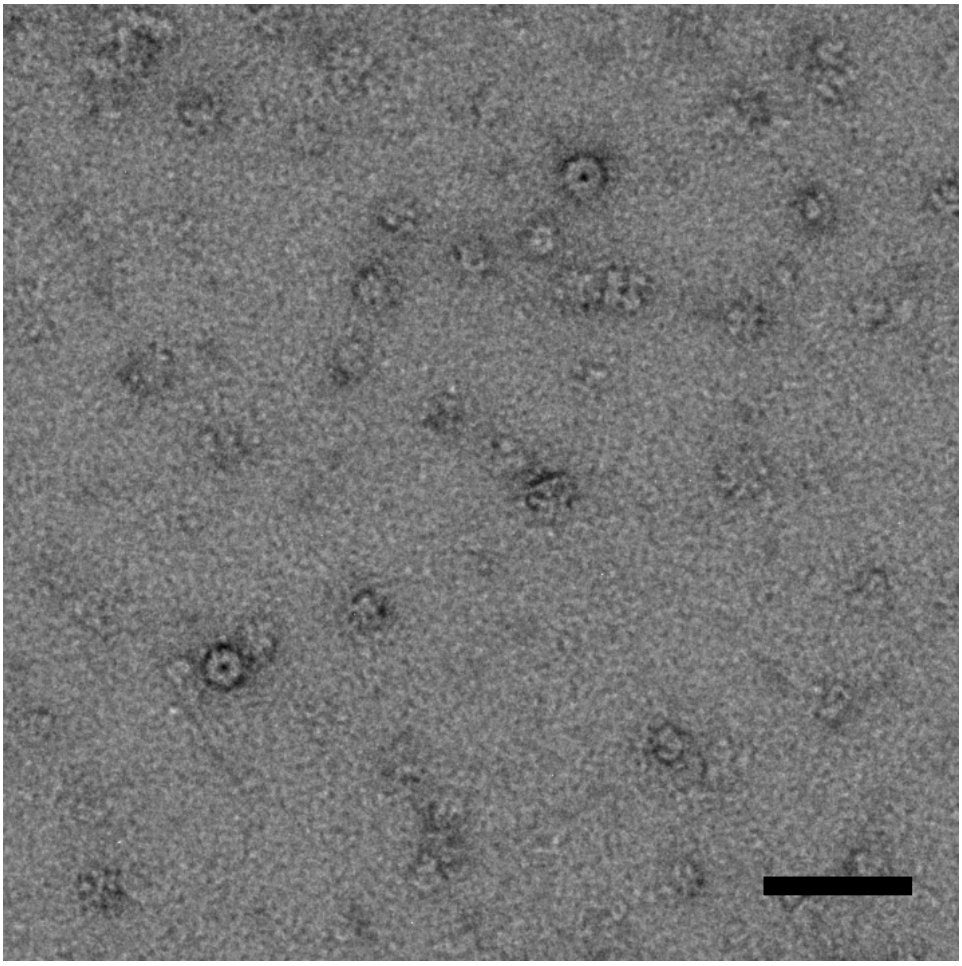

Figure 37: Negative Stain EM of SYP/VAMP2 Particles
Representative raw micrograph of negative stained protein. Scale bar = 50 nm.

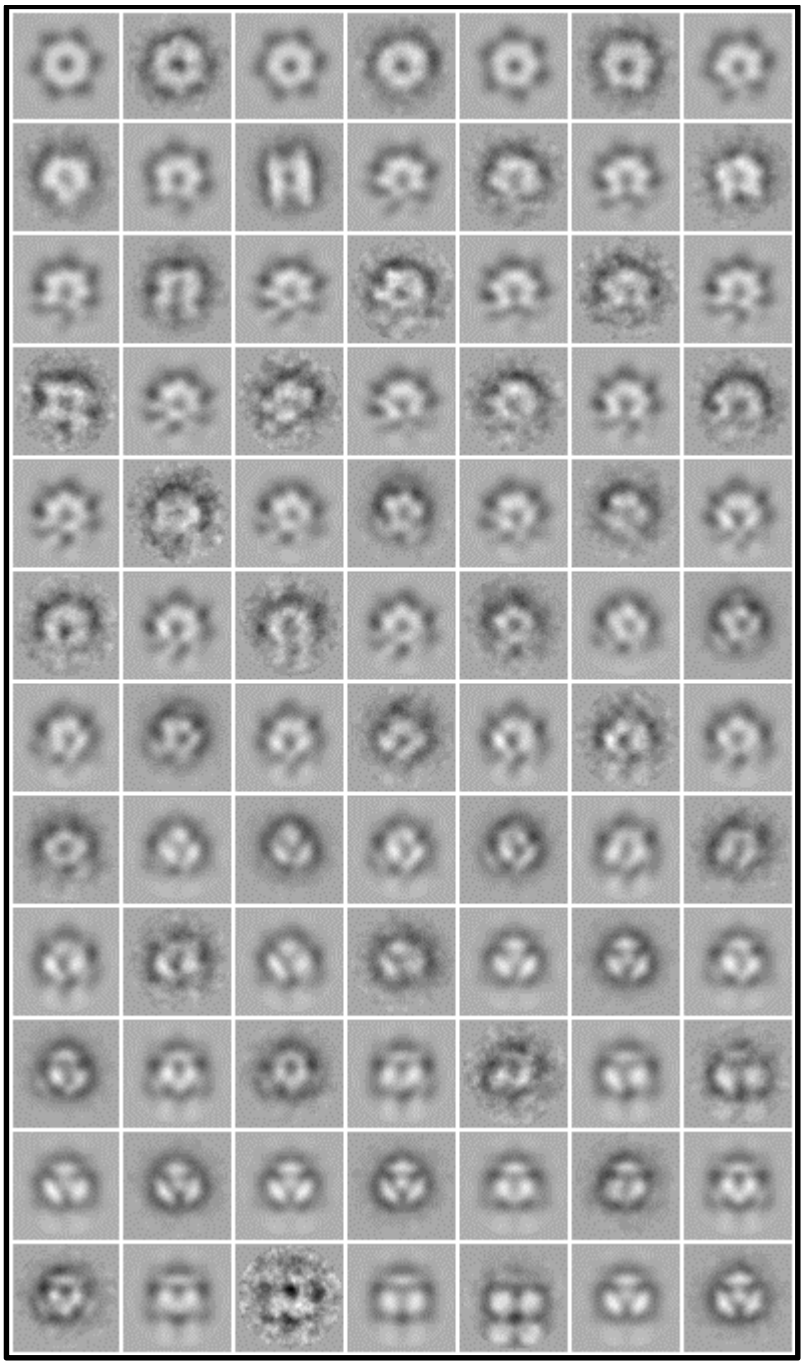

Figure 38: Class Averages of SYP/VAMP2 Complex
1232 particles were selected and grouped into classes. Each class of particles was averaged to produce class averages which were used to generate a final refined density model.

The SYP/VAMP2 complex shows 6-fold symmetry that resembles the previously described SYP structure[5] with six spokes radiating from a central hub. The outer diameter of the complex is 7.0 nm and the height measures roughly the same dimension.

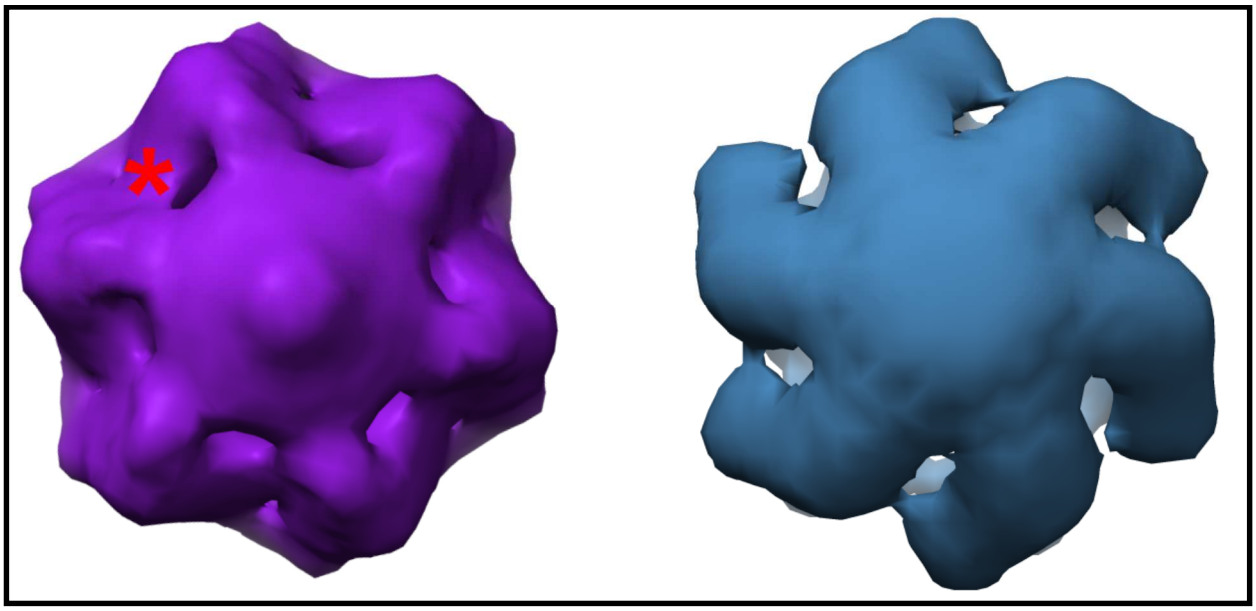

Figure 39: 3D Density Map of SYP/VAMP2 Complex – Top View
View from cytoplasmic face of EM density map of native SYP/VAMP2 complex (purple) or synaptophysin alone[5] (dark blue). Red asterisk indicates density corresponding to VAMP2 dimers.

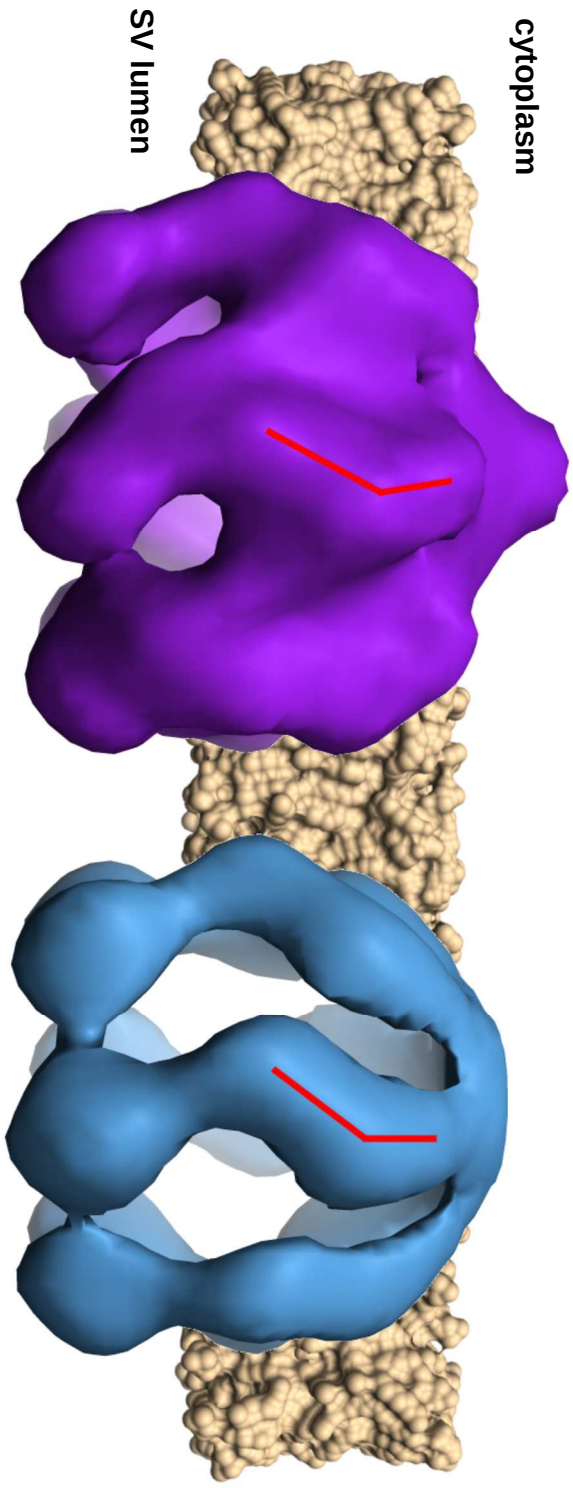

Figure 40: 3D Density Map of SYP/VAMP2 Complex – Side View
Side view of EM density map of native SYP/VAMP2 complex (purple) or synaptophysin alone[5] (dark blue). Red line indicates approximate centroid of the 4 helix TMD bundle of SYP.

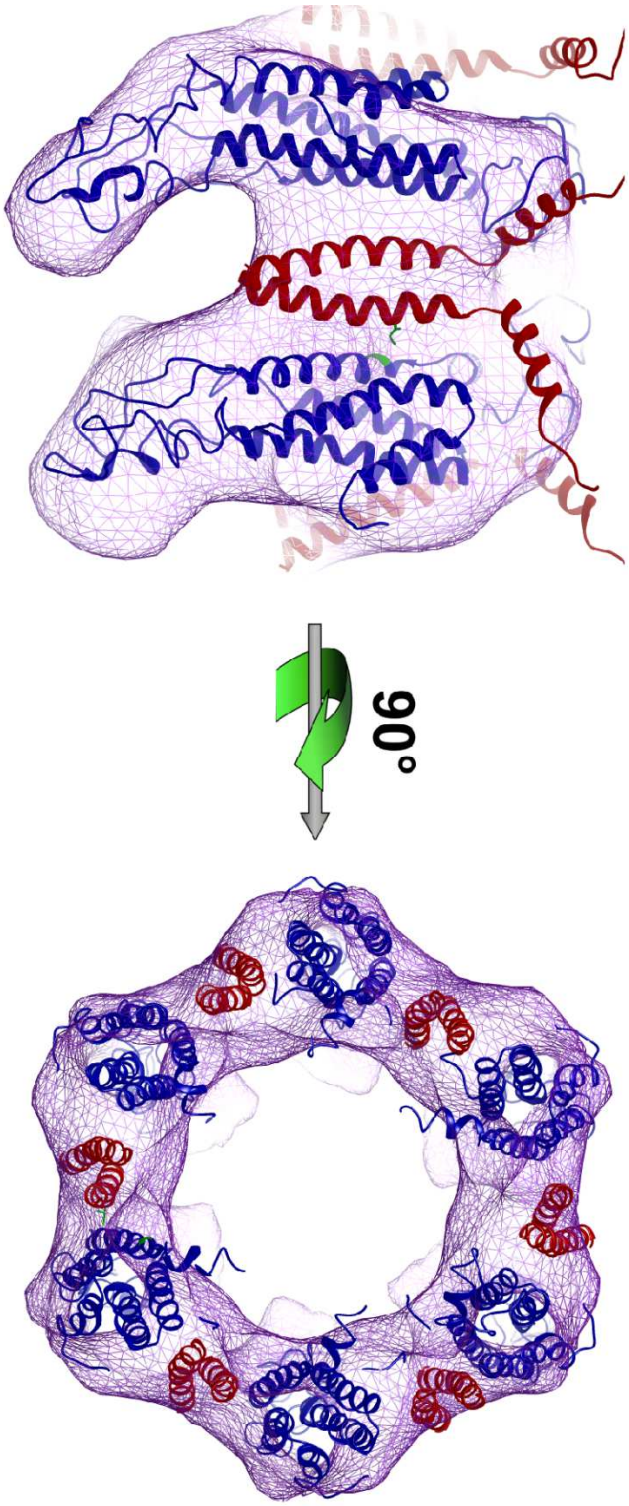

Figure 41: Docked High-Resolution Model with EM Density
High resolution model of SYP (blue ribbon) and VAMP2 (red ribbon) docked into EM density map (blue mesh) at the determined 6:12 stoichometry.

Based on hydrophobicity alignment to the gap junction protein connexin, which is a structural homolog of the synaptophysin hexamer, we were able to thread the SYP backbone onto the connexin26 structure[87] and then add sidechains and fit the model into our EM density data. Next, we docked the NMR structure of VAMP2[88] into our model with the transmembrane helices of the dimer inserted between the SYP molecules (Figure 41 and Figure 42). The SNARE domain of VAMP2 is too flexible to be observed in our EM structure so it is modeled outside of the density map.

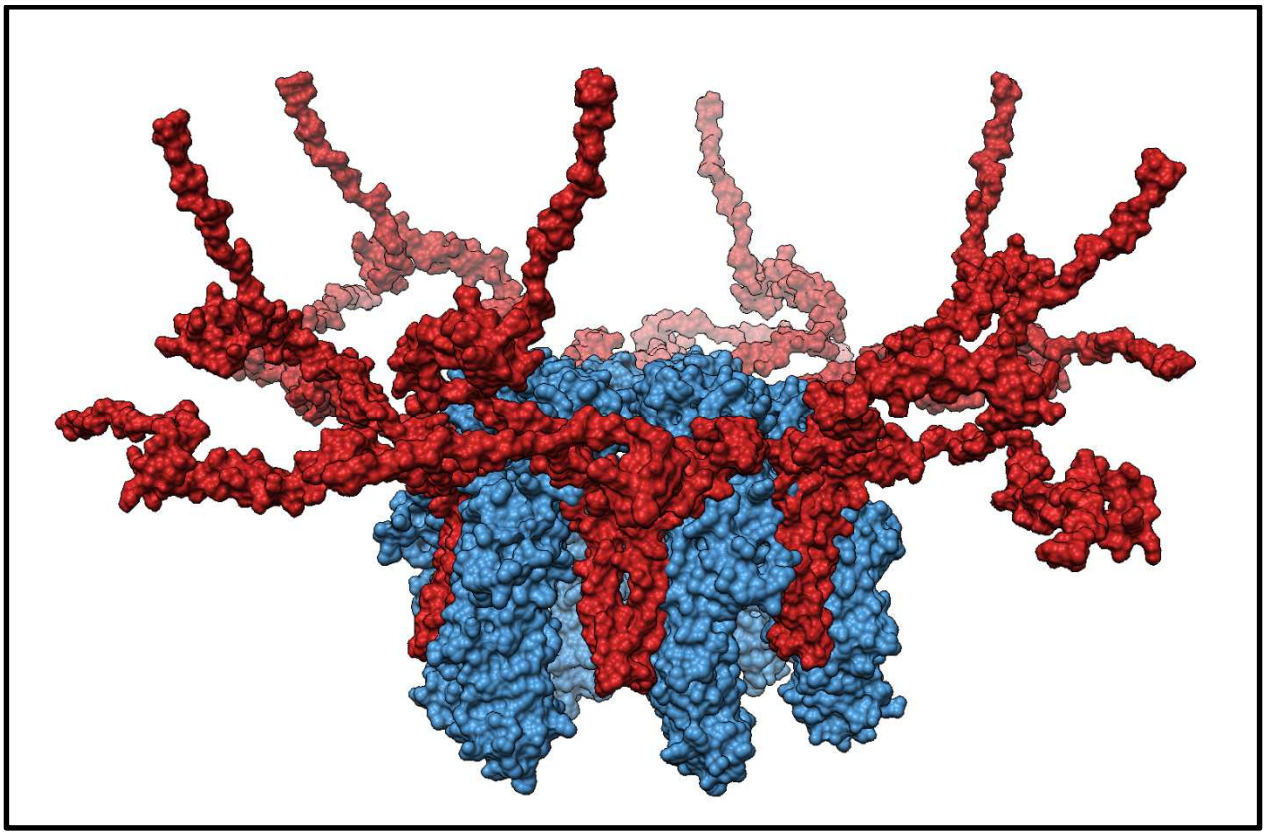

Figure 42: Space-Fill Rendering of High-Resolution Model
Space-fill rendering of the complete SYP_6VAMP2_{12} pre-fusion v-SNARE complex. SYP is blue and VAMP2 is red.

CHOLESTEROL BALANCES AB42 REGULATING THE SYNAPTOPHYSIN/VAMP2 COMPLEX

The connection between the Alzheimer's peptide Aß42 and SYP goes beyond the direct physical interaction shown here. The synaptic vesicle membrane is about 45% cholesterol[13] which is critical to the stability of the SYP/VAMP2 complex. Reduction of membrane cholesterol in neuronal cultures results in a loss of SYP/VAMP2 binding[89] very similar to the perturbation caused by Aß42. As predicted from our results, this cholesterol depletion recapitulates the vesicle release failure induced by amyloid disruption of the pre-fusion SNARE complex[90]. Neurons can tolerate as much as 40% reduction in membrane cholesterol without impacting viability, but this treatment significantly potentiates the neurotoxicity of Aß[91]. Furthermore, supplemental cholesterol confers a dose-responsive protection against this toxicity demonstrating that the converse of this synergistic relationship also holds[91]. Both cholesterol depletion and Aß42 peptide represent pleiotropic biochemical insults to the neurons, but both modulate the SYP/VAMP2 complex and these data suggest that this pre-fusion structure may be the link between the two. In addition to directly antagonizing SYP/VAMP2 binding, Aß42 also indirectly weakens this interaction by depleting membrane sterols in its activity as a potent cholesterol oxidase[92]. In opposition, cholesterol not only stabilizes SYP/VAMP2 independently of Aß42, but we saw that the more aqueous-soluble hemisuccinate form directly attenuated SYP binding to the peptide in a concentration dependent

fashion (Figure 44). We conclude that at least part of the acute cholesterol protection from Aß42 is due to these two activities maintaining the normal function of the SYP/VAMP2 complex.

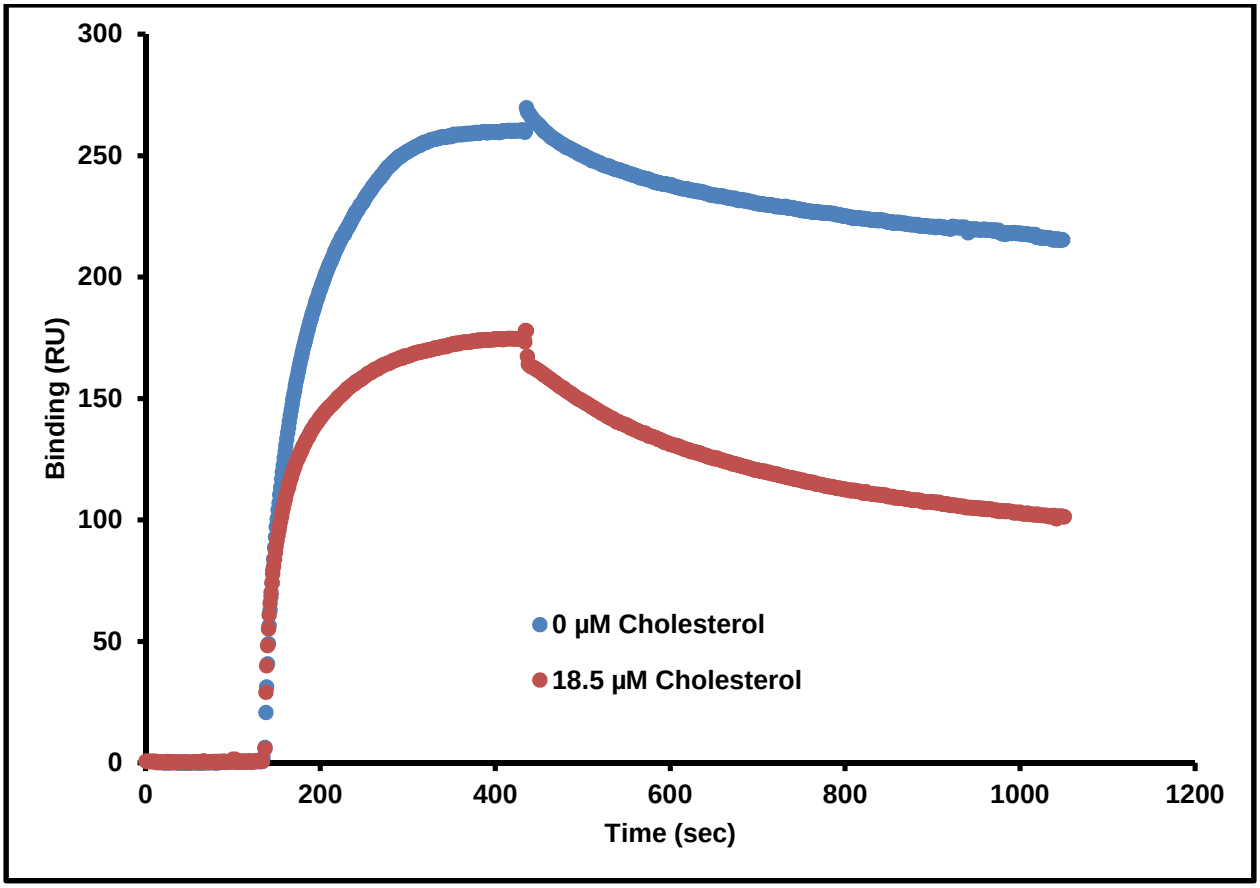

Figure 43: Cholesterol Inhibits Aβ42 Binding to SYP
Representitive sensorgrams of 40 µM SYP binding to immobilized Aβ42 with or without cholesterol in the buffer.

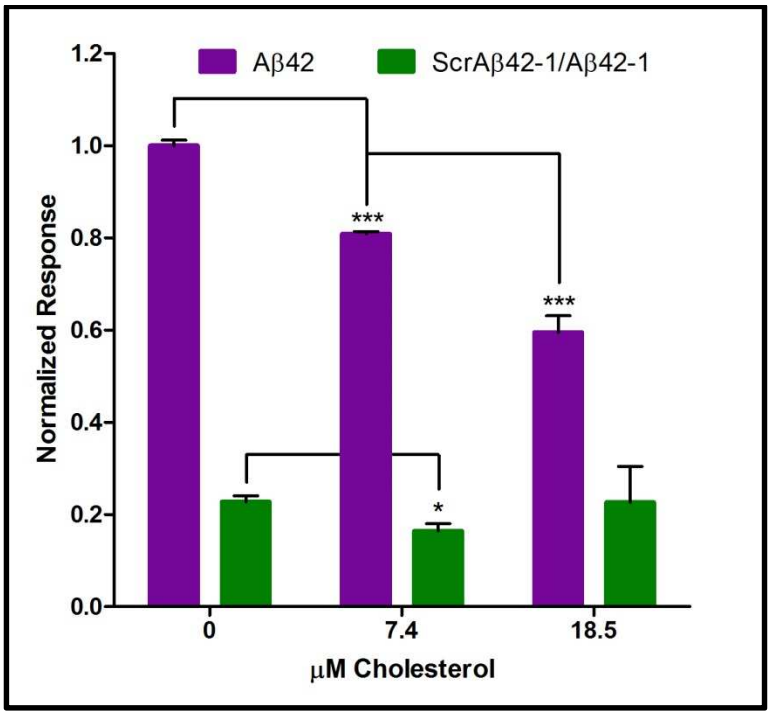

Figure 44: Cholesterol Inhibits Aβ42 Binding to SYP
Normalized maximal binding of SYP to Aβ42 at increasing cholesterol concentration. Mean of 3 experiments, maximal binding defined as maximum RU value attained during association phase of sensorgram. Representative traces shown in Figure 43.p < 0.001 (***); p < 0.05 (*).

DISCUSSION

Many cellular proteins have been shown by various assays to interact with Aβ42[64,66,93], so we first sought to confirm a report that SYP was also able to interact with the peptide[81]. In agreement with previous findings we observed robust binding of SYP to the immobilized peptide by western blot but also found significant binding of other proteins by silver stain. Because many of the bands in the column retentate appear to simply be high abundance proteins also visible in the input, one might suspect non-specific binding, but a similar degree of binding for those proteins is not observed in the scrambled peptide column. From this we conclude that structural

features unique to Aß42 and independent of amino acid composition mediate this apparent promiscuity. It is also possible, despite efforts to bind pre-aggregated peptide onto the column, that the Aß42 peptide was able to partially assemble into protofibrils or other form which might facilitate non-specific protein binding preferentially over the scrambled peptide. Indeed some of the reports of Aß42 interacting proteins have been specific to more aggregated forms[66] which contain unique interaction interfaces. The wash conditions were gentle in this experiment (150 mM NaCl, 0.5% NP-40), so it would be interesting to try a range of elution conditions to see if the binding species could be further fractionated and characterized. The large number of proteins bound out of the synaptosomal lysate would make it difficult to gain any specific insights towards biological targets via a discovery oriented approach but more stringent washes may allow this type of methodology. Specifically, if increased stringency in the wash conditions reduced the number of bound proteins, it might be possible to use tandem MS-MS mass spectrometry to identify and quantify the bound proteins to generate a list of all synaptic proteins which bind Aß42. This unbiased approach may implicate previously unknown cellular targets of Aß42 which may play an important role in AD. However, despite some promiscuous binding, we found that the SYP-Aß42 interaction did display some specificity. Another neuronal protein MAP2 was used as a control and showed no binding to either column. VAMP2 which is another highly abundant SV membrane protein like SYP also failed to bind, further supporting the specificity of this interaction. This is consistent with a previous

report that other synaptic proteins PSD95 and SNAP25 also fail to bind Aß42 *in vitro*[81]. Finally, we probed for homologs of SYP which didn't bind from WT lysates where they are poorly expressed, but also showed no binding out of SYP KO lysates where they are dramatically upregulated. Because of the high similarity of these proteins, we conclude that interaction with Aß42 requires some specific and unique contacts which SYP does not share with its homologs. This binding specificity causes us to predict that SYP is a specific target of Aß42 peptide and that the related proteins would not share this susceptibility.

Using SPR we observed extremely tight binding of SYP to Aß42. Under the conditions used to immobilize Aß42 to the SPR chip, it was observed to be pre-fibrilar by ThT fluorescence which indicates that this form can potently bind its target. This further supports the well documented observation that pre-aggregated Aß42 is the most toxic disease-relevant species[50–60] and that this binding event is biologically meaningful. The sub-nanomolar affinity of Aß42 for the native SYP hexamer predicts substantial binding at the concentrations of soluble Aß42 found in the brains of AD patients which typically fall in the low nanomolar range[94]. Furthermore, this affinity is tens to hundreds of times greater than previously described affinities of Aß42 for other purported neuronal targets[64,66,93] where binding affinities were determined from oligomeric and aggregating Aß42 which likely overestimates the true specific binding. The SPR measurements shown are normalized against baseline binding to a scrambled Aß42 chip showing that very little binding occurred consistent with our results from the Aß42 column.

It is well known that SYP and VAMP2 form a complex in SVs, however it is still somewhat unclear what the exact function of this interaction is. Consistent with many previous reports we observe robust co-purification when performing immunoprecipitation for either protein (Figure 25 and Figure 26). When neurons are treated with Aß42 in the media, it is found to localize to synapses[81], and the effects on synaptic proteins are of great interest. We observed that at 24 hours, 13 nM Aß42 reduced levels of intact SYP/VAMP2 complex but was not able to disrupt all copies of the highly abundant complex. This disruption may be a dose-responsive phenomenon but without further experimentation to titrate in Aß42 we cannot be sure. It is also possible that there are multiple subpopulations of the protein complex and that some may exist in a protected state whereas all vulnerable complexes were completely dissolved by the peptide treatment. It is also possible that the Aß42 peptide bound and disrupted the SYP/VAMP2 interaction rapidly upon treatment and that by 24 hours additional protein synthesis has overcome the initial loss of the complex and that the disruptive peptide has already been cleared or absorbed by the system. Regardless of the exact mechanism, it is clear that Aß42 dramatically reduces interaction of SYP with VAMP2. It has also been observed that extremely high concentrations of Aß42 can directly compete SYP off immobilized VAMP2 *in vitro*[81], so we predict that VAMP2 and Aß42 compete for a similar binding site on SYP. Failure to co-purify any VAMP2 along with the bound SYP on the Aß42 column (Figure 23) further supports the idea that association with VAMP2 and Aß42 are mutually exclusive.

To observe the impact Aß42 treatment and subsequent loss of SYP/VAMP2 has in synaptic release, we performed a series of FM destaining experiments. When interpreting this data it is important to remember that this assay reports a bulk measurement of release at each synapse rather than fusion events of individual vesicles. Thus, the overall release rate is a convolution of several subtly distinct steps in the life cycle of a synaptic vesicle. Because of the stimulation method, we are primarily observing fusion of a readily releasable pool of vesicles which appear to fuse serially until the vesicle pool is depleted[95]; so although we expect some natural variation in the exact kinetics of each quantal release event, the bulk measurement of exocytosis is a good proxy for the kinetics of individual release events.

The striking reduction in release kinetics induced by Aß42 treatment appears to be more than a simple slowing of the kinetics observed in the control. Rather, we observe the dramatic appearance of a new population of very slow ($\tau > 400$ sec.) synaptic release events not seen in the presence of scrambled peptide. A Kolmogorov-Smirnov analysis of the entire dataset shows a very significant difference with a $p < 10^{-4}$ (Figure 31). This result is consistent with the observation that Aß42-treated neurons have reduced pools of readily releasable SVs[96,97]. The Aß42 dose of 13 nM used here closely matches the observed concentrations of Aß42 in AD brains[94]. While this dose is many times lower than used in previous studies[81,96,97], the magnitude of the effect we observe is similar, suggesting a threshold effect. Presumably above a certain concentration, Aß42 either aggregates

into a less active high oligomer form, or that the biological system becomes saturated above this threshold.

Aß42 has many claimed targets in neurons which may mediate its potent neurotoxicity and devastating dysregulation of basic neuronal function and it is often difficult to pinpoint these broad phenotypes to any specific protein or signal. In this case, because the *SYP* -/- neurons are viable and healthy, we have the rare opportunity to assay for insensitivity to Aß42 as a measure of reliance on SYP for mechanism of dysregulation. The fact that Aß42 treatment of *SYP* -/- neurons has no significant impact on vesicle release indicates that SYP is absolutely required for the disruption we observed in WT neurons. We know that Aß42 binds extremely tightly to SYP and disrupts interaction with VAMP2, so it is likely that this action is responsible for the altered release kinetics we observed in WT neurons. All these data are consistent with a model wherein SYP functions to enhance the kinetics of SV fusion by binding VAMP2 and that disruption of this activity is one of the earliest events in the progression of AD.

The shared ability of at least two SYP homologs to bind VAMP2 adds further evidence in support of the redundancy seen by others[14,80]. Because VAMP2 and SYP bind via their TMDs[85] we hypothesized that specific perturbation of this region of the proteins would yield a similar functional deficit as we saw in our FM experiment. Although the TMD of VAMP2 was shown to be dispensable for the fusion reaction to occur, the kinetics of evoked release were decreased when the SNARE TMD was replaced with a lipid anchor[98], consistent with our hypothesis

that oligomerization via TMD interactions is required for normal kinetics by lowering the entropic barrier.

Synaptophysin is a highly abundant protein and there are many copies of its complex with VAMP2 in neurons, so for other family members to substitute in the KO mice, significant upregulation would be required. Consistent with this idea, we observed a significant developmental upregulation of both synaptoporin and synaptogyrin1. In the knockout mice, we also found robust association of these homologs with VAMP2, indicating that these proteins do functionally substitute *in vivo* by binding VAMP2 and enhancing release kinetics. Strikingly, these SYP paralogs do not appear to be direct targets of Aß42 (Figure 23) which explains why knockout of *SYP* ameliorates the kinetic defects caused by Aß42 treatment in wildtype neurons (Figure 28, Figure 30 and Figure 31). A direct prediction of this model is that SYP KO mice would be protected against synaptic release defects caused by Aß42 in AD. To test this prediction we plan to cross a transgenic AD mouse model onto the SYP KO background and assay for disease phenotypes. This particular approach does not have great potential in intervening with the human disease therapeutically, but may help us to understand how much of the AD phenotype is mediated by interaction of Aß42 with SYP.

Bovine SYP and VAMP2 both share very high identity with the orthologous human proteins (94.6% and 99.1% respectively) so we expect that the 3D density map of the complex at this resolution is generalizable to all mammals if not all vertebrates. When compared with the structure of SYP alone[5] two important

differences become evident. First, from the top (cytoplasmic face) it is obvious that there is new density between each of the six spokes of SYP which we attribute to the presence of VAMP2 dimers (Figure 39). At this resolution, it is difficult to discern any further detail about the exact interaction interface, but the map is at least consistent with the other data indicating that the interaction occurs in the membrane. Second, the density corresponding to the four-helix bundle of the SYP TMDs is tilted in the complex relative to the structure of SYP alone, indicating a structural rearrangement caused by binding of the SNARE protein (Figure 40).

Although reconstituted systems have allowed the observation of fusion mediated by single SNARE binding events[99], it has recently been demonstrated that biologically relevant SV fusion requires at least 3-6 SNARE interactions[100–104]. The contact patch of a fusing vesicle with the plasma membrane is roughly 180 square nm[95] which, at 35 copies per vesicle[13,70], yields less than a single VAMP2 dimer occupying that area on average. The SNAREs extend beyond the surface of the vesicle by about 12 nm which effectively augments this contact patch several fold, but this alone cannot generate coordinated binding of the required 6 SNARE pairs. Synaptophysin is found at 32 copies per vesicle[13] which, together with previous studies[18], suggests that its complex with VAMP2 is the predominant form of these proteins. From this, we predict that five or six near or perfectly stoichiometric complexes stud the surface of every readily releasable SV. By pre-clustering VAMP2 into a stable complex, SYP not only allows for presentation of the requisite number of SNAREs, but also makes the individual trans-SNARE binding interactions

cooperative. This physical model implies that the fusion pore would open at the center of the hexamer where we observe some extra density that may be a lipid plug lost at the instant of fusion. Furthermore, the inner diameter of our pore structure (~3.0 nm) and previous measurements of the conductance of the SYP pore[10] (415 pS) are consistent with direct measurements of the fusion pore[105] of ~2.3 nm and a conductance in excess of 375 pS. These results demonstrate that the SYP/VAMP2 complex represents the physiologic pre-fusion state of the v-SNARE which, together with the docking of accessory proteins, is responsible for the extremely fast kinetics of the release event[106].

From our high resolution structural model, we can more closely observe the interaction interface of SYP and VAMP2. The clinical mutation in SYP, G217R, associated with X-Linked Intellectual Disability[107] is found on the 4th transmembrane helix of SYP and appears at the probable interface with the VAMP2 helix (Figure 45). Glycine 217 is conserved in all vertebrates examined and represents a pocket on SYP that may accommodate the side chain of VAMP2 Ile 98. We predict that replacement with a relatively bulky arginine at position 217 would severely attenuate the ability of SYP to coordinate VAMP2 into its pre-fusion state and modulate release kinetics. This acute cellular defect may underlie the developmental and cognitive impairments observed in patients with that mutation.

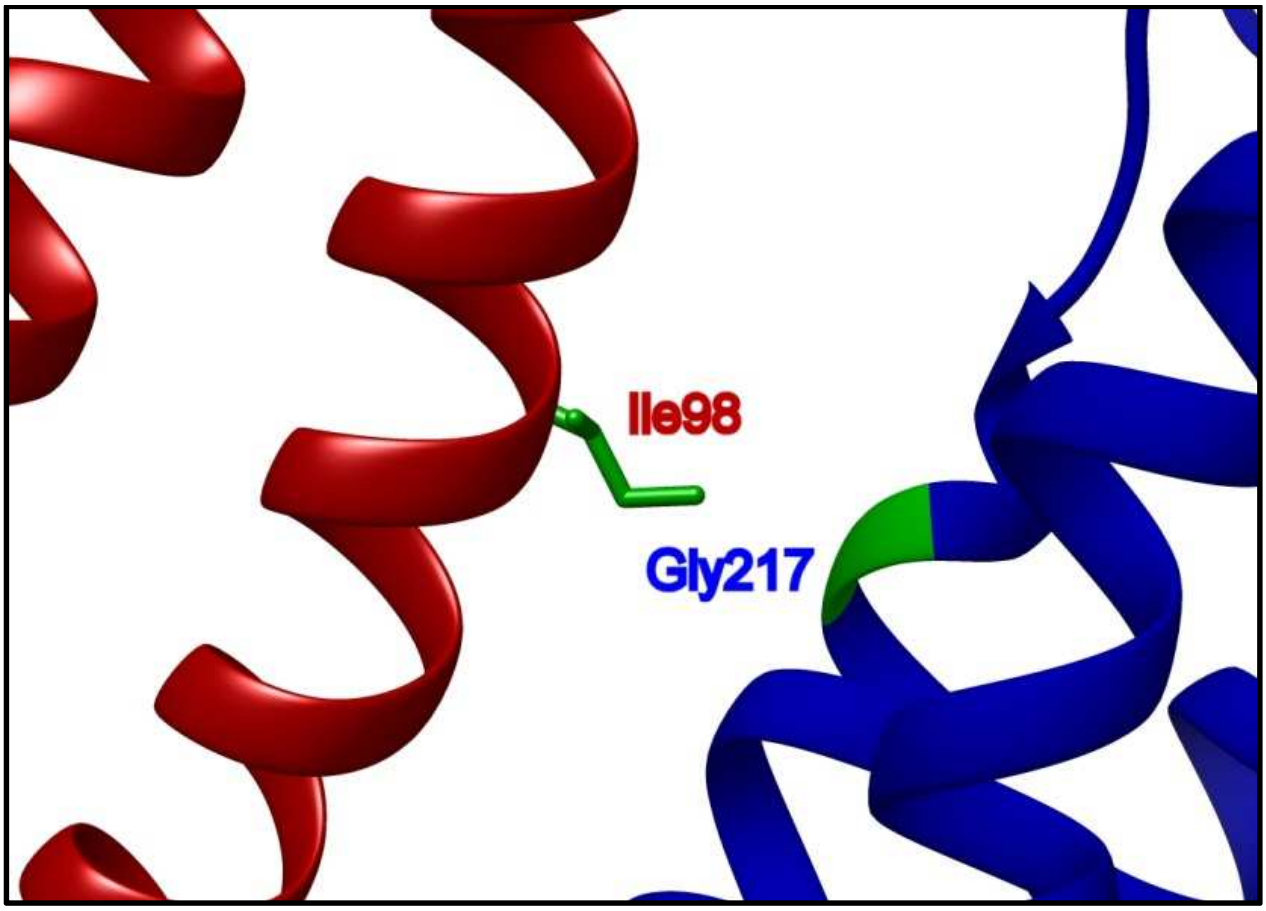

Figure 45: SYP XLMR-Associated G217R Mutation
Helical packing interface between SYP and VAMP2 near SYP G217 (blue ribbon) and VAMP2 I98 (red ribbon) which in SYP is the site of the clinical XLMR-associated G217R mutation. This mutation is expected to create a clash with VAMP2 I98 and disrupt the SYP/VAMP2 complex.

Our data informs a new model describing the complete life cycle of the synaptic v-SNARE VAMP2 shown below. Unlike many other SNARE-mediated fusion events, SV release requires exquisitely tight temporal coupling of fusion with Ca^{++} influx. We propose that this event features additional catalytic mechanisms not found in general fusion pathways. Without pre-ordering SNAREs in the vesicle, exocytosis still requires multiple trans-SNARE contacts, but these can only be made

at significant entropic cost thereby impeding physiologic fusion kinetics. This entropic cost is paid in electrostatics and hydrophobic forces upon binding to SYP early in the vesicle cycle, which bears fruit when a ring of 12 SNAREs can simultaneously dock at the membrane to rapidly open a fusion pore upon Ca^{++} influx. Based on this previously undescribed activity, SYP can now be thought of as an entropic catalyst of neurotransmitter release. Assembly of the pre-fusion pore appears to be rate-limiting, consistent with evidence that structured arrays of t-SNARE proteins, which may mirror the structure presented here of the pre-fusion v-SNARE complex, serve as the docking sites of vesicles[108–110]. The SYP/VAMP2 interaction is labile relative to the bundled SNARE trimer and these are known to be mutually exclusive molecular contexts for VAMP2[111]. According to our model, this is essential to allow fusion when VAMP2 finally contacts syntaxin-1/SNAP-25, so we propose that SYP/VAMP2 binding is just strong enough to hold VAMP2 together until it docks with the t-SNAREs and accessory proteins. SV fusion with reconstituted membranes displayed comparable kinetics to synthetic liposomes[112] but the conditions were not consistent with maintenance of the SYP/VAMP2 interaction[111]. Therefore, we predict that vesicles with natively reconstituted pre-fusion v-SNARE complexes of SYP/VAMP2 would show enhanced fusion kinetics in *in vitro* assays but to date this has not been tested. Evidence for the proposed catalytic activity of SYP has remained elusive because multiple functional homologs can substitute for SYP in knockout animals and experimental conditions suitable for observing the effects of entropic catalysis are not readily available.

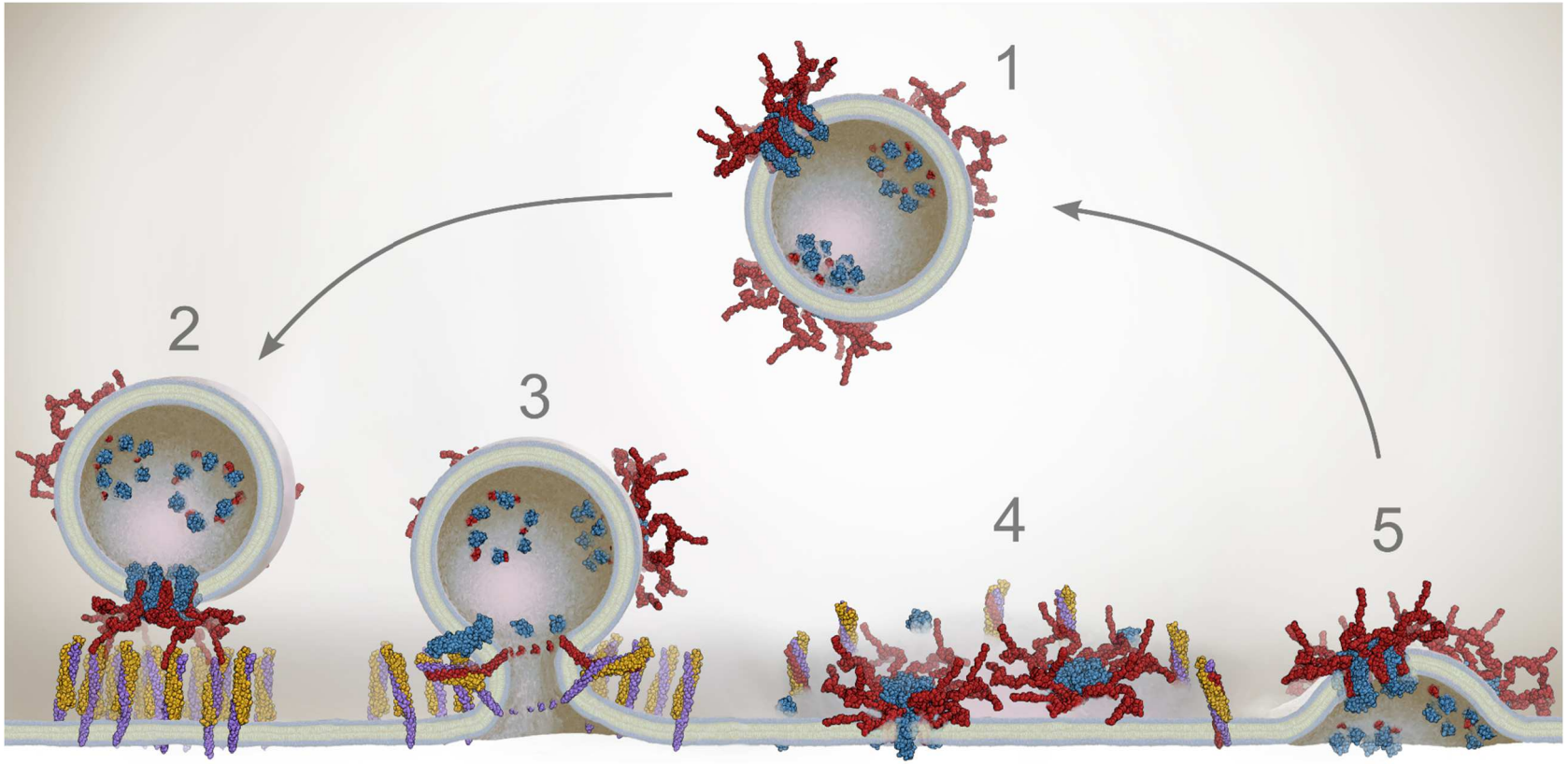

Figure 46: Life Cycle of v-SNARE VAMP2

(1) Mature SVs contain 5 or 6 complete SYP/VAMP2 complexes. (2) SVs are trafficked to the active zone where accessory proteins mediate docking of clustered VAMP2 (red) with ordered arrays of the t-SNARE complex of syntaxin-1 (purple) and SNAP-25 (gold). (3) Calcium influx induces SNARE zippering as SYP (blue) dissociates from VAMP; the fusion pore opens and neurotransmitter is released. (4) The post-fusion SNARE assemblies[67] and disassociated SYP molecules ring the membrane patch contributed by the SV, which contains the intact SYP/VAMP2 complexes not involved in the fusion reaction. (5) NSF disassembles the SNARE bundles and t-SNAREs return to the active zone. SV components are loaded into clathrin coated pits where the SYP/VAMP2 complex reforms. Endocytosis recovers the SVs for subsequent loading and fusion.

The pathologic interaction of Aß42 with normal neuronal function is a complex and diverse set of processes, making it difficult to tease out specific cascades of biochemical events. In general, Aß42 leaves the site of cleavage and can either accumulate extracellularly, or directly reenter the cell via association with lipid rafts and endocytosis or receptor interactions[113]. By reentering the bouton, the peptide is almost immediately in contact with the synaptic machinery, so we propose that the disruption of vesicle release we observe may underlie the plasticity defects seen in hippocampal slices as early as 20 minutes after Aß introduction[47,61]. Cognitive impairments appear to precede loss of synapses and cell death[114], so these subtle alterations in neuronal function may well be upstream of other pathologies. In addition to the impacts we report on exocytosis, Aß42 targeting of dynamin-1 has been reported to disrupt SV endocytosis[115]. Others have reported subtle impacts to multiple steps in the synaptic vesicle lifecycle rather than a single major phenotype[116]. Because preparations of Aß42 peptide are known to be so highly variable, one explanation for these diverse observations could be that different forms of the peptide have subtly differing affinities and potencies amongst various synaptic targets. Because we observe efficient loading of vesicles in our FM assay, in our hands it is release that appears the most highly sensitive to Aß42 in the synapse. Our data is not inconsistent with subtle effects on other aspects of vesicle trafficking, but they are below the threshold of detection by the assay we used.

Here, we have demonstrated that the peptide creates a range of kinetic phenotypes at different synapses: from fast and fully wildtype, to almost completely

arrested, as well as a spectrum of rates in between (Figure 28). We propose that these kinetic intermediates represent structural intermediates of the pre-fusion SNARE complex with 5, 4, 3 and 2 copies of the VAMP2 dimer clustered in the vesicle leading to partially catalyzed fusion (Figure 46). This structural heterogeneity is also evidenced by biochemical data showing incomplete dissolution of the SYP/VAMP2 complex under identical Aß42 treatment (Figure 25 and Figure 26). Our findings support the paradigm that SYP binding and dysregulation of vesicle fusion by Aß42 is an early causal step in AD which lies far upstream of the many other pathologies associated with the disease. While our observations are an important step in understanding AD, substantial future work will be needed to fully understand the pleotropic complexities of Aß42 in disease progression.

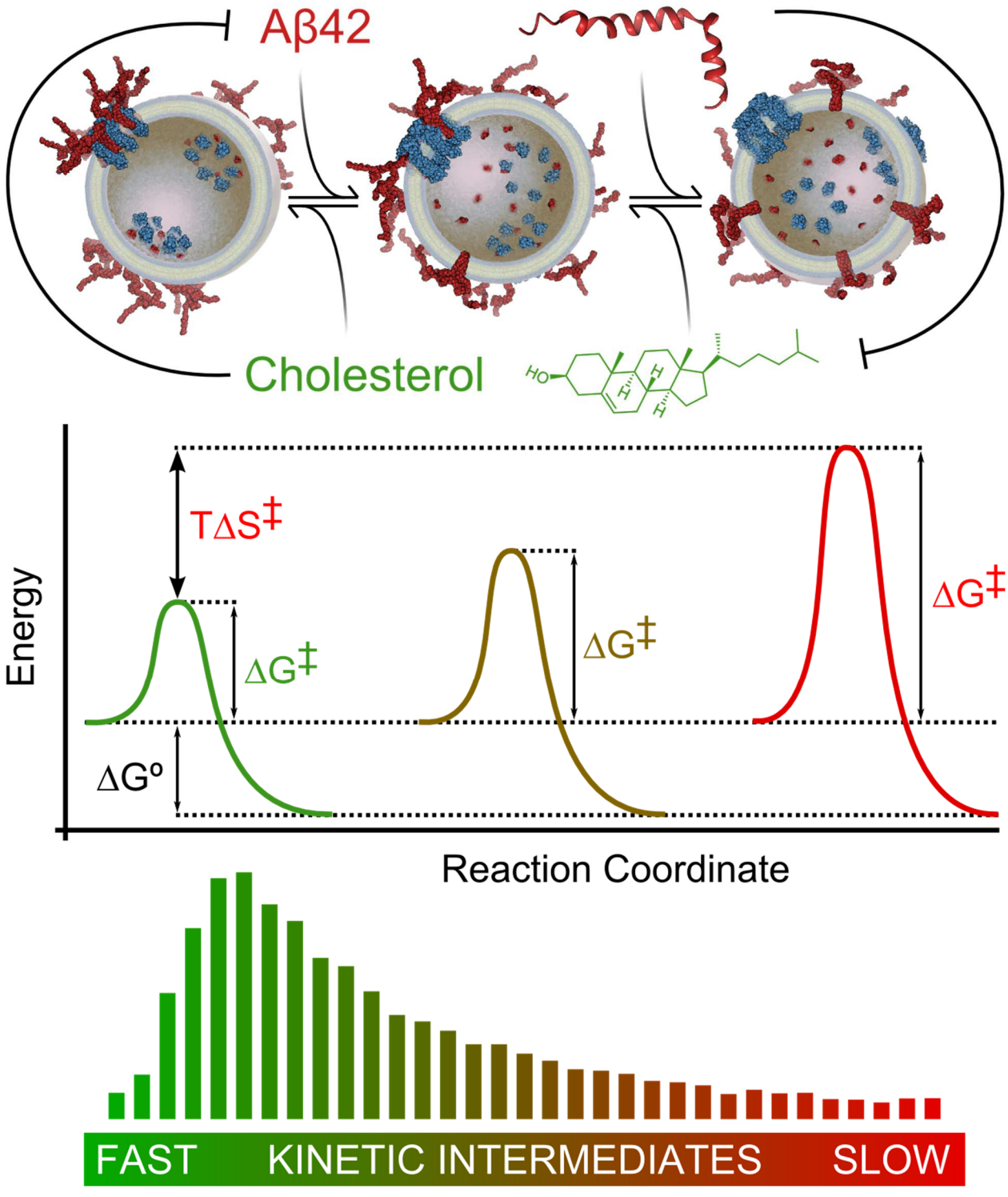
Aβ42
Cholesterol
HO
Energy
TΔS‡
ΔG‡
ΔG‡
ΔG‡
ΔGº
Reaction Coordinate
FAST
KINETIC INTERMEDIATES
SLOW

Figure 47: SYP Catalysis is Targeted by Aβ42 and Regulated by Cholesterol
We observed an equilibrium between the assembled (upper left) and disassociated (upper right) forms of the SYP/VAMP2 complex with cholesterol favoring the former and Aβ42 leading to the latter. Cholesterol and Aβ42 are also mutually antagonistic by mechanisms independent of the pre-fusion v-SNARE complex. Aβ42 induces structural intermediates, partially assembled SYP/VAMP2 complexes, incapable of complete entropic catalysis of fusion (center) resulting in intermediate kinetic phenotypes (bottom & Figure 28).

ACKNOWLEDGMENTS AND ATTRIBUTIONS

The work presented in this chapter was a collaboration of several members of Michael Stowell's lab with his direction and guidance. All SPR experiments were carried out and analyzed by Stephen Eisenberg using recombinant SYP generated by James Mapes and Arieann DeFazio. Work to optimize conditions for SYP/VAMP2 co-immunoprecipitaion was performed by Kerri Ball. Christopher Arthur purified native SYP/VAMP2 complex, performed EM and single particle reconstruction to generate the final refined 3D density map. Michael Stowell generated the high resolution model of the SYP/VAMP2 complex. For illustrations used in Figure 43 and the top panel of Figure 47, we contracted a professional illustrator, Michelle Turco.

CHAPTER 4: INHIBITORS OF AB AGGREGATION

INTRODUCTION

Since introduction of the amyloid hypothesis of AD over 20 years ago[41], an overwhelmingly large literature has accumulated, cementing the central importance of Aß42 in the mechanism of the disease (reviewed [34,50,117–120]). Due to its causal role in AD, Aß peptide is a favored tool to model the disease mechanisms and phenotypes. Synthetically derived Aß has been widely used in animal models and cell culture systems to aid in understanding the biological targets and pathologic mechanisms of AD. Synthetic Aß is also heavily used for *in vitro* characterization of the basic biophysical properties which imbue Aß42 with such unique and toxic potency. While the synthetic peptide has unquestionably proven to faithfully recapitulate many disease-relevant molecular and physiological pathologies, data generated in these models notably suffer from poor reproducibility. Because of its extreme propensity to aggregate in solution, harsh conditions are typically employed in the handling of synthetic Aß to keep it soluble for use in various assays. These include concentrated urea, strong base, guanidine and even organic solvents, however no single method is standard in the field. Seeding further variability, numerous conflicting methods are commonly used in quantifying Aß concentration. Beyond these complications in handling Aß, it is now becoming evident that the source and purity of the peptide can have major impacts on its performance in functional assays. While synthetic Aß is widely available from many manufacturers and has been used ubiquitously for many years, peptide produced recombinantly in

bacteria is now emerging as a compelling alternative. An initial report indicates that synthetic Aß peptide contains impurities that alter its neurotoxicity and ability to aggregate[121]. Here we have validated those findings and extended the line of questioning to determine the identity of the contaminants which appear to inhibit the toxic activities of Aß42. Through both discovery-oriented and candidate-based approaches, we have found that a failed valine-valine coupling at position 39-40 in Aß42 produces a truncated peptide that co-purifies with full-length Aß42 and is a potent inhibitor of its aggregation and neurotoxic functions. We propose that this truncated Aß derivative merits further investigation in bioassays to characterize its potentially therapeutic properties against Alzheimer's disease.

SYNTHETIC Aβ42 EXHIBITS REDUCED TOXICITY AND AGGREGATION DYNAMICS

Motivated by reports of divergent functional properties between recombinant and synthetic Aß42[121], we sought to directly compare their cytotoxic potency. Samples of synthetic and recombinant Aß42 were prepared as a monomer by solubilizing in hexafluoroisopropanol (HFIP) and re-drying to film under inert gas flow. The films were re-solubilized in 10 mM NaOH to prevent aggregation and diluted into culture medium immediately piror to application. The concentration of each peptide sample was determined by BCA assay in a method that has been independently verified by SDS-PAGE, UV-Vis spectroscopy and amino acid analysis. The popular pheochromocytoma-derived cell line PC12 was used in a toxicity assay because it is known to express many neuronal proteins and is easily amenable to high

throughput bioassays. A concentration series of recombinant and synthetic peptide as well as the NaOH vehicle was prepared and applied to cells for 24 hours. At the endpoint, a standard MTT viability assay was performed (Figure 48). We found that recombinant Aß42 was potently toxic to the neuron-like PC12 cells, inducing measurable toxicity as low as 25 nM with an apparent LD_{50} of 190 nM. In contrast, the toxicity of the synthetic peptide was significantly lower, with an apparent LD_{50} of 280 nM.

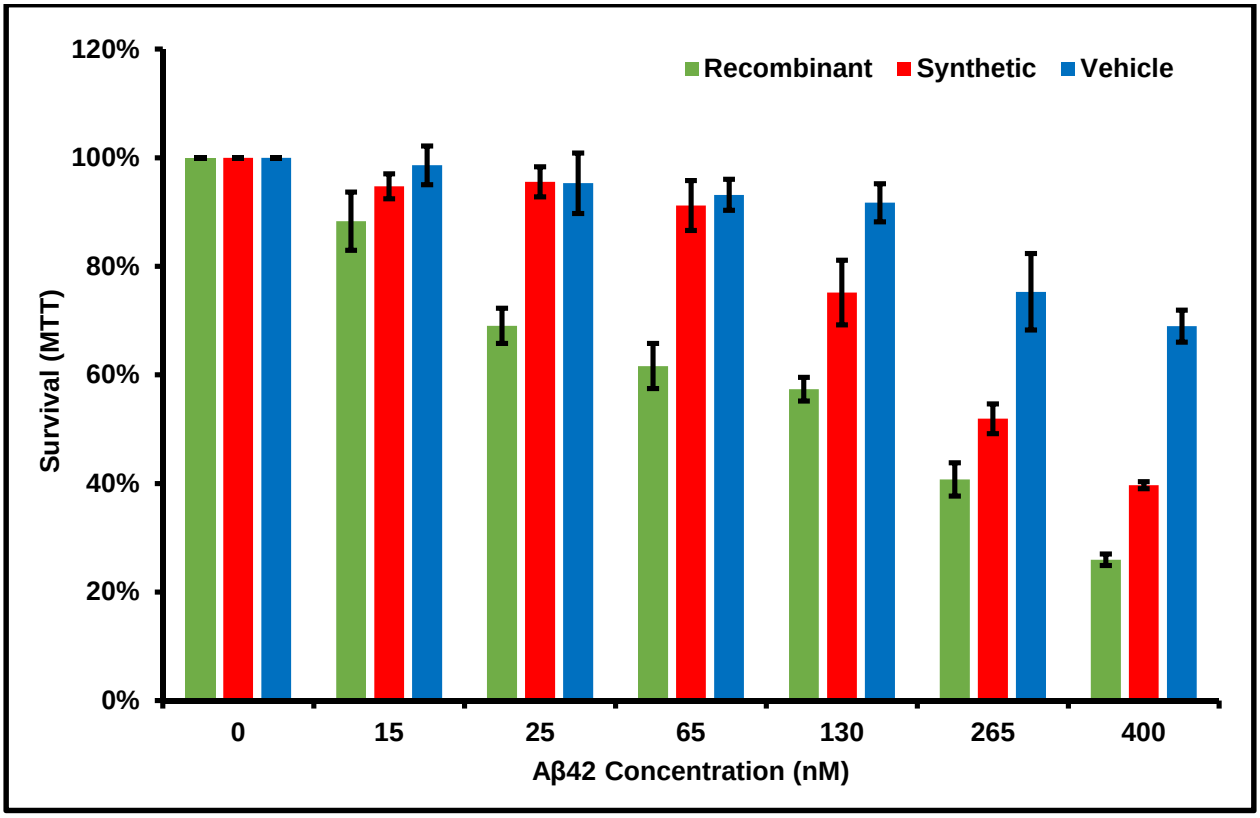

Figure 48: Recombinant Aβ42 is More Cytotoxic
MTT survival after 24h of peptide treatment at indicated concentrations. Averages from two experiments and six replicates. Error bars represent SEM.

The aggregation behavior of Aß42 is well documented and highly investigated, but the relationship between this behavior and the protein's acute cytotoxicity is not entirely clear. Therefore, negative stain electron microscopy was used to determine if there were structural correlates of the reduced toxicity displayed by synthetic Aß42. Recombinant and synthetic Aß42 stocks at 10 µM were diluted to 1 µM in phosphate buffered saline (PBS pH 7.4) to induce aggregation. Samples were removed for imaging after 15 and 60 minutes. Samples were stained with 2% uranyl acetate for 30 seconds and imaged at 80 kV in a Phillips CM100. Within 15 minutes both samples displayed obvious fibrils (Figure 49 and Figure 50) and appear to contain small globular structures which may be proto-filamentous aggregates. However, compared to the synthetic peptide the recombinant Aß42 formed much longer linear fibrils and in much greater quantity, despite the fact that both samples contained identical peptide concentrations. By 60 minutes, significantly more and longer fibrils had formed in both samples compared to the earlier time point (Figure 51 and Figure 52). Again, the recombinant sample displayed a more elongated linear morphology whereas the synthetic preparation was characterized by shorter more branched clumps of fibrils. In the recombinant sample, short protofibrils are present at very high density suggestive that most molecules are in some form of oligomer and few monomers persist at this time point. To determine the morphologic endpoint of the aggregation process, the recombinant sample was allowed to continue aggregation for 72 hours (Figure 53). At the end of this time, a dense mesh of straight linear fibrils had formed.

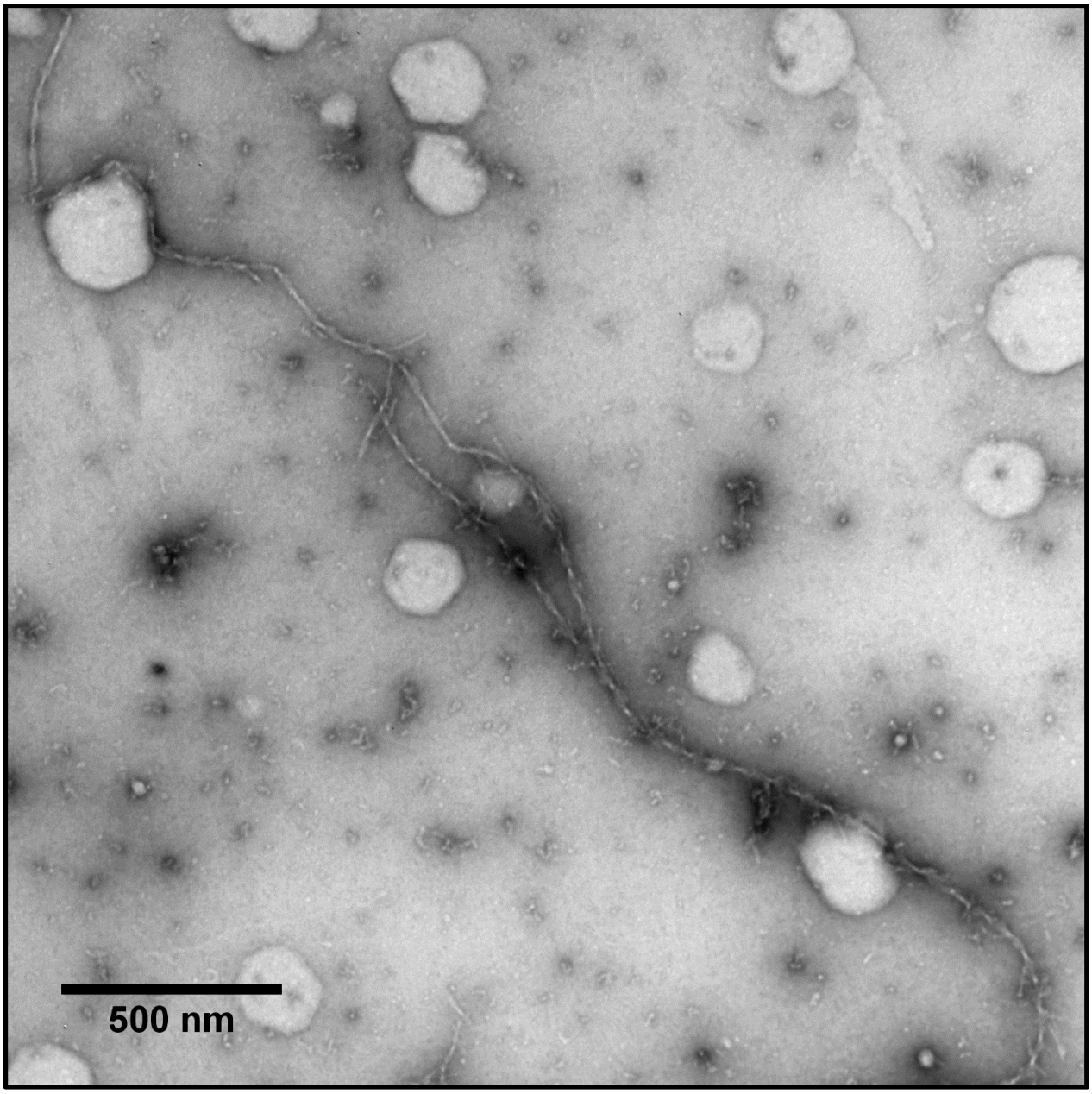

Figure 49: Recombinant Aβ42 Aggregates into Fibrils - 10 min.
Negative-stain TEM of recombinant Aβ42 after 10 minutes of aggregation in PBS pH 7.4.

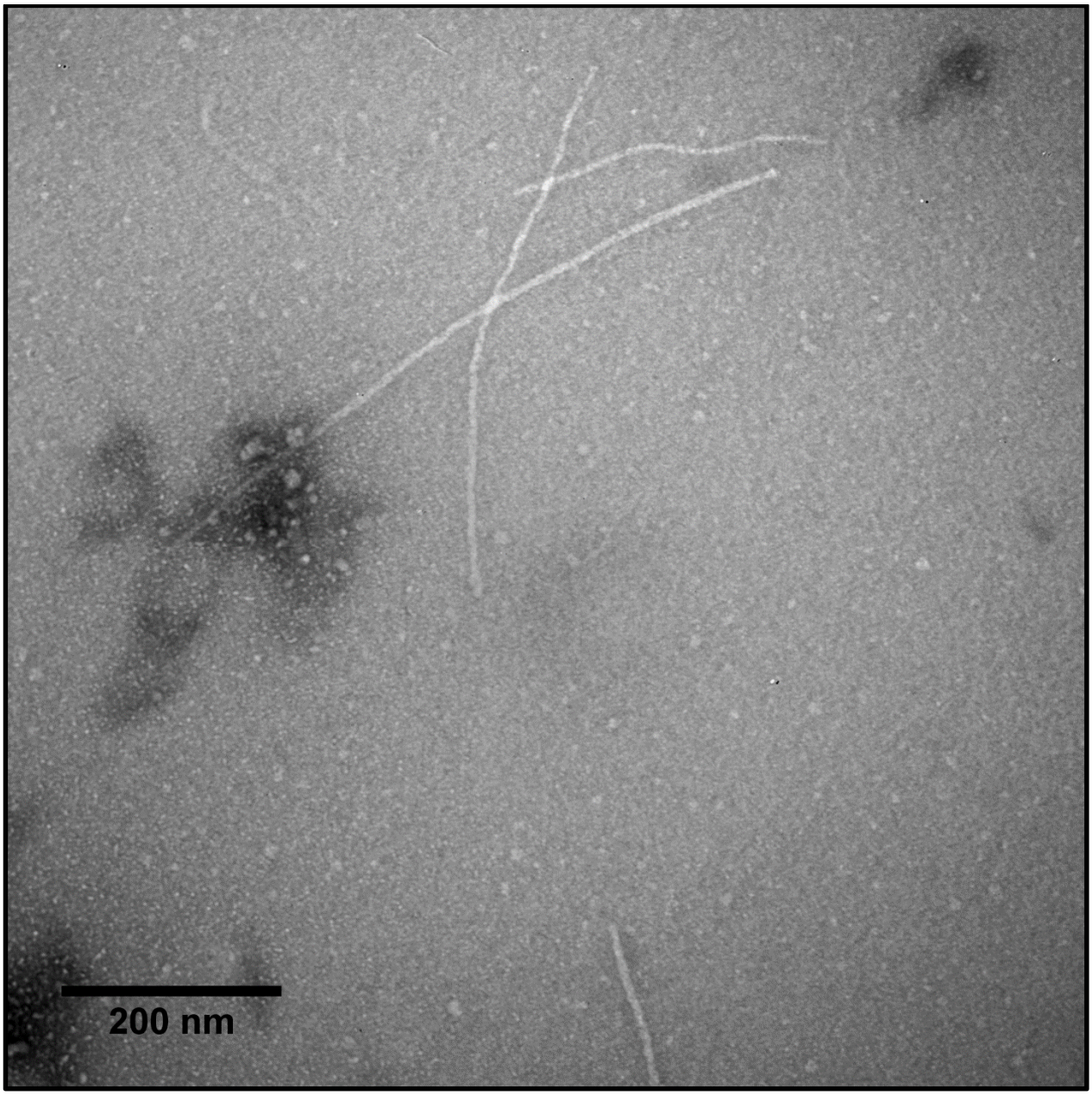

Figure 50: Synthetic Aβ42 Aggregates into Fibrils - 10 min.
Negative-stain TEM of synthetic Aβ42 after 10 minutes of aggregation in PBS pH 7.4.

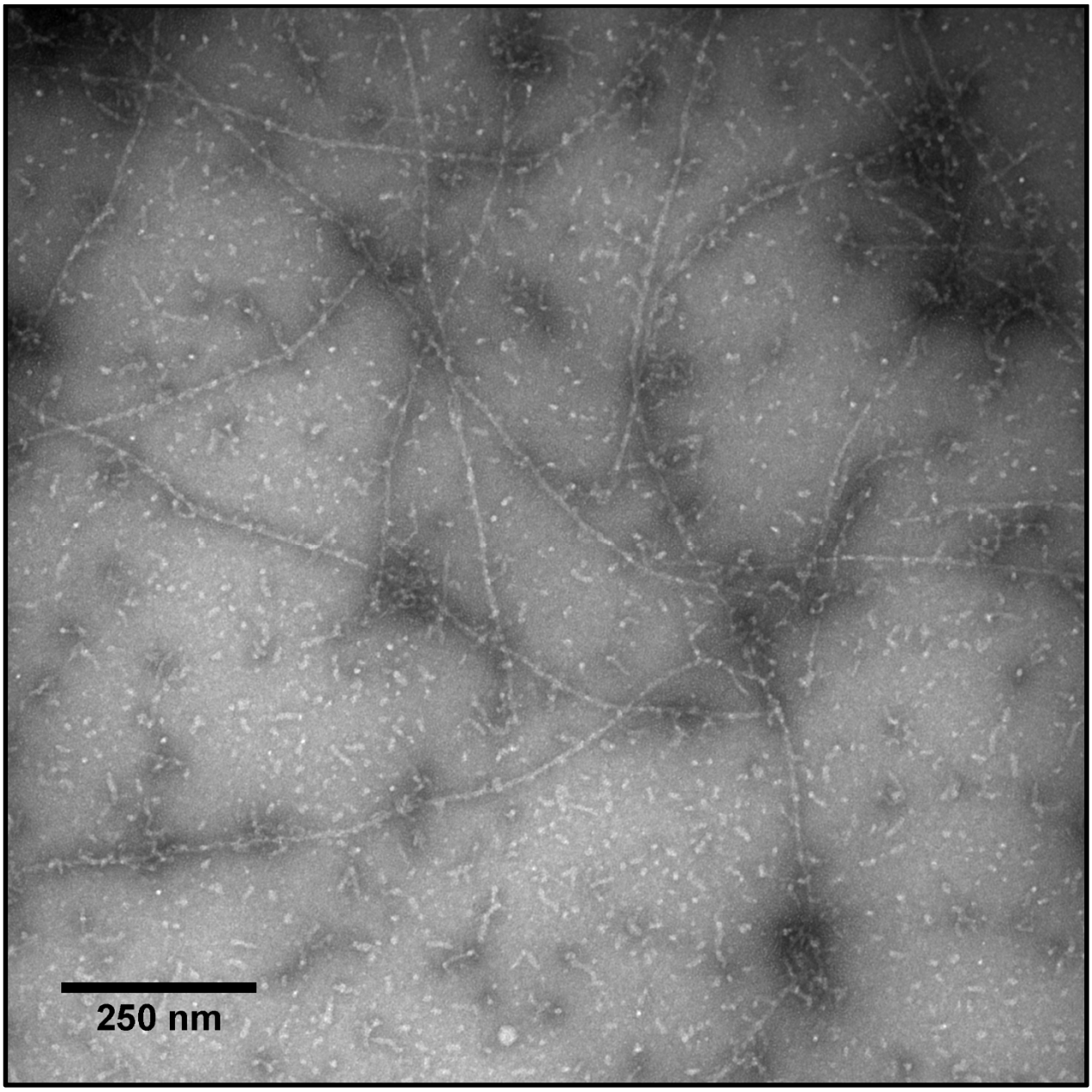

Figure 51: Recombinant Aβ42 Aggregates into Fibrils - 60 min.
Negative-stain TEM of recombinant Aβ42 after 60 minutes of aggregation in PBS pH 7.4.

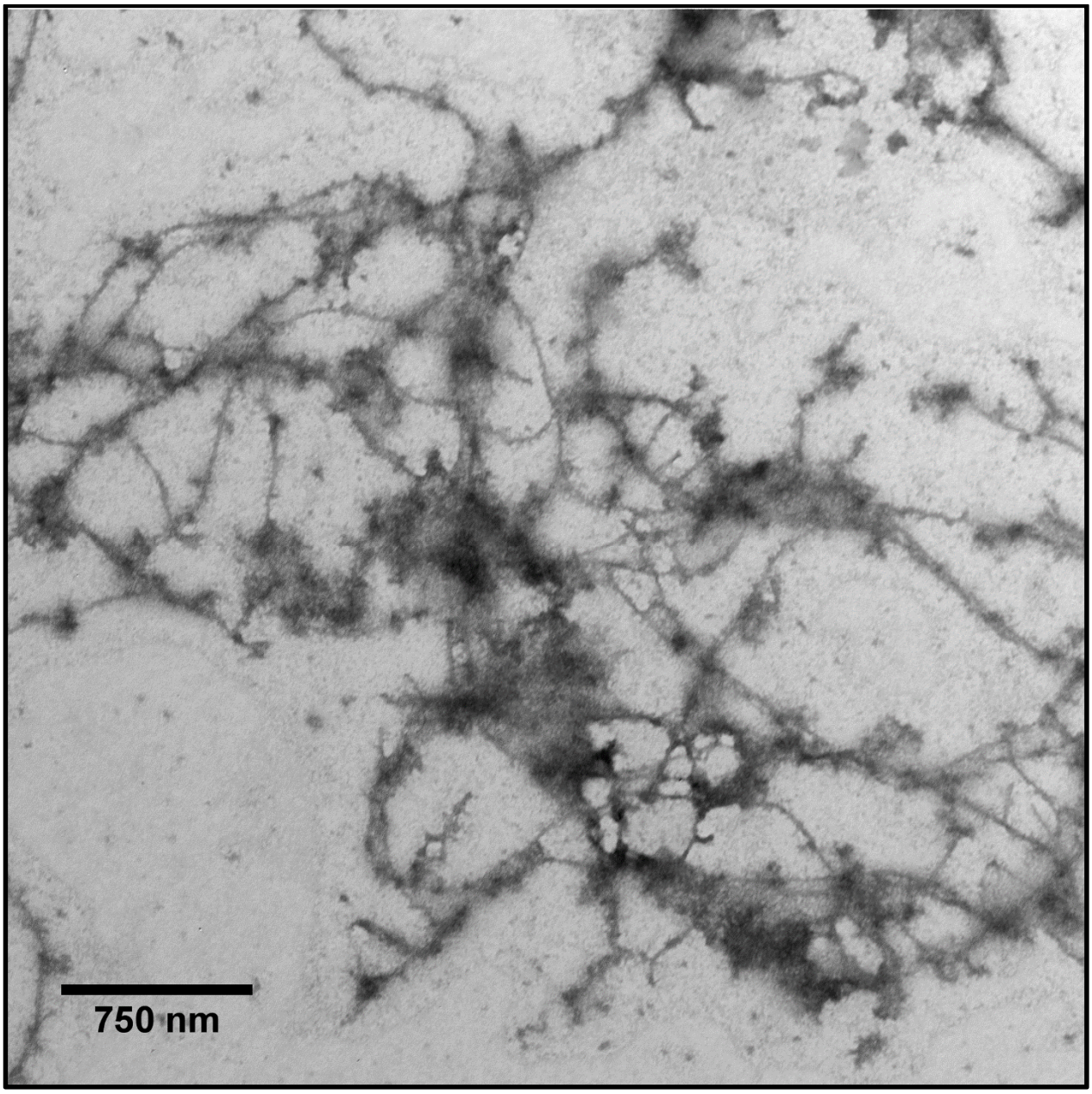

Figure 52: Synthetic Aβ42 Aggregates into Fibrils - 60 min.
Negative-stain TEM of synthetic Aβ42 after 60 minutes of aggregation in PBS pH 7.4.

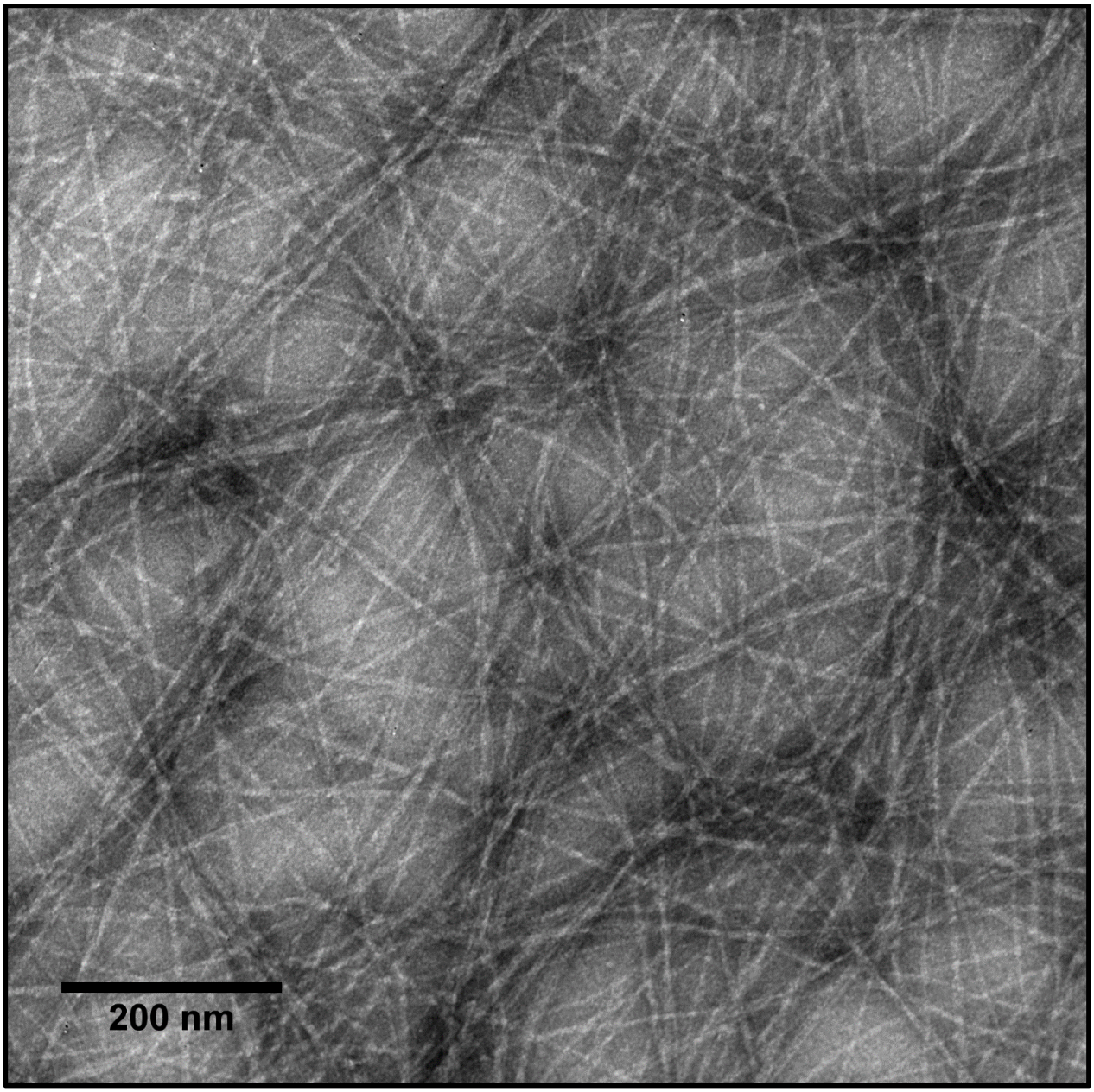

Figure 53: Recombinant Aβ42 Aggregates into Fibrils - 72 hrs.
Negative-stain TEM of recombinant Aβ42 after 3 days of aggregation in PBS pH 7.4.

After observing qualitative differences in the morphology of aggregating fibrils of recombinant and synthetic Aß42, we sought to determine if differences might also exist in the quantitative dynamics of fibrillation. To this end we

performed a standard fluorescence-based assay to track the kinetics of aggregation in real-time. Thioflavin T (ThT) is a benzothiazole dye that binds specifically to fibrillar Aß and has been used for many years as a marker in histological identification of Aß plaques in brain tissue. ThT binds an interaction surface unique to Aß fibrils whereupon its fluorescence emission is greatly enhanced[122]. Thus an increase in ThT signal represents increased binding to fibrils and is therefore a direct readout for aggregation. Using ThT dye, we observed both a longer lag time as well as reduced slope of the fast phase in the synthetic peptide sample.

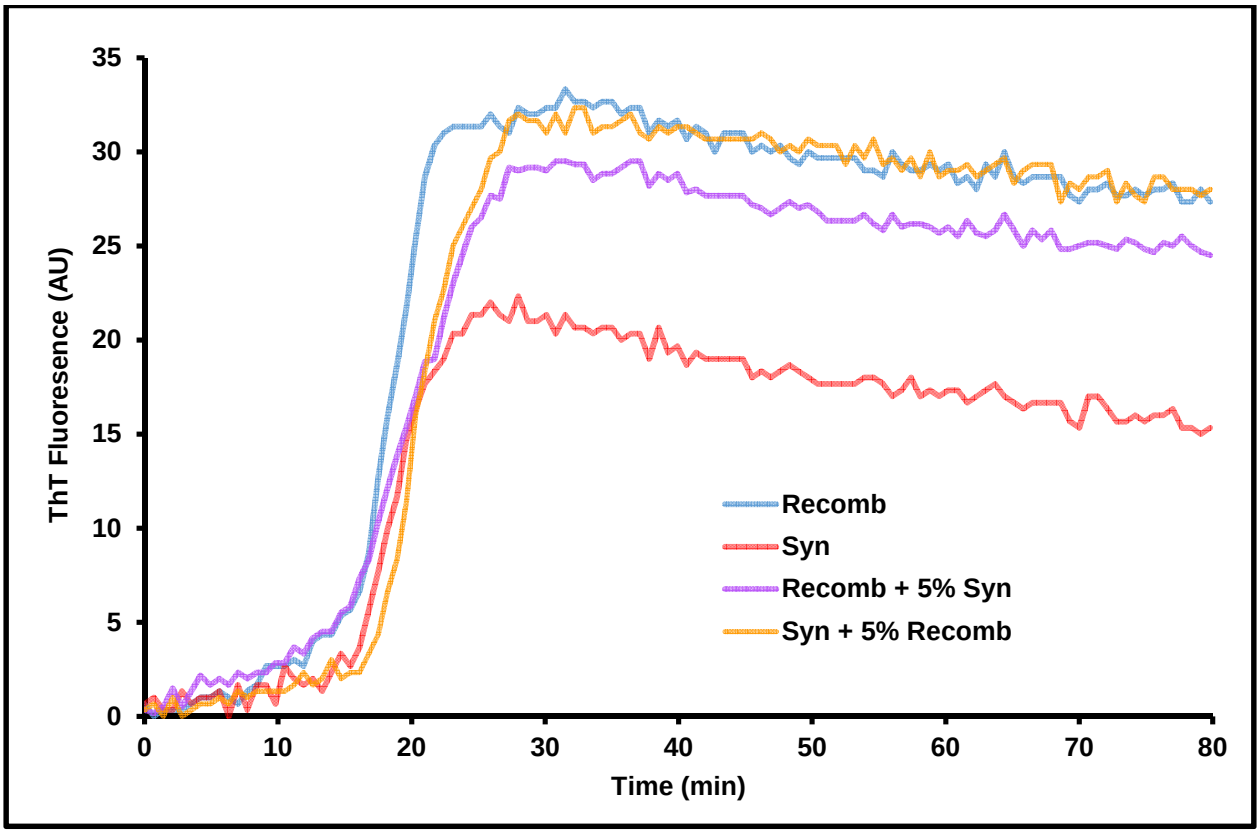

Figure 54: Aggregation of Recombinant, Synthetic and Mixed Aβ42
ThT fluorescence trace of Aβ42 aggregation. Mixing experiment is 5% synthetic Aβ42 in recombinant peptide (n/n%).

We have observed that the ability of Aß42 to aggregate correlates with its toxicity. This correlation has been noted before[121,123,124], but it is not clear by what mechanism the tendency toward fibrillation would drive toxicity. To further explore this connection, we assayed if manipulations which impact aggregation behavior could also alter toxicity. For this experiment we utilized the G37L mutant of the Aß42 peptide. This mutation disrupts the glycine zipper motif (Figure 55) that is important for the normal homo-oligomerization of Aß42[123,125]. It has been observed that the G37L mutant peptide can act as a dominant negative in an aggregation assay[123,124,126]. Thus, we performed a 1:1 mixing experiment between wild-type and G37L Aß42 and applied this peptide to PC12 cells in the same toxicity experiment as above (Figure 48). We found that the G37L peptide exhibited a protective effect from Aß42 toxicity (Figure 56). This result supports the claim that features of Aß42 involved in oligomerization are also important in toxicity.

Figure 55: Sequence and Features of Human Aβ42
Sequence of human Aβ42 peptide. Histidine residues highlighted in yellow. Glycine 37 highlighted in blue. Valine 39 highlighted in red. Purple bar indicates sequence derived from the transmembrane domain of APP. Blue curved lines indicated glycine zipper motif.

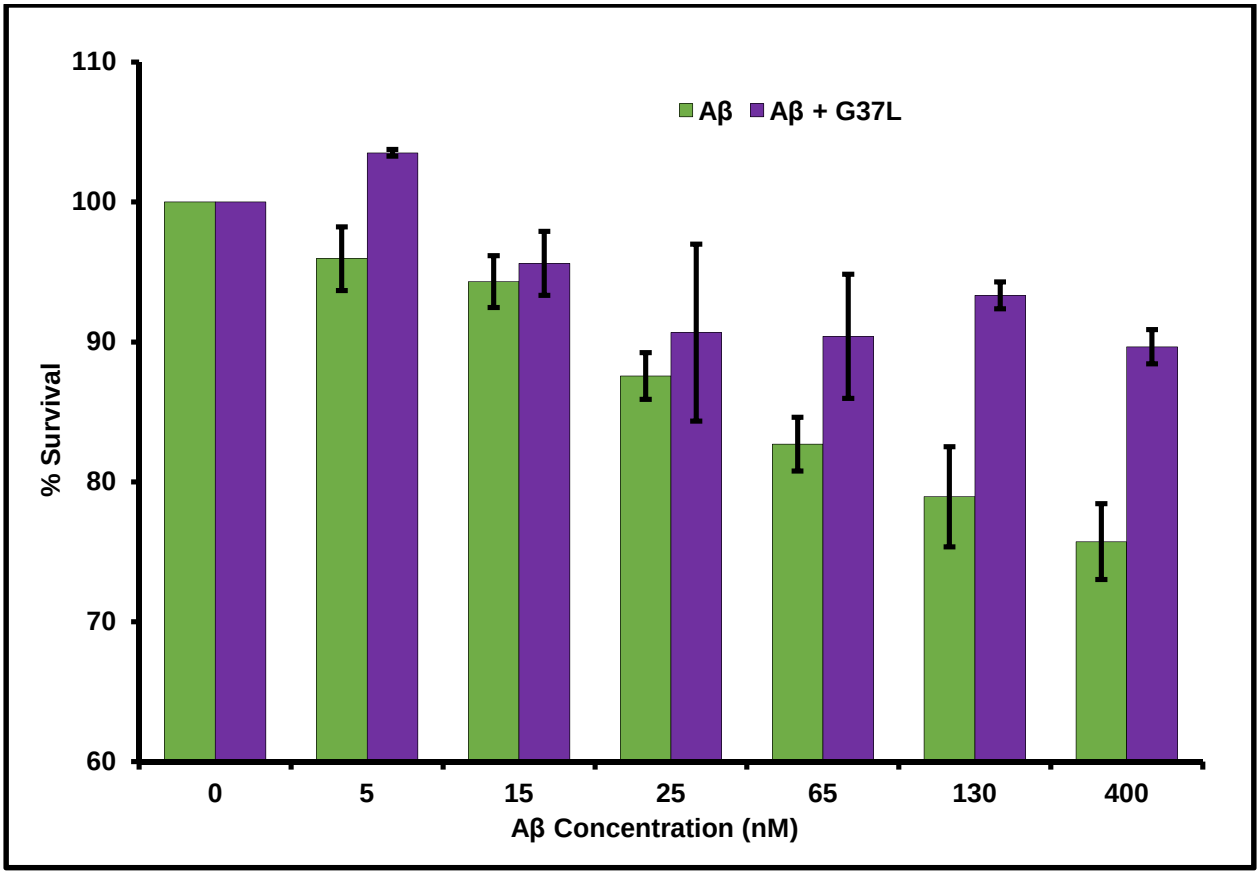

Figure 56: Aβ42 G37L Protects from Toxicity as Dominant Negative
Wild-type recombinant Aβ42 was mixed in an equimolar ratio with Aβ42 G37L. PC12 cells were treated for 24 hours and viability was assayed by MTT. Bars represent 6 replicates. Error bars represent SEM.

From multiple manufacturers, a typical lot of commercial Aß42 peptide is stated as >95% pure. Assuming these numbers are accurate, two distinct scenarios could explain the disparity in aggregation dynamics and toxicity between recombinant and synthetic Aß42. One possibility is that some contaminant in the recombinant peptide is responsible for its comparatively enhanced toxicity and aggregation behavior. If it were possible to identify this contaminant and add it to the synthetic

Aß42, increased performance of the synthetic peptide would be expected. The other possibility is that a minority product present in the synthetic peptide is inhibiting its natural aggregation and toxicity. To distinguish between these possibilities, a doping experiment was performed in which a small amount (5% mole fraction) of synthetic peptide was added to the recombinant peptide and subjected to aggregation analysis by ThT fluorescence. If a contaminant of the recombinant peptide were responsible for its enhanced aggregation behavior compared to the synthetic peptide, then no change in dynamics would be expected; but if an inhibitor of aggregation were present in the synthetic peptide, it should still be able to produce a measurable effect even diluted 20 fold. Strikingly, we observed that only 5% of the synthetic peptide was sufficient to perturb the normal dynamics of Aß42 aggregation (Figure 54). Both the time to $t_{\frac{1}{2}}$ and slope of rapid aggregation phase indicate that the dynamics of aggregation have indeed been altered by the minority species present in the synthetic peptide. In contrast, 5% doping of recombinant Aß42 into the synthetic peptide was not able to improve aggregation behavior (Figure 54).

We next used this doping strategy to assess toxicity of Aß42 mixtures in PC12 cells. In agreement with our ThT data, just a small dose of synthetic peptide was capable of reducing the toxicity of the recombinant peptide by a measurable amount (Figure 57), further confirming the potency of the inhibitory species present in the synthetic Aß42 preparation.

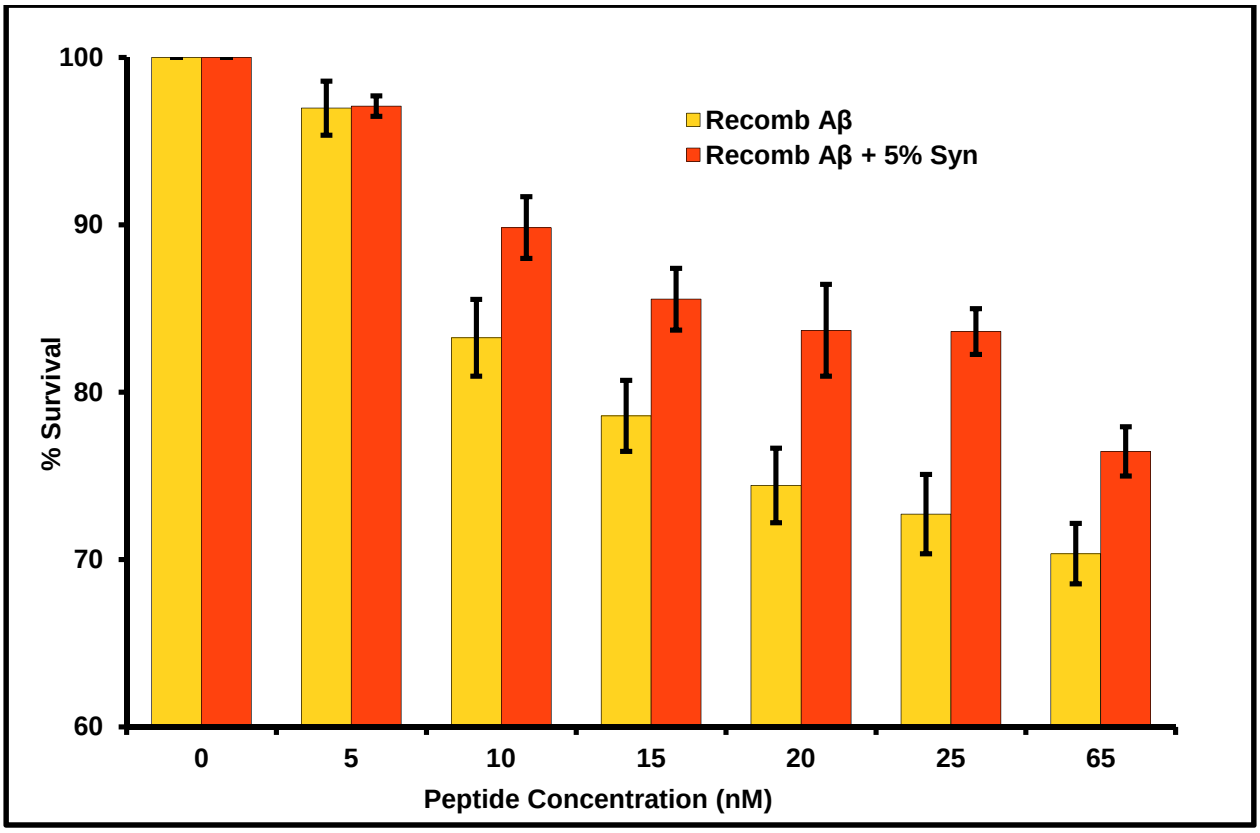

Figure 57: Synthetic Aβ42 Contains a Potent Inhibitor of Toxicity
MTT toxicity assay of PC12 cells treated with recombinant Aβ42 ± 5% synthetic Aβ42 (n/n%). Assay performed in triplicate, error bars represent SEM.

IDENTIFICATION OF Aβ INHIBITORS

Our data indicate that a potent inhibitor of both the aggregation (Figure 54) and toxicity (Figure 57) of Aß42 exists as a minority product present in the commercially obtained synthetic peptide. This finding has wide implications due to the ubiquitous use of synthetic Aß42 in AD research. However, due to the recent commercial availability of recombinant Aß42$^{127–129}$, it may not be necessary to improve upon commercial synthesis and purification to avoid these inhibitory contaminants. Instead, these unknown inhibitors may prove valuable as a starting point for the

rational design of molecules for therapeutic intervention in AD. Furthermore, these inhibitors serve as a unique and novel tool for probing the relationship between Aß42 aggregation and toxicity.

We began our study of the contaminants of synthetic Aß42 by optimizing a chromatographic method for both purification and analysis. We found conditions under which we could elute sharp peaks of recombinant Aß42 off a C8 reverse-phase column in a mobile phase of acetonitrile with TFA as a counter ion. We then used this method to analyze the synthetic Aß42 sample for the presence of contaminants. The same sharp main peak existed, however a number of additional minor peaks were observed. The was a distinct peak that eluted just before the main peak, as well a significant shoulder on both the leading and trailing edges of the main peak.

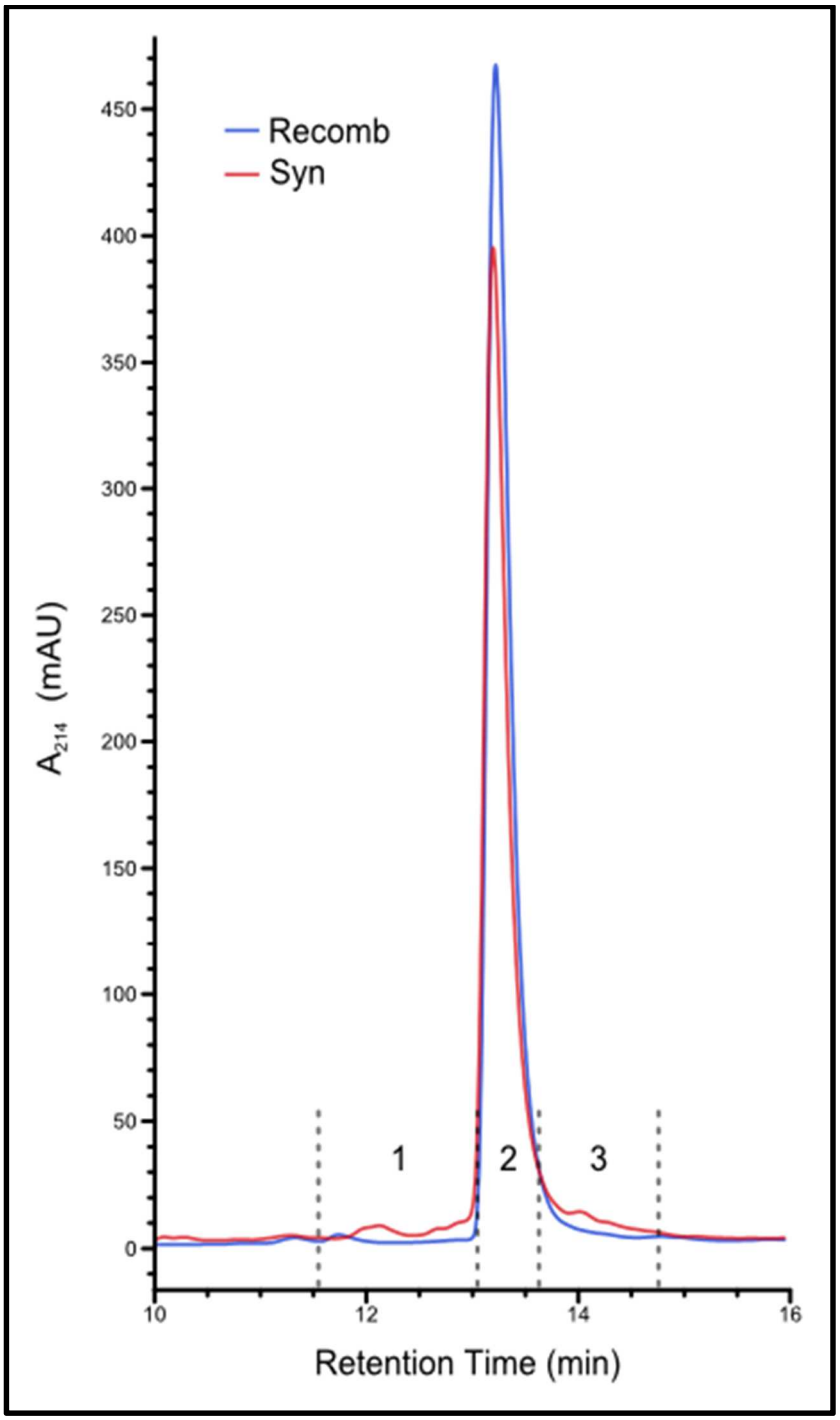

Figure 58: HPLC Analysis of Recombinant and Synthetic Aβ42
RP-HPLC of recombinant and synthetic Aβ42 reveals contaminants in synthetic preparation. 10 µg of each peptide sample was loaded. Fractions collected from synthetic sample indicated 1, 2 and 3 by dashed lines.

We also analyzed both recombinant and synthetic peptide samples by MALDI-TOF mass spectrometry (Figure 59). This analysis revealed that the synthetic peptide sample contains a diverse collection of contaminants; however due to their relatively low abundance no specific identifications from this MALDI-TOF cocktail were possible.

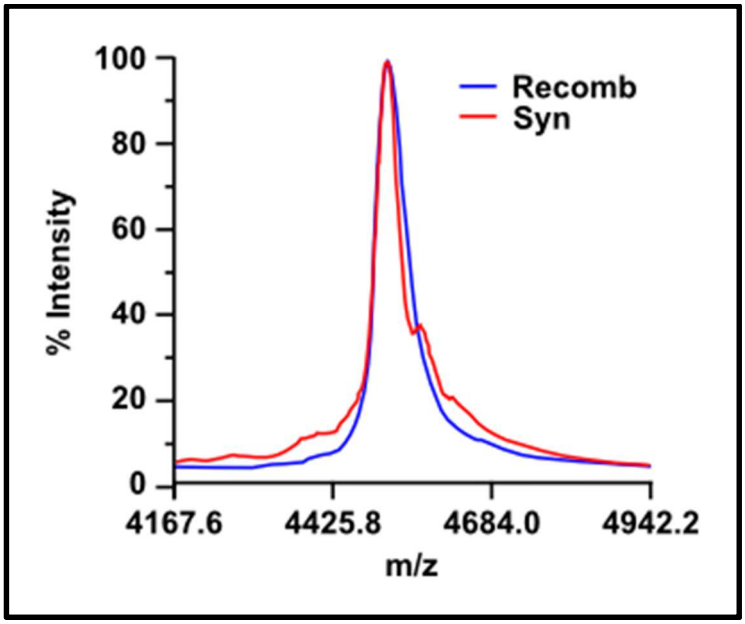

Figure 59: MALDI Mass Spectra of Aβ42 Samples
MALDI-TOF spectra reveal contaminants in synthetic Aβ42 sample.

It has been reported that synthetic Aß42 contains a significant fraction (> 1%) of D-histidine that is suggested to be the functionally relevant contaminant in the synthetic material[121]. The traditional reverse-phase chromatographic methods used to purify Aß42 would be incapable of resolving peptides epimerized at any of the three histidine residues in Aß42 (Figure 55). Racemized peptide would also be indistinguishable by mass spectrometry, making it very difficult to assay for this

contaminant with commonly used tools. To directly test if an Aß42 histidine racemate was capable of recapitulating the aggregation inhibition imparted by the synthetic peptide, we obtained a sample of racemized peptide for ThT assay. The peptide was synthesized using a standard solid phase Fmoc-protected method, but at positions 6, 13 and 14 a 50:50 mixture of L- and D-histidine enantiomers was applied. Thus, a mixture of Aß42 molecules representing every possible combination of histidine stereochemistry was yielded (noted below as Aß42-HIS). The Aß42-HIS was doped into recombinant Aß42 at 5% mole fraction, a much higher concentration than might normally appear in the synthetic peptide, and aggregation was monitored by ThT fluorescence. We found that even this large dose of Aß42-HIS only induced a modest reduction in the recombinant peptide's velocity of aggregation. Therefore we conclude that though Aß42-HIS may be capable of inhibiting Aß42 aggregation, it alone is not sufficient to illicit effects of the magnitude observed. Therefore, we believe that other as yet undiscovered inhibitors in synthetic Aß42 must exist.

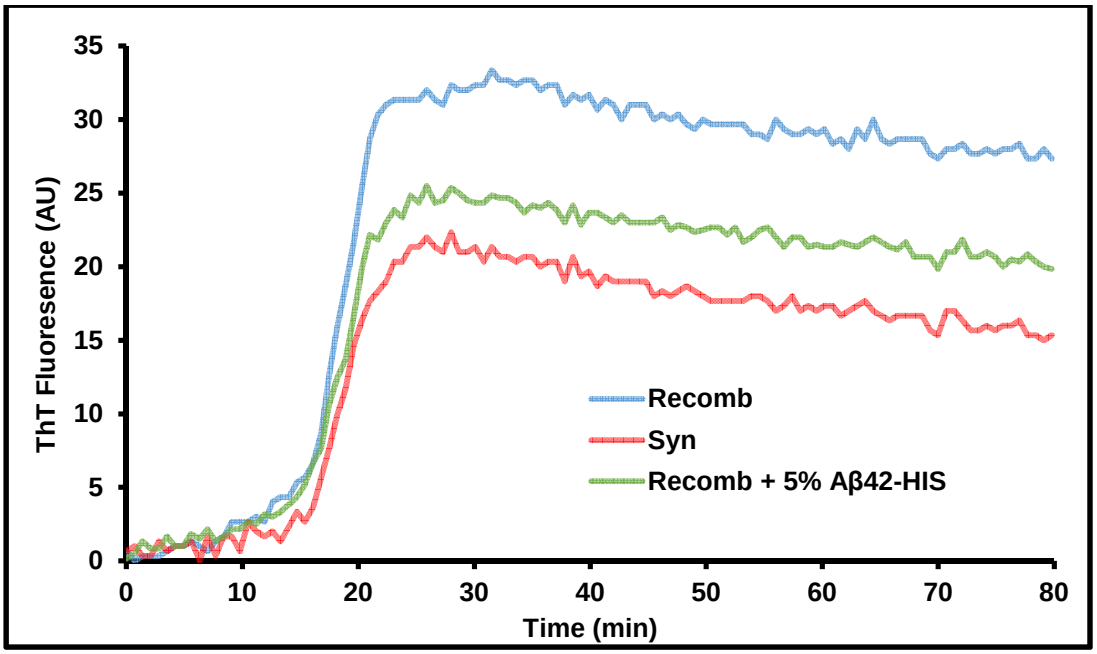

Figure 60: Aβ42 Histidine Racemate Inhibits Aggregation
ThT fluorescence was used to assay aggregation dynamics of Aβ42-HIS mixed into recombinant Aβ42.

Using RP-HPLC (Figure 58) and mass spectrometry (Figure 59), we observed many contaminating minority product in synthetic Aß42. To determine if any of these possessed inhibitory activity, synthetic Aß42 samples were fractionated by RP-HPLC and then assayed for inhibition of aggregation using ThT. Specifically, the main peak of synthetic Aß42 was isolated from the contaminating material that eluted on either side of it, yielding fractions labeled 1, 2 and 3 (Figure 58). As before, fractions were doped into recombinant Aß42 at 5% for the aggregation assay. Significant changes in aggregation dynamics were not observed in recombinant peptide doped with fractions 2 and 3, but we found that fraction 1 contained extremely potent inhibitory activity. We suspect that this fraction was still a

complex mixture; therefore it remains unclear whether its inhibitory activity is caused by a single or multiple species. Without further analysis by more sensitive methods such as tandem MS-MS, it is impossible to ascertain the identity of the active agents isolated in fraction 1. The quantity of relevant contaminants available for study is extremely limiting prompting us to adopt a candidate-based approach towards identification of Aß42 inhibitors.

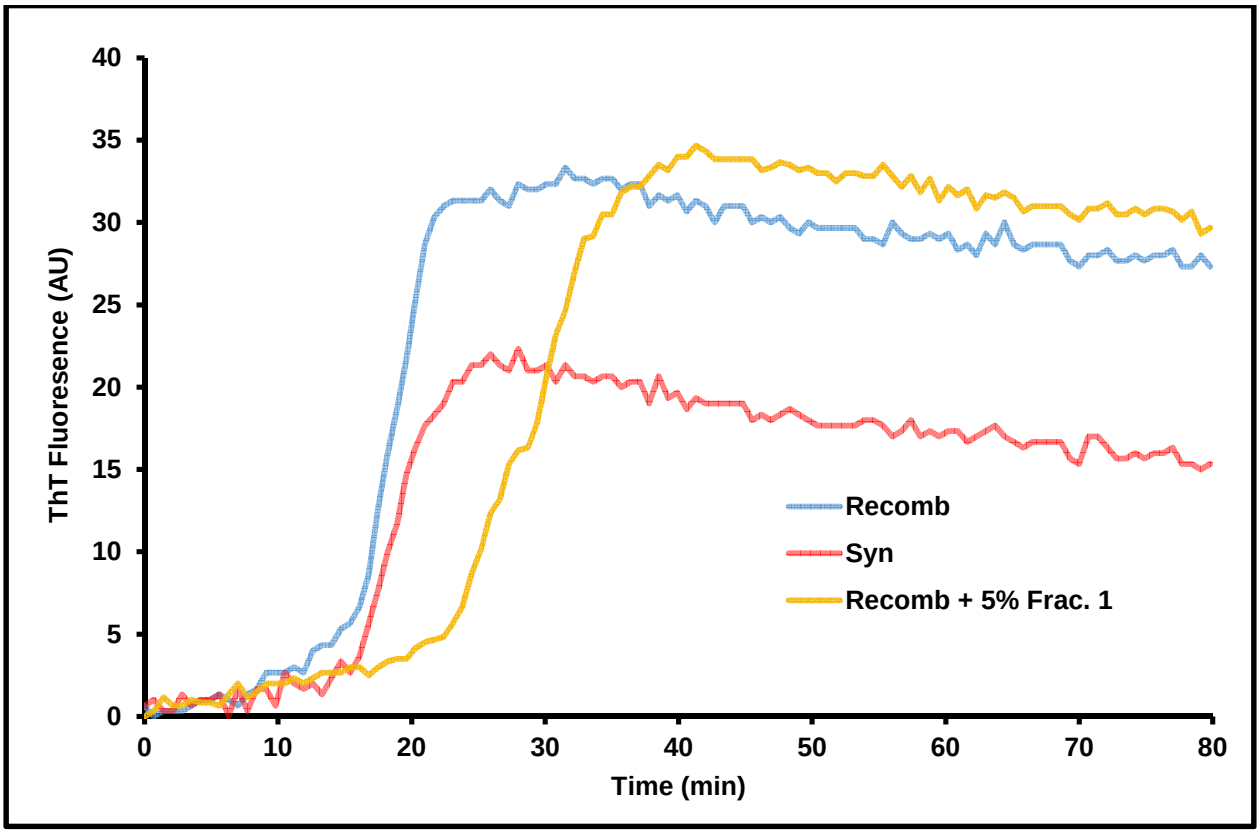

Figure 61: Contaminant is Potent Inhibitor of Aggregation
HPLC fraction 1 was doped into recombinant Aß42 and aggregation was assessed by ThT fluorescence.

There are several sequence features which are known to pose challenges to standard solid phase peptide synthesis methods, and therefore can inform rational

prediction of peptide synthesis byproducts for a given target. Highly hydrophobic aggregation-prone sequences such as found in Aß42 are known to be particularly difficult to generate[130]. Traditional synthesis methods proceed from the carboxy-terminus towards the amino-terminus coupling a single amino acid at a time each followed by a round of deprotection and wash. Given that the carboxy-terminal 1/3 of Aß42 is derived from the transmembrane helix of APP (Figure 55), early steps in the synthesis of Aß42 are particularly susceptible to aggregation of the nascent peptide chain[131]. Peptide aggregation competes with binding of synthesis reagents including deprotection agents and subsequent amino acid residues[132]. Because of the iterative nature of the synthesis process, if either deprotection or coupling fails for a particular molecule in one round, that molecule may well participate in future rounds of synthesis, yielding a final peptide lacking only a single amino acid. In addition to these challenges, couplings between C-beta branched residues (val, ile, thr), which are used in Aß42 synthesis, are known to be of lower efficiency than other peptide couplings in general[133] which led us to predict that omission of valine 39 (hereinafter Aß42Δ39) generated a putative byproduct of synthesis (Figure 55).

Absolute mass resolution by MALDI-TOF is inversely correlated with analyte mass[134], and therefore the 3% difference in mass of Aß42Δ39 from the total peptide would prove difficult to resolve using solely this method. Digestion of the sample with trypsin would generate a C-terminal fragment 29-42. Aß 29-42 has an expected mass of approximately 1270 Da which would shift to 1171 Da upon deletion of Val 39, a change of nearly 10% which would be more readily resolved. Therefore this

combinatorial method of enzymatic digestion and subsequent MALDI-TOF analysis was performed in order to reveal putative Aβ42Δ39 contaminants. Digestion was carried out on synthetic Aβ42 overnight at 37 °C. The resultant peptides were desalted/concentrated with a C_4 reversed-phase ZipTip and eluted in acetonitrile and analyzed by MALDI-TOF.

Fragment	1-5	6-16	17-28	29-42
Expected Mass (Da)	637.29	1337.60	1325.67	1269.76
Observed Mass (Da)	638.21	1337.23	1324.79	1271.55

Table 2: Trypsin Digest of Aβ42

After optimization of desalting conditions and matrix/spotting parameters we were able to identify all four trypsin digestion peaks (Table 2: Trypsin Digest of Aβ42 and Figure 62). We found no peaks corresponding to partial digestion indicating that the reaction had gone to completion. Disappointingly, the 29-42 peptide of interest was found to ionize very poorly by MALDI, leading to very weak signal. We did not see evidence of a peak near 1153 although we considered this uninformative as the Aβ42Δ39 would represent only a very small fraction of the already weak signal from the 29-42 fragment. It was, however, encouraging to validate that the original premise of the experiment was well founded.

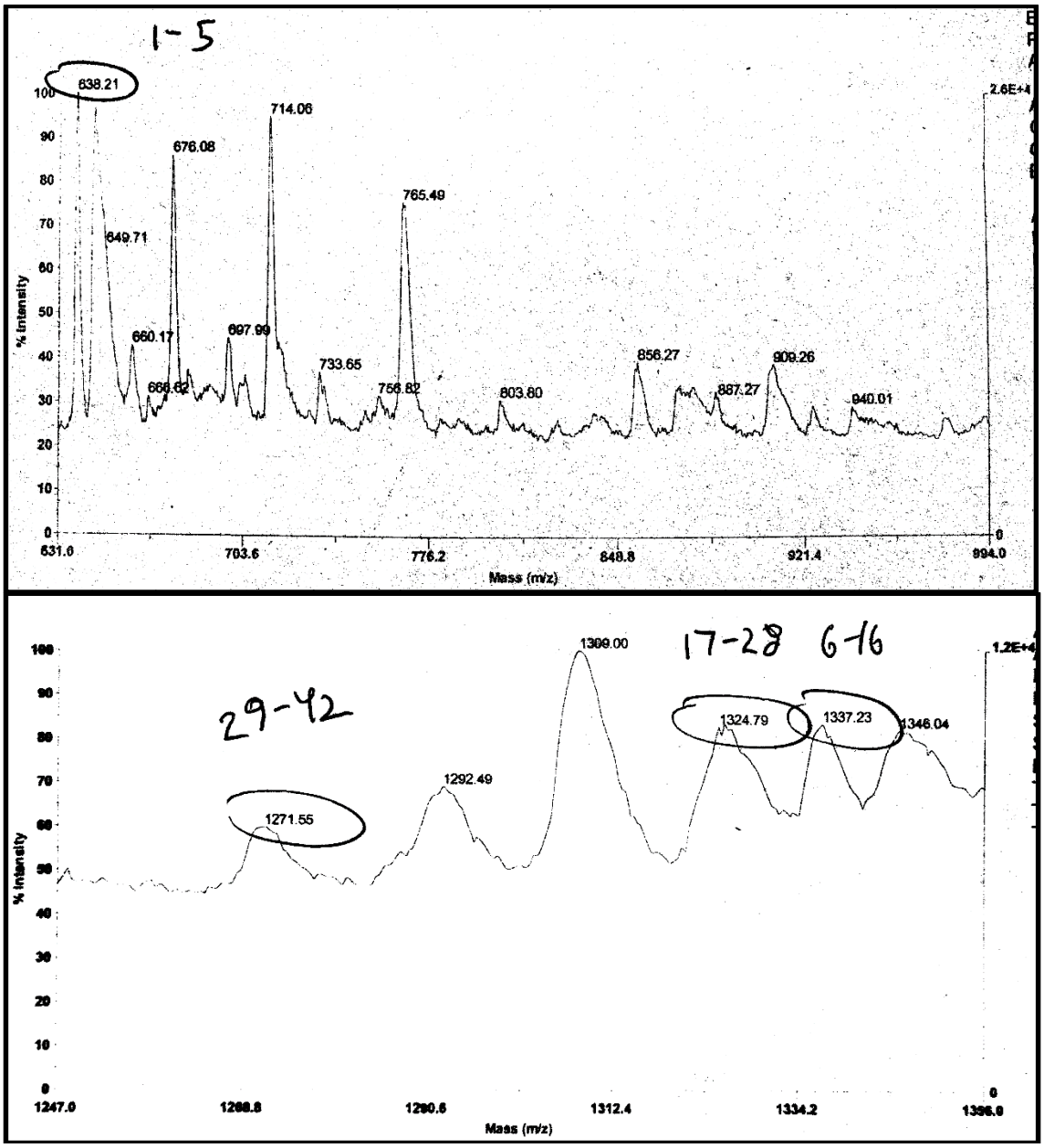

Figure 62: Mass Spectrum of Trypsin Digested Aβ42 Fragments

To overcome the sensitivity hurdles of MALDI-TOF in contaminant identification, we performed ESI-Orbitrap mass spectrometry on both recombinant and synthetic Aβ42.

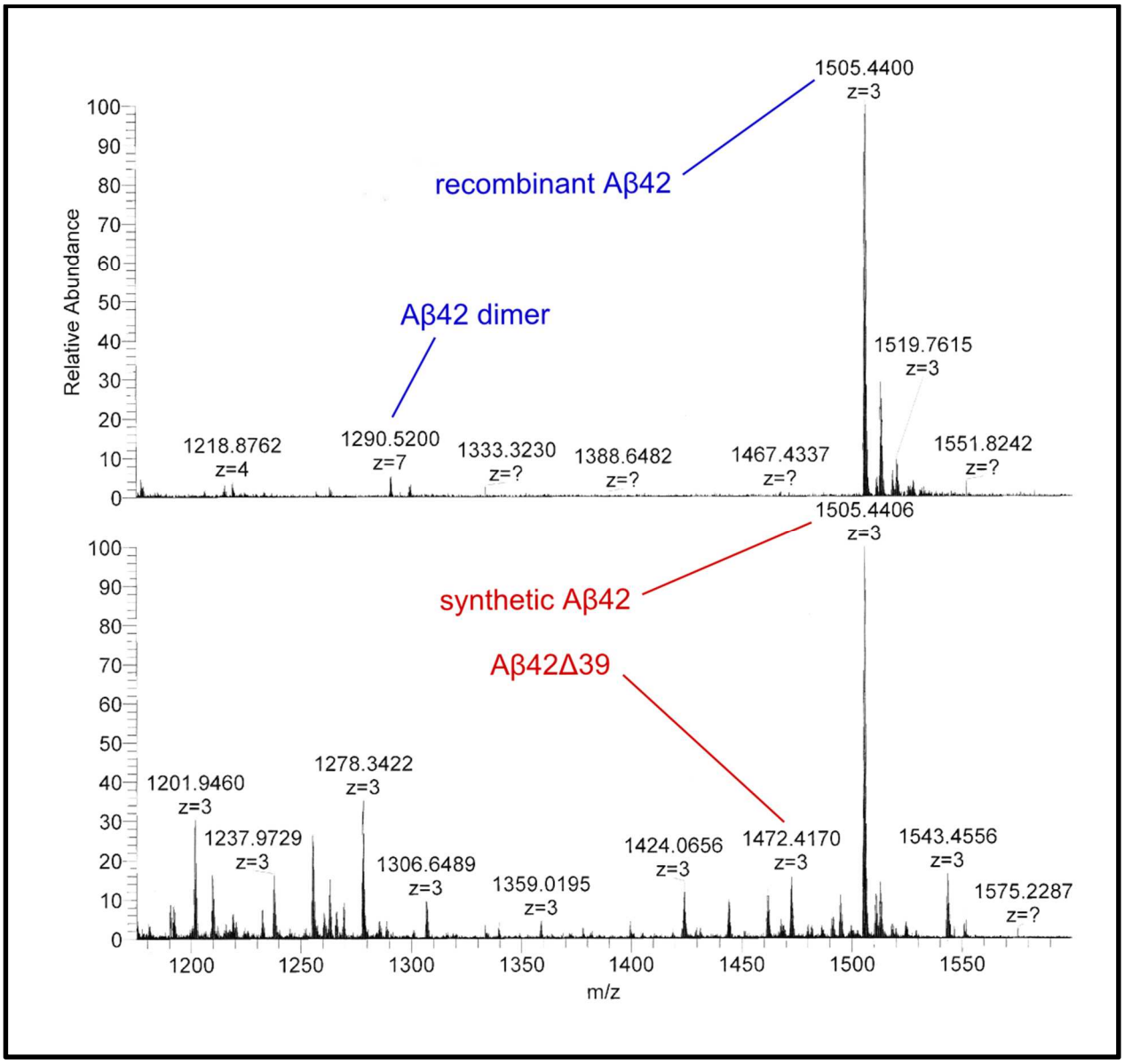

Figure 63: ESI-Orbitrap MS of Synthetic and Recombinant Aβ42

The orbitrap data (Figure 63) strongly confirm the presence of the many contaminating species in synthetic Aß42 observed by MALDI MS (Figure 59) and HPLC (Figure 58). The orbitrap allowed us to resolve individual peaks out of the shoulder present on the Aß42 peak seen by MALDI MS from approximately 4200 Da

to 4500 Da. Importantly, a peak of 4417.25 Da was observed, consistent with the presence of Aß42Δ39. Based on this finding, we proceeded with direct evaluation of Aß42Δ39 as an inhibitor of Aß42 aggregation.

To directly test if Aß42Δ39 was capable of inhibiting Aß42 aggregation kinetics, we obtained the modified peptide, mixed it into recombinant Aß42 at 5% mole fraction, and assayed aggregation by ThT fluorescence. We observed a remarkable inhibition with a near two-fold increase of $t_{\frac{1}{2}}$ from 17.9 minutes (Aß42) to 30.5 minutes (Aß42Δ39) (Figure 64). This shift was reminiscent of the effect imparted by the HPLC fraction 1 (Figure 61) further suggestive that Aß42Δ39 is the major active component of that fraction.

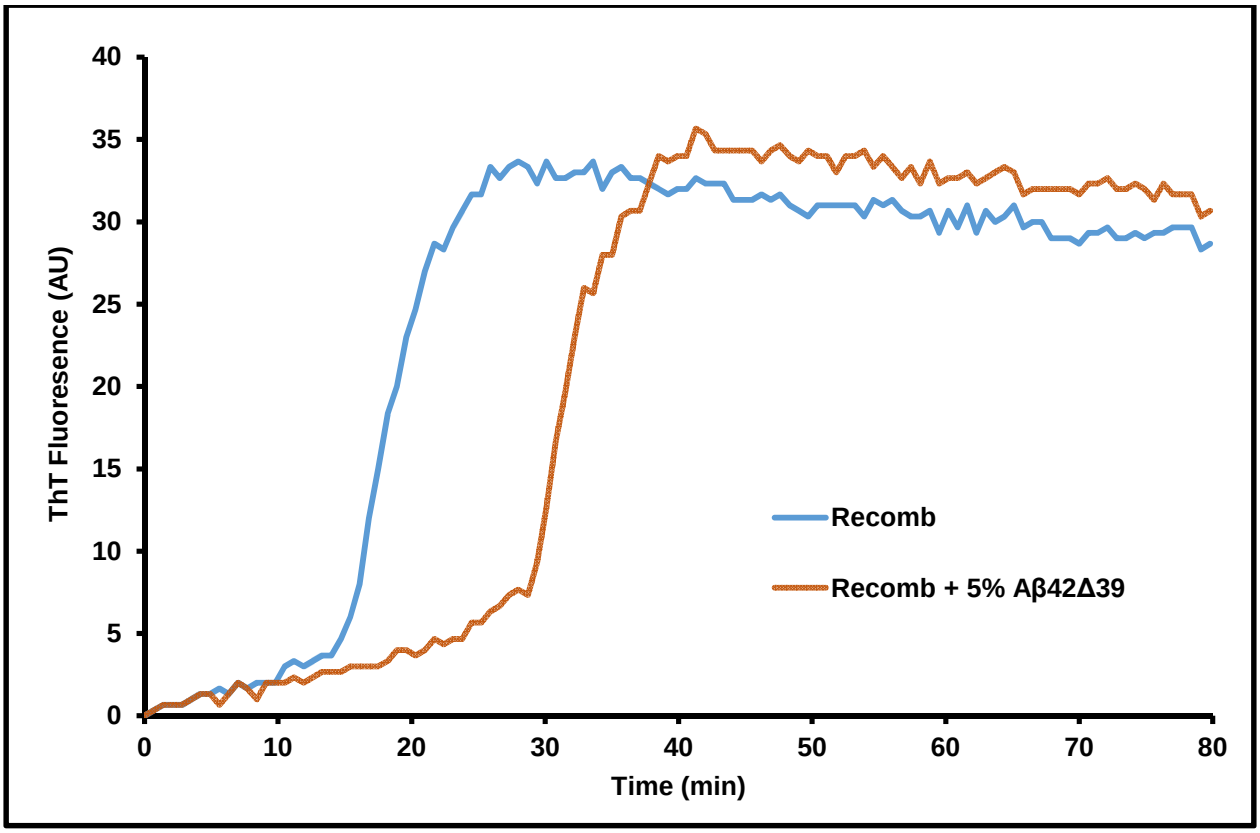

Figure 64: Aβ42Δ39 Potently Inhibits Aβ42 Aggregation
ThT fluorescence was used to assay aggregation dynamics of Aβ42Δ39 mixed into recombinant Aβ42.

DISCUSSION

We observed that Aß42 can disruption the normal fusion of synaptic vesicles (Figure 28), however others using 10 fold more peptide in the same assay have observed an effect of similar magnitude indicating that this activity is not dose responsive. In contrast, we observed here that the toxicity of Aß42 is highly dose responsive and the specific toxicity is sensitive to various factors such as peptide preparation and purity. We found that a recombinant preparation of Aß42 exhibited roughly 1.5 fold higher toxicity when compared to synthetic peptide. This suggests

that the acute toxicity of Aß42 may be occurring by a mechanism separate from the synaptic dysregulation. Hypotheses regarding the specifics of this mechanism are widely varied from activity as a pore forming toxin[135] to generation of oxygen radicals[136]. Because Aß42 peptide is generically toxic at supraphysiological levels even in non-neuronal cell types[137], it is likely that many mechanisms related to acute toxicity are not disease-relevant at all. The present study was not designed to uncover the mechanisms of Aß42 neurotoxicity in AD, but rather to use acute cytotoxicity as a metric of potency to compare different preparations of the peptide.

Our morphologic analysis of Aß42 aggregates indicates that both synthetic and recombinant peptides form fibrils rapidly and we found that the fibrils were rather homogenous in ultrastructure. Fibrils found at all stages of aggregation were 8-12 nm in thickness even despite other differences. There appeared to be differences in the kinetics of the aggregation as larger and more dense aggregates appeared in the recombinant sample at the early time point, but we also observed morphologic differences in the overall shape of the fibrils. The curvature and branching of the synthetic peptide sample indicates that there may be some slight variation in the molecular packing interface that forms along the fibrillation axis. Our data suggests that there is a potent inhibitor rather than being required at high copy number relative to Aß42, so one plausible explanation is that the contaminating peptides are responsible for the branches because of slightly different structure leading to altered aggregation kinetics and toxicity. At the end point, the recombinant peptide had completely formed very long linear fibrils. No

evidence of smaller oligomeric material remained suggesting that under our conditions these mature fibrils are the thermodynamically favored. Given their extremely high density, the pure linearity of the fibrils is quite striking and either suggests that fibril formation is unimpeded by contacts with adjacent polymers or that short fibril fragments form as intermediates and later self-assemble into the mature fibrils.

To follow up on the numerous observations correlating toxicity with aggregation dynamics, we compared the peptide samples using the ThT assay. The kinetics of aggregation are set apart by two features of the fluorescent traces. Firstly, the lag time to reach the half-maximal signal, $t_{\frac{1}{2}}$, is about 10% longer in the synthetic reaction indicating alterations to the early aggregation steps. Secondly, the fast-phase aggregation trajectory is less steep for the synthetic Aß42. Together with our EM data, this indicates that the more highly branched fibrils observed in the synthetic sample (Figure 52) form with reduced kinetics when compared to the more linear fibrils of recombinant peptide (Figure 51 and Figure 53).

Whatever the contaminant in the synthetic peptide is, it is not present at high concentration so its ability to alter aggregation dynamics and toxicity is extremely potent. This further suggests a mechanism where single molecules of this inhibitor are capable of disrupting the normal aggregation of long segments of Aß42 perhaps by capping growing strands or causing branches. It is still unclear how this relates to toxicity but the tight connection implies that perhaps the very same

physical attributes of the fibrils somehow mediate the toxicity observed by our assay.

Analytical chromatography and mass spectrometry of the two Aß42 samples (Figure 58 and Figure 59) was not sufficient to indicate the identity of specific contaminants but made it clear that there was a heterogeneous pool of various candidates which may possess the activity we sought. This is consistent with the idea that each phase of synthesis generates unique impurities all of which are present at small fractional amounts in the final product. Most of the contaminants appear within approximately 400 mass units of the main peak by MALDI-TOF MS, corroborating a previous suggestion[121] that they may be byproducts of synthesis related to the majority product. A loss or addition of one to three residues would result in truncated or augmented peptides consistent with the observed sizes of contaminants.

A version of the Aß42 peptide with altered stereochemistry could easily avoid detection and separation by the standard methods used in production, so it seemed a very likely candidate for one of the byproducts. A reversed chiral center would likely alter the specific fold of the peptide and may subtly change the shape such that the altered peptide could still interact via its normal oligomerization interface but somehow reduced the velocity of this event perhaps by putting a kink in the chain. Our ThT assay revealed that Aß42-HIS decelerated the aggregation reaction slightly but was not as potent as the inhibitor we were looking for.

The fractionated peptide sample revealed that the relevant contaminant had higher mobility on the column indicating that it was slightly less hydrophobic than the Aß42 main peak. A loss of a hydrophobic amino acid like valine may be sufficient to illicit this shift, although another likely candidate is I32 which is at another low-efficiency beta-branch dipeptide coupling site. Beyond these two candidates a number of other changes may be able to cause this shift but the chromatography data is consistent with Aß42Δ39 being the relevant contaminant. This is further supported by the peak of mass observed by MALDI-TOF MS approximately 100 Da below the main peak (Figure 59).

Of note in the ESI-MS experiment was the presence of a peak in the recombinant sample of Aß42 dimer. This indicates not only that small oligomers can form under the inhibitory conditions used (1% NH_4OH), but that these oligomers can remain intact through electrospray ionization, trapping and detection. The absence of this peak in the synthetic sample indicates that the inhibitor in that material can reduce formation of dimer as well as larger aggregates and demonstrates that it may functional primarily at the early stages of aggregation.

The potency of aggregation inhibition displayed by Aß42Δ39 is consistent with it being the major contributor to the reduced kinetics observed in the synthetic peptide. A direct prediction of this finding is that Aß42Δ39 would also reduce the toxicity of Aß42, so an immediate next step will be performing the MTT toxicity assay with the doped peptide sample. Another extension of these studies would be to structurally characterize the doped aggregates by EM. We predict that these

peptide samples would show the same branching and curving morphology we observed in the synthetic peptide. We would also like to gain mechanistic insights into the mechanism of inhibition by performing a titration experiment. If inhibition is dose-responsive, it would indicate that the mechanism of inhibition is by directly binding or incorporating into the forming fibril. However, if inhibition is thresholded, it would support another model of inhibition. A competing model would be that Aß42Δ39 peptides induce a non-productive conformation amongst Aß42 molecules similar to the prion protein which would only require a small amount of the altered peptide to seed a misfolding cascade. One way to approach the question of mechanism would be to perform *in silico* experiments mixing the two peptides in molecular dynamics simulations. Many studies have modeled the structure and contacts between aggregating molecules of Aß42 so it should be possible to model the interaction between Aß42Δ39 and Aß42. Such modeling may provide insight into the mechanisms by which Aß42Δ39 inhibits aggregation but may also provide a greater understanding of the connection between aggregation and toxicity of Aß42.

The primary goal of identifying the inhibitor present in synthetic Aß42 was to develop therapeutics which may help AD patients. The next step in this effort is to test Aß42Δ39 in a mouse model to look for real *in vivo* effects. Molecular modeling may also indicate rational modifications of Aß42Δ39 or even smaller peptide fragments which may be more potent. Peptide fragments may be small enough to serve as viable drug candidates which could pass from the blood stream into the

brain where they are needed, which would make them a powerful tool in the treatment of AD.

CONCLUSION

We have found that manufacture of synthetic Aß42 generates contaminating byproducts that inhibit Aß42 aggregation. We have also identified Aß42Δ39 as a potent agent of this inhibition. To a lesser extent, another suggested contaminant, Aß42-HIS, also exhibited some inhibition of aggregation. Based on the correlation between Aß42 toxicity and aggregation kinetics, we propose that Aß42Δ39 and perhaps Aß42-HIS may exhibit neuroprotective activity in AD models. Cell-based assays will reveal whether treatment with Aß42Δ39 or Aß42-HIS can serve to attenuate Aß42 toxicity, possibly yielding an important new class of compounds for therapeutic intervention in Alzheimer's disease.

ACKNOWLEDGMENTS AND ATTRIBUTIONS

All HPLC experiments were performed at AmideBio, LLC with the assistance of Travis Nemkov there. I'd like to thank Christopher Ebmeier for assistance with optimizing trypsin digestion and subsequent purification and analysis of Aß42. ESI-Orbitrap MS was performed by Michael Stowell and William Old. Finally I'd like to thank John Mayer of Lilly Pharmaceuticals for helpful discussion and particularly for the insight to go after Aß42Δ39 as a likely synthesis byproduct.

METHODS

ANIMALS

All animal procedures were carried out in accordance with protocols approved by the IACUC at CU Boulder and the Animal Welfare Assurance filed with OLAW. B6 mice (Jax) were used as WT in all experiments. *SYP* -/- animals[11] were a gift of R. Leube at RWTH Aachen University.

SYNAPTOSOMES

Whole brains were obtained from age-matched female B6 and *SYP* -/- adults. Brains were homogenized 13 strokes on ice in 4 mL of sucrose buffer (10 mM HEPES pH 7.4, 320 mM sucrose, 2 mM EGTA, 2mM EDTA) with protease inhibitor cocktail (Roche) and homogenates were cleared at 4 °C at 1000 g for 10 minutes. Synaptosomes were pelleted at 10,000 g at 4 °C for 20 minutes, resuspended in buffer (25 mM HEPES pH 7.4, 150 mM NaCl, 10 mM $MgCl_2$, 1 mM EDTA, 1% glycerol) and total protein was quantified with the Pierce 660 nM Protein Assay kit.

AB42 COLUMN

AminoLink resin (Pierce) was functionalized according to manufacturer specifications with BioPure™ recombinant Aβ42 or scrambled Aβ42 (AmideBio). Whole brain synaptosomes from B6 or *SYP* -/- mice were applied to column overnight at 4 °C in IP buffer (25 mM HEPES pH 7.4, 150 mM NaCl, 10 mM $MgCl_2$, 1 mM EDTA, 1% glycerol, 0.5% NP-40) with protease inhibitor cocktail (Roche). Beads were washed three times and bound material was eluted at 95 °C in 2X SDS sample buffer.

ANTIBODIES

Antibodies were obtained from Synaptic Systems (SYP, VAMP2, MAP2), Santa Cruz Biotechnology (synaptoporin, synaptogyrin1), and Pierce (synaptogyrin1).

SURFACE PLASMON RESONANCE

Binding studies were performed on a Biacore 3000 and a BiOptix 404pi, with similar results. For the Biacore, a CM5 chip was used and for the BiOptix instrument, a CMV150 chip was employed. BioPure™ recombinant Aß42, scrambled Aß42, or A Aß42-1 (AmideBio) was dissolved to 0.1mM in 10mM sodium hydroxide, and diluted to 1uM in 10mM sodium acetate pH 4.0 immediately prior to immobilization using EDC-NHS chemistry. Recombinant human SYP, containing a His(6)-tag expressed in insect cells, was a gift of J. Mapes and A. DeFazio at CU Boulder. Bovine serum albumin (Sigma), Interleukin 1 receptor antagonist (gift of Synergen, Inc.), and SLC35F1 (gift of G. Chang, UCSD) were used as control proteins. Binding at a flow rate of 20µl/min was in 0.15M sodium chloride, 0.03M sodium HEPES, pH 7.4, 0.009% Fos-choline 14 (Anatrace) for all samples.

DENSITOMETRY

Relative protein quantifications were performed with the gel analysis tool packaged with ImageJ. Measurements were taken in triplicate and averaged. Values of co-precipitated protein were normalized to levels of recovered bait protein and shown as a ratio over samples treated with scrambled Aß42.

CELL CULTURE

Cortical neurons were prepared as described previously[138] and plated at high density (~5000 cells/mm^2) to ensure physiologically relevant synaptic connections. Imaging was performed at 12 - 15 DIV. Neurons were treated with 13 nM Aß42 or scrambled peptide (R Peptide) 24 hours prior to imaging. No difference was observed between scrambled peptide and vehicle.

FM 1-43 Assay: Neurons were labeled with 10 μM FM 1-43 (Invitrogen) in stimulating buffer (25 mM HEPES pH 7.4, 59 mM NaCl, 70 mM KCl, 2 mM $CaCl_2$, 1 mM $MgCl_2$, 30 mM glucose) for 2 minutes at 37 °C followed by washing in a calcium-depleted buffer (25 mM HEPES pH 7.4, 124 mM NaCl, 5 mM KCl, 0.2 mM $CaCl_2$, 5 mM $MgCl_2$, 30 mM glucose) to prevent release of labeled vesicles prior to assay. Cultures were depolarized under profusion with stimulating buffer and imaged for 60 seconds after onset of release. Synaptic puncta were identified in ImageJ[68] by making a max projection of the video, background subtraction of 0.5*mean pixel intensity and finding local maxima on a 10 px (~650 nm) radius with the NEMO-derived[139] ImageJ plugin 3D Fast Filter. These maps were enlarged over a 5 px radius and mean grey value of each punctum was plotted against time. Each unloading curve was fitted to an exponential decay equation of the form $f(t) = f_0 \cdot e^{\left(\frac{-1}{\tau}\right)\cdot t} + c$ to determine a time constant, τ, to represent the kinetics of release at each synapse. These data were filtered for particles whose behavior poorly fit an exponential model (R^2<0.95) and the data presented was trimmed to values of τ between 0 and 500 seconds, although a small number of extremely slow decay events were observed. The remaining values were sorted into

5 second bins and displayed as a histogram. Each bin represents the sum of all biological replicates at each τ value normalized to the mode of each distribution.

SEQUENCE ALIGNMENTS

Human sequences of SYP and homologs were obtained from the uniprot database (uniprot.org). Paralog tree was produced with the simple analysis tool from phylogeny.fr. ClustalW alignment was performed with gap penalties 12 open and 1 extension and aligned with PSI-BLAST at 3 iterations and an E-value cutoff of 0.01. This alignment was assigned a similarity score at each position by the PRALINE server using the BLOSUM62 matrix. The conservation scores were presented at each position as a moving average over a 3 residue window to smooth the plot. The query sequence (hSYP) was then analyzed for hydropathy using the ExPASy ProtScale tool with the Kyte & Doolittle algorithm at a window size of 19 residues.

IMMUNOPRECIPITATION

Five µg of precipitating antibody was bound to PureProteome protein A magnetic beads (Millipore) in IP buffer for 10 minutes and the beads were washed. Whole brain synaptosomes were applied in IP buffer with protease inhibitor cocktail (Roche) overnight at 4 °C. Beads were washed thrice in IP buffer and bound material was eluted at 95 °C in 2X SDS sample buffer.

SYP/VAMP2 PURIFICATION

SVs were prepared from frozen calf brain as described previously[5]. Purified SVs were incubated for 30 minutes at 0° C (at 5 mg/ml) in a solution containing 5

mM NaH_2PO_4 (pH6.8), 0.2% Triton X-100 (w/v) and 1% cholesterol. The Triton extract was centrifuged at 45,000*g* for 30 minutes at 4° C. Triton supernatant was applied to a dry hydroxyapatite/celite column (2:1 w/w) (0.1 g/mg protein) and eluted with solubilization buffer. The resin bound proteins were eluted and found to contain no SYP. The SYP/VAMP2 containing flow through was applied to a POROS H10 anion-exchange column and eluted using a NaCl gradient from 0-1 M (20 mM NaH_2PO_4 (pH6.8), 0.2% Brij-35, 0.1% Cholesterol, 40 mM sucrose). 1 ml fractions were collected and analyzed using SDS-PAGE. Fractions containing SYP/VAMP2 were pooled and applied to a Hi-Prep Sephacryl S-300 size-exclusion column. Protein was eluted using 20 mM NaH_2PO_4 (pH6.8), 0.2% Brij-35, 0.1% Cholesterol, 40 mM sucrose. Fractions were analyzed using SDS-PAGE and western blotting. Blots were probed with monoclonal SYP and VAMP2 antibodies and fractions of purified SYP/VAMP2 were combined and utilized for EM analysis. The SYP/VAMP2 complex eluted with an apparent molecular weight of ~400kD.

ELECTRON MICROSCOPY (SYP/VAMP2)

Imaging was performed as described previously.[5] The final model was a result of 8 rounds of refinement and contained 1232 particles. The resolution of the final model was calculated to be ~28 Å based on FSC using a standard cutoff of 0.5. The absolute hand of the structure was not determined experimentally but was placed in the same hand as the previous SYP structure[5].

STRUCTURAL ALIGNMENT AND FITTING

The SYP sequence was aligned with the connexin26 sequence based upon a hydropathy window using AlignMe. The aligned sequences were then used in Medeller either as the core SYP 21-220 or the full length sequence as the target and connexin as the template. The new model was then dynamically fit to the map using the AD-ENM EMFF web server. This Cα model was then run through the rotamer search program MaxSprout to place side chains. Finally, the model was minimized using the 3D refine server.

Aß42 and Related Peptides

Peptides were sourced from rPeptide, Bachem, genscript and were prepared in 10 mM NaOH. Quantification was performed by BCA assay (Pierce) to determine the ε_{280} which was used for further quantification.

MTT Toxicity Assay

Cell survival was assayed with the (MTT) method. Undifferentiated PC12 cells (ATCC) were plated at a density of 20,000 cells/well in a clear-bottom 96-well culture plate. At 24 hours after plating, a peptide or vehicle was added to cells. At 48 hours after plating, MTT (Promega) was added to cells and developed according to the specifications of the manufacturer.

Negative Stain Electron Microscopy (Aβ fibrils)

200 mesh copper grids were coated with formvar and sputtered with a carbon coat before being plasma discharged to prepare for sample application. Aß42 samples were applied in 4 µL volume and allowed to adsorb for 60 seconds. Excess liquid was blotted away with filter paper and washed twice. Samples were stained

for 30 seconds with 2% urinal acetate, and then blotted dry with filter paper. Imaging was performed on a Philips CM100.

THT Aggregation Assay

Aggregation of Aß42 fibrils was performed as described previously[121].

Aß42 Chromatography

Aß42 samples were run over a Zorbax SB300 C8 RP-HPLC column at 1mL/min. in 10% acetonitrile/0.1% TFA. Elution at 30.5% acetonitrile in ramp elution at 4 mL/min.

MALDI-TOF Mass Spectrometry

Samples were spotted onto MALDI plates with alpha-Cyano-4-hydroxycinnamic acid. Samples were analyzed on a Voyager-DE STR.

Purification of Tryptic Aß42 Fragments

Aß42 Peptide was solubilized in 50 mM Tris and allowed to digest for 16 hours at 37 °C. Samples were purified using C_4 Zip-Tip (Millipore) according to the specifications of the manufacturer.

ESI-Orbitrap Mass Spectrometry

Aß42 samples were reconstituted in pH 10 NH_4OH at 1mg/mL. Samples were infused at 300 nl/min for nano-electrospray ionization and mass spectrometry analysis performed on a LTQ-Orbitrap (ThermoFisher). Survey scans were collected in the Orbitrap at 60,000 resolution (at m/z=300), and MS/MS sequencing was performed by CAD in the LTQ. The maximum injection time for MS survey scans was 500 ms with 1 microscan and AGC= $1x10^6$. For LTQ MS/MS scans, maximum injection time for survey scans was 250 ms with 1 microscan and AGC= $1x10^6$.

Peptides were fragmented by CAD for 30 ms in 1 mTorr of N_2 with a normalized collision energy of 35% and activation Q=0.25.

REFERENCES

1. Herculano-Houzel, S. The human brain in numbers: a linearly scaled-up primate brain. *Front Hum Neurosci* **3,** 31 (2009).
2. Roth, G. & Dicke, U. Evolution of the brain and intelligence. *Trends Cogn. Sci. (Regul. Ed.)* **9,** 250–257 (2005).
3. Azevedo, F. A. C. *et al.* Equal numbers of neuronal and nonneuronal cells make the human brain an isometrically scaled-up primate brain. *J. Comp. Neurol.* **513,** 532–541 (2009).
4. Gao, Y. *et al.* Single reconstituted neuronal SNARE complexes zipper in three distinct stages. *Science* **337,** 1340–1343 (2012).
5. Arthur, C. P. & Stowell, M. H. B. Structure of Synaptophysin: A Hexameric MARVEL-Domain Channel Protein. *Structure* **15,** 707–714 (2007).
6. Wiedenmann, B. & Franke, W. W. Identification and localization of synaptophysin, an integral membrane glycoprotein of Mr 38,000 characteristic of presynaptic vesicles. *Cell* **41,** 1017–1028 (1985).
7. Jahn, R., Schiebler, W., Ouimet, C. & Greengard, P. A 38,000-dalton membrane protein (p38) present in synaptic vesicles. *Proc. Natl. Acad. Sci. U.S.A.* **82,** 4137–4141 (1985).
8. Kwon, S. E. & Chapman, E. R. Glycosylation is dispensable for sorting of synaptotagmin 1 but is critical for targeting of SV2 and synaptophysin to recycling synaptic vesicles. *J. Biol. Chem.* **287,** 35658–35668 (2012).
9. Evans, G. J. O. & Cousin, M. A. Tyrosine phosphorylation of synaptophysin in synaptic vesicle recycling. *Biochemical Society Transactions* **33,** 1350 (2005).
10. Gincel, D. & Shoshan-Barmatz, V. The synaptic vesicle protein synaptophysin: purification and characterization of its channel activity. *Biophysical journal* **83,** 3223–3229 (2002).
11. Eshkind, L. G. & Leube, R. E. Mice lacking synaptophysin reproduce and form typical synaptic vesicles. *Cell Tissue Res.* **282,** 423–433 (1995).
12. Abraham, C. *et al.* Synaptic tetraspan vesicle membrane proteins are conserved but not needed for synaptogenesis and neuronal function in Caenorhabditis elegans. *Proc. Natl. Acad. Sci. U.S.A.* **103,** 8227–8232 (2006).
13. Takamori, S. *et al.* Molecular Anatomy of a Trafficking Organelle. *Cell* **127,** 831–846 (2006).
14. Janz, R. *et al.* Essential Roles in Synaptic Plasticity for Synaptogyrin I and Synaptophysin I. *Neuron* **24,** 687–700 (1999).
15. Spiwoks-Becker, I. *et al.* Synaptic vesicle alterations in rod photoreceptors of synaptophysin-deficient mice. *Neuroscience* **107,** 127–142 (2001).
16. Schmitt, U., Tanimoto, N., Seeliger, M., Schaeffel, F. & Leube, R. E. Detection of behavioral alterations and learning deficits in mice lacking synaptophysin. *Neuroscience* **162,** 234–243 (2009).

17. Kwon, S. E. & Chapman, E. R. Synaptophysin regulates the kinetics of synaptic vesicle endocytosis in central neurons. *Neuron* **70,** 847–854 (2011).
18. Edelmann, L., Hanson, P. I., Chapman, E. R. & Jahn, R. Synaptobrevin binding to synaptophysin: a potential mechanism for controlling the exocytotic fusion machine. *EMBO J* **14,** 224–231 (1995).
19. Calakos, N. & Scheller, R. H. Vesicle-associated membrane protein and synaptophysin are associated on the synaptic vesicle. *J. Biol. Chem.* **269,** 24534–24537 (1994).
20. Gordon, S. L., Leube, R. E. & Cousin, M. A. Synaptophysin is required for synaptobrevin retrieval during synaptic vesicle endocytosis. *J. Neurosci.* **31,** 14032–14036 (2011).
21. Schoch, S. *et al.* SNARE function analyzed in synaptobrevin/VAMP knockout mice. *Science* **294,** 1117–1122 (2001).
22. Deák, F., Schoch, S., Liu, X., Südhof, T. C. & Kavalali, E. T. Synaptobrevin is essential for fast synaptic-vesicle endocytosis. *Nat. Cell Biol.* **6,** 1102–1108 (2004).
23. Gordon, S. L. & Cousin, M. A. The sybtraps: Control of synaptobrevin traffic by synaptophysin, α-synuclein and AP180. *Traffic* (2013). doi:10.1111/tra.12140
24. Peterson, K. J. *et al.* Estimating metazoan divergence times with a molecular clock. *Proc. Natl. Acad. Sci. U.S.A.* **101,** 6536–6541 (2004).
25. DE ROBERTIS, E. D. & BENNETT, H. S. Some features of the submicroscopic morphology of synapses in frog and earthworm. *J Biophys Biochem Cytol* **1,** 47–58 (1955).
26. PALAY, S. L. Synapses in the central nervous system. *J Biophys Biochem Cytol* **2,** 193–202 (1956).
27. Betz, W. J. & Bewick, G. S. Optical analysis of synaptic vesicle recycling at the frog neuromuscular junction. *Science* **255,** 200–203 (1992).
28. Betz, W. J., Mao, F. & Bewick, G. S. Activity-dependent fluorescent staining and destaining of living vertebrate motor nerve terminals. *J. Neurosci.* **12,** 363–375 (1992).
29. Betz, W. J. & Bewick, G. S. Optical monitoring of transmitter release and synaptic vesicle recycling at the frog neuromuscular junction. *J. Physiol. (Lond.)* **460,** 287–309 (1993).
30. Miesenböck, G., De Angelis, D. A. & Rothman, J. E. Visualizing secretion and synaptic transmission with pH-sensitive green fluorescent proteins. *Nature* **394,** 192–195 (1998).
31. Pennuto, M., Bonanomi, D., Benfenati, F. & Valtorta, F. Synaptophysin I controls the targeting of VAMP2/synaptobrevin II to synaptic vesicles. *Molecular biology of the cell* **14,** 4909 (2003).
32. Möller, C. *et al.* Different patterns of gray matter atrophy in early- and late-onset Alzheimer's disease. *Neurobiol. Aging* **34,** 2014–2022 (2013).
33. Alzheimer's Association. *Alzheimer's Association* at <http://www.alz.org/index.asp>

34. Karran, E., Mercken, M. & De Strooper, B. The amyloid cascade hypothesis for Alzheimer's disease: an appraisal for the development of therapeutics. *Nat Rev Drug Discov* **10,** 698–712 (2011).
35. About Alzheimer's Disease: Diagnosis. *National Institute on Aging* at <http://www.nia.nih.gov/alzheimers/topics/diagnosis>
36. Tanzi, R. E. The genetics of Alzheimer disease. *Cold Spring Harb Perspect Med* **2,** (2012).
37. Alzheimer's Association. 2010 Alzheimer's disease facts and figures. *Alzheimer's & Dementia: The Journal of the Alzheimer's Association* **6,** 158–194 (2010).
38. Tejada-Vera, B. Mortality from Alzheimer's disease in the United States: data for 2000 and 2010. *NCHS Data Brief* 1–8 (2013).
39. Lopez, O. L. The growing burden of Alzheimer's disease. *Am J Manag Care* **17 Suppl 13,** S339–345 (2011).
40. Mayeux, R. & Stern, Y. Epidemiology of Alzheimer disease. *Cold Spring Harb Perspect Med* **2,** (2012).
41. Hardy, J. & Allsop, D. Amyloid deposition as the central event in the aetiology of Alzheimer's disease. *Trends Pharmacol. Sci.* **12,** 383–388 (1991).
42. Berezovska, O. *et al.* Familial Alzheimer's disease presenilin 1 mutations cause alterations in the conformation of presenilin and interactions with amyloid precursor protein. *J. Neurosci.* **25,** 3009–3017 (2005).
43. Lai, F. & Williams, R. S. A prospective study of Alzheimer disease in Down syndrome. *Arch. Neurol.* **46,** 849–853 (1989).
44. Hall, A. M. & Roberson, E. D. Mouse models of Alzheimer's disease. *Brain Res. Bull.* (2011). doi:10.1016/j.brainresbull.2011.11.017
45. Davis, R. C. *et al.* Amyloid beta dimers/trimers potently induce cofilin-actin rods that are inhibited by maintaining cofilin-phosphorylation. *Mol Neurodegener* **6,** 10 (2011).
46. Reifert, J., Hartung-Cranston, D. & Feinstein, S. C. Amyloid beta-mediated cell death of cultured hippocampal neurons reveals extensive Tau fragmentation without increased full-length tau phosphorylation. *J. Biol. Chem.* **286,** 20797–20811 (2011).
47. Shankar, G. M. *et al.* Amyloid-beta protein dimers isolated directly from Alzheimer's brains impair synaptic plasticity and memory. *Nat. Med.* **14,** 837–842 (2008).
48. Cleary, J. P. *et al.* Natural oligomers of the amyloid-beta protein specifically disrupt cognitive function. *Nat. Neurosci* **8,** 79–84 (2005).
49. Price, J. L. *et al.* Neuropathology of nondemented aging: presumptive evidence for preclinical Alzheimer disease. *Neurobiol. Aging* **30,** 1026–1036 (2009).
50. Walsh, D. M. & Selkoe, D. J. A beta oligomers - a decade of discovery. *J. Neurochem.* **101,** 1172–1184 (2007).
51. Ono, K. & Yamada, M. Low-n oligomers as therapeutic targets of Alzheimer's disease. *J. Neurochem.* **117,** 19–28 (2011).

52. Dahlgren, K. N. *et al.* Oligomeric and fibrillar species of amyloid-beta peptides differentially affect neuronal viability. *J. Biol. Chem.* **277,** 32046–32053 (2002).
53. Enya, M. *et al.* Appearance of sodium dodecyl sulfate-stable amyloid beta-protein (Abeta) dimer in the cortex during aging. *Am. J. Pathol.* **154,** 271–279 (1999).
54. Freir, D. B. *et al.* Aß oligomers inhibit synapse remodelling necessary for memory consolidation. *Neurobiol. Aging* **32,** 2211–2218 (2011).
55. Gervais, F. *et al.* Targeting soluble Abeta peptide with Tramiprosate for the treatment of brain amyloidosis. *Neurobiol. Aging* **28,** 537–547 (2007).
56. Haass, C. & Selkoe, D. J. Soluble protein oligomers in neurodegeneration: lessons from the Alzheimer's amyloid beta-peptide. *Nat. Rev. Mol. Cell Biol.* **8,** 101–112 (2007).
57. Hartley, D. M. *et al.* Protofibrillar intermediates of amyloid beta-protein induce acute electrophysiological changes and progressive neurotoxicity in cortical neurons. *J. Neurosci.* **19,** 8876–8884 (1999).
58. Hsia, A. Y. *et al.* Plaque-independent disruption of neural circuits in Alzheimer's disease mouse models. *Proc. Natl. Acad. Sci. U.S.A.* **96,** 3228–3233 (1999).
59. Hu, N.-W., Smith, I. M., Walsh, D. M. & Rowan, M. J. Soluble amyloid-beta peptides potently disrupt hippocampal synaptic plasticity in the absence of cerebrovascular dysfunction in vivo. *Brain* **131,** 2414–2424 (2008).
60. Klein, W. L., Stine, W. B., Jr & Teplow, D. B. Small assemblies of unmodified amyloid beta-protein are the proximate neurotoxin in Alzheimer's disease. *Neurobiol. Aging* **25,** 569–580 (2004).
61. Li, S. *et al.* Soluble Oligomers of Amyloid ß Protein Facilitate Hippocampal Long-Term Depression by Disrupting Neuronal Glutamate Uptake. *Neuron* **62,** 788–801 (2009).
62. Deshpande, A., Mina, E., Glabe, C. & Busciglio, J. Different conformations of amyloid beta induce neurotoxicity by distinct mechanisms in human cortical neurons. *J. Neurosci.* **26,** 6011–6018 (2006).
63. Catalano, S. M. *et al.* The role of amyloid-beta derived diffusible ligands (ADDLs) in Alzheimer's disease. *Curr Top Med Chem* **6,** 597–608 (2006).
64. Laurén, J., Gimbel, D. A., Nygaard, H. B., Gilbert, J. W. & Strittmatter, S. M. Cellular prion protein mediates impairment of synaptic plasticity by amyloid-beta oligomers. *Nature* **457,** 1128–1132 (2009).
65. Lacor, P. N. *et al.* Abeta oligomer-induced aberrations in synapse composition, shape, and density provide a molecular basis for loss of connectivity in Alzheimer's disease. *J. Neurosci.* **27,** 796–807 (2007).
66. Kim, T. *et al.* Human LilrB2 is a ß-amyloid receptor and its murine homolog PirB regulates synaptic plasticity in an Alzheimer's model. *Science* **341,** 1399–1404 (2013).

67. Li, S., Shankar, G. M. & Selkoe, D. J. How do Soluble Oligomers of Amyloid ß protein Impair Hippocampal Synaptic Plasticity? *Frontiers in Cellular Neuroscience* **4,** (2010).
68. Schneider, C. A., Rasband, W. S. & Eliceiri, K. W. NIH Image to ImageJ: 25 years of image analysis. *Nat Meth* **9,** 671–675 (2012).
69. Ryan, T. A. & Smith, S. J. Vesicle pool mobilization during action potential firing at hippocampal synapses. *Neuron* **14,** 983–989 (1995).
70. Walch-Solimena, C. *et al.* The t-SNAREs syntaxin 1 and SNAP-25 are present on organelles that participate in synaptic vesicle recycling. *J. Cell Biol.* **128,** 637–645 (1995).
71. Van Spronsen, M. & Hoogenraad, C. C. Synapse pathology in psychiatric and neurologic disease. *Curr Neurol Neurosci Rep* **10,** 207–214 (2010).
72. Tackenberg, C. & Brandt, R. Divergent pathways mediate spine alterations and cell death induced by amyloid-beta, wild-type tau, and R406W tau. *J. Neurosci.* **29,** 14439–14450 (2009).
73. Milnerwood, A. J. & Raymond, L. A. Early synaptic pathophysiology in neurodegeneration: insights from Huntington's disease. *Trends Neurosci.* **33,** 513–523 (2010).
74. Sze, C. I. *et al.* Loss of the presynaptic vesicle protein synaptophysin in hippocampus correlates with cognitive decline in Alzheimer disease. *J. Neuropathol. Exp. Neurol.* **56,** 933–944 (1997).
75. Sze, C. I., Bi, H., Kleinschmidt-DeMasters, B. K., Filley, C. M. & Martin, L. J. Selective regional loss of exocytotic presynaptic vesicle proteins in Alzheimer's disease brains. *J. Neurol. Sci.* **175,** 81–90 (2000).
76. Reddy, P. H. *et al.* Differential loss of synaptic proteins in Alzheimer's disease: implications for synaptic dysfunction. *J. Alzheimers Dis.* **7,** 103–117; discussion 173–180 (2005).
77. Johnston, P. A., Jahn, R. & Südhof, T. C. Transmembrane topography and evolutionary conservation of synaptophysin. *J. Biol. Chem.* **264,** 1268–1273 (1989).
78. Thomas, L. *et al.* Identification of synaptophysin as a hexameric channel protein of the synaptic vesicle membrane. *Science* **242,** 1050–1053 (1988).
79. Marquèze-Pouey, B., Wisden, W., Malosio, M. L. & Betz, H. Differential expression of synaptophysin and synaptoporin mRNAs in the postnatal rat central nervous system. *J. Neurosci.* **11,** 3388–3397 (1991).
80. Spiwoks-Becker, I. *et al.* Synaptic vesicle alterations in rod photoreceptors of synaptophysin-deficient mice. *Neuroscience* **107,** 127–142 (2001).
81. Russell, C. L. *et al.* Amyloid-ß Acts as a Regulator of Neurotransmitter Release Disrupting the Interaction between Synaptophysin and VAMP2. *PLoS ONE* **7,** e43201 (2012).
82. Gordon, S. L. & Cousin, M. A. X-Linked Intellectual Disability-Associated Mutations in Synaptophysin Disrupt Synaptobrevin II Retrieval. *J. Neurosci.* **33,** 13695–13700 (2013).

83. McMahon, H. T. *et al.* Synaptophysin, a major synaptic vesicle protein, is not essential for neurotransmitter release. *Proc. Natl. Acad. Sci. U.S.A.* **93,** 4760–4764 (1996).
84. Becher, A. *et al.* The synaptophysin-synaptobrevin complex: a hallmark of synaptic vesicle maturation. *J. Neurosci* **19,** 1922–1931 (1999).
85. Laage, R. & Langosch, D. Dimerization of the synaptic vesicle protein synaptobrevin (vesicle-associated membrane protein) II depends on specific residues within the transmembrane segment. *Eur. J. Biochem.* **249,** 540–546 (1997).
86. Sternberg, M. J. Inter-species sequence conservation of single-spanning transmembrane regions. *Protein Eng.* **4,** 45–47 (1990).
87. Maeda, S. *et al.* Structure of the connexin 26 gap junction channel at 3.5 A resolution. *Nature* **458,** 597–602 (2009).
88. Ellena, J. F. *et al.* Dynamic structure of lipid-bound synaptobrevin suggests a nucleation-propagation mechanism for trans-SNARE complex formation. *Proc. Natl. Acad. Sci. U.S.A.* **106,** 20306–20311 (2009).
89. Mitter, D. *et al.* The synaptophysin/synaptobrevin interaction critically depends on the cholesterol content. *Journal of Neurochemistry* **84,** 35–42 (2003).
90. Dason, J. S., Smith, A. J., Marin, L. & Charlton, M. P. Vesicular sterols are essential for synaptic vesicle cycling. *J. Neurosci.* **30,** 15856–15865 (2010).
91. Sponne, I. *et al.* Membrane cholesterol interferes with neuronal apoptosis induced by soluble oligomers but not fibrils of amyloid-beta peptide. *FASEB J.* **18,** 836–838 (2004).
92. Puglielli, L. *et al.* Alzheimer disease beta-amyloid activity mimics cholesterol oxidase. *J. Clin. Invest.* **115,** 2556–2563 (2005).
93. Kam, T.-I. *et al.* FcγRIIb mediates amyloid-ß neurotoxicity and memory impairment in Alzheimer's disease. *J. Clin. Invest.* **123,** 2791–2802 (2013).
94. Lue, L. F. *et al.* Soluble amyloid beta peptide concentration as a predictor of synaptic change in Alzheimer's disease. *Am. J. Pathol.* **155,** 853–862 (1999).
95. Zampighi, G. A. *et al.* Conical electron tomography of a chemical synapse: vesicles docked to the active zone are hemi-fused. *Biophys. J.* **91,** 2910–2918 (2006).
96. Moreno, H. *et al.* Synaptic transmission block by presynaptic injection of oligomeric amyloid beta. *Proc. Natl. Acad. Sci. U.S.A.* **106,** 5901–5906 (2009).
97. Parodi, J. *et al.* Beta-Amyloid Causes Depletion of Synaptic Vesicles Leading to Neurotransmission Failure. *Journal of Biological Chemistry* **285,** 2506–2514 (2009).
98. Zhou, P., Bacaj, T., Yang, X., Pang, Z. P. & Südhof, T. C. Lipid-Anchored SNAREs Lacking Transmembrane Regions Fully Support Membrane Fusion during Neurotransmitter Release. *Neuron* doi:10.1016/j.neuron.2013.09.010
99. Van den Bogaart, G. *et al.* One SNARE complex is sufficient for membrane fusion. *Nat. Struct. Mol. Biol.* **17,** 358–364 (2010).

100. Keller, J. E., Cai, F. & Neale, E. A. Uptake of botulinum neurotoxin into cultured neurons. *Biochemistry* **43,** 526–532 (2004).
101. Domanska, M. K., Kiessling, V., Stein, A., Fasshauer, D. & Tamm, L. K. Single vesicle millisecond fusion kinetics reveals number of SNARE complexes optimal for fast SNARE-mediated membrane fusion. *J. Biol. Chem.* **284,** 32158–32166 (2009).
102. Karatekin, E. *et al.* A fast, single-vesicle fusion assay mimics physiological SNARE requirements. *Proc. Natl. Acad. Sci. U.S.A.* **107,** 3517–3521 (2010).
103. Szule, J. A. *et al.* Regulation of synaptic vesicle docking by different classes of macromolecules in active zone material. *PLoS ONE* **7,** e33333 (2012).
104. Mohrmann, R., de Wit, H., Verhage, M., Neher, E. & Sørensen, J. B. Fast vesicle fusion in living cells requires at least three SNARE complexes. *Science* **330,** 502–505 (2010).
105. He, L., Wu, X.-S., Mohan, R. & Wu, L.-G. Two modes of fusion pore opening revealed by cell-attached recordings at a synapse. *Nature* **444,** 102–105 (2006).
106. Sabatini, B. L. & Regehr, W. G. Timing of neurotransmission at fast synapses in the mammalian brain. *Nature* **384,** 170–172 (1996).
107. Tarpey, P. S. *et al.* A systematic, large-scale resequencing screen of X-chromosome coding exons in mental retardation. *Nat. Genet.* **41,** 535–543 (2009).
108. Murray, D. H. & Tamm, L. K. Molecular mechanism of cholesterol- and polyphosphoinositide-mediated syntaxin clustering. *Biochemistry* **50,** 9014–9022 (2011).
109. Sieber, J. J. *et al.* Anatomy and dynamics of a supramolecular membrane protein cluster. *Science* **317,** 1072–1076 (2007).
110. Cho, W. J., Jeremic, A., Jin, H., Ren, G. & Jena, B. P. Neuronal fusion pore assembly requires membrane cholesterol. *Cell Biol. Int.* **31,** 1301–1308 (2007).
111. Galli, T., McPherson, P. S. & Camilli, P. D. The V Sector of the V-ATPase, Synaptobrevin, and Synaptophysin Are Associated on Synaptic Vesicles in a Triton X-100-resistant, Freeze-thawing Sensitive, Complex. *J. Biol. Chem.* **271,** 2193–2198 (1996).
112. Kiessling, V. *et al.* Rapid fusion of synaptic vesicles with reconstituted target SNARE membranes. *Biophys. J.* **104,** 1950–1958 (2013).
113. Lai, A. Y. & McLaurin, J. Mechanisms of Amyloid-Beta Peptide Uptake by Neurons: The Role of Lipid Rafts and Lipid Raft-Associated Proteins. *International Journal of Alzheimer's Disease* **2011,** (2010).
114. Tiraboschi, P. *et al.* The decline in synapses and cholinergic activity is asynchronous in Alzheimer's disease. *Neurology* **55,** 1278–1283 (2000).
115. Kelly, B. L. & Ferreira, A. Beta-amyloid disrupted synaptic vesicle endocytosis in cultured hippocampal neurons. *Neuroscience* **147,** 60–70 (2007).
116. Park, J., Jang, M. & Chang, S. Deleterious effects of soluble amyloid-ß oligomers on multiple steps of synaptic vesicle trafficking. *Neurobiology of Disease* **55,** 129–139 (2013).

117. Seeman, P. & Seeman, N. Alzheimer's disease: ß-amyloid plaque formation in human brain. *Synapse* **65,** 1289–1297 (2011).
118. Giuffrida, M. L. *et al.* The monomer state of beta-amyloid: where the Alzheimer's disease protein meets physiology. *Rev Neurosci* **21,** 83–93 (2010).
119. Hardy, J. & Selkoe, D. J. The amyloid hypothesis of Alzheimer's disease: progress and problems on the road to therapeutics. *Science* **297,** 353–356 (2002).
120. Masters, C. L. & Selkoe, D. J. Biochemistry of amyloid ß-protein and amyloid deposits in Alzheimer disease. *Cold Spring Harb Perspect Med* **2,** a006262 (2012).
121. Finder, V. H., Vodopivec, I., Nitsch, R. M. & Glockshuber, R. The Recombinant Amyloid-[beta] Peptide A [beta] 1-42 Aggregates Faster and Is More Neurotoxic than Synthetic A [beta] 1-42. *Journal of molecular biology* **396,** 9–18 (2010).
122. Biancalana, M. & Koide, S. Molecular mechanism of Thioflavin-T binding to amyloid fibrils. *Biochim. Biophys. Acta* **1804,** 1405–1412 (2010).
123. Fonte, V. *et al.* A glycine zipper motif mediates the formation of toxic ß-amyloid oligomers in vitro and in vivo. *Mol Neurodegener* **6,** 61 (2011).
124. Hung, L. W. *et al.* Amyloid-beta peptide (Abeta) neurotoxicity is modulated by the rate of peptide aggregation: Abeta dimers and trimers correlate with neurotoxicity. *J. Neurosci.* **28,** 11950–11958 (2008).
125. Kim, S. *et al.* Transmembrane glycine zippers: physiological and pathological roles in membrane proteins. *Proc. Natl. Acad. Sci. U.S.A.* **102,** 14278–14283 (2005).
126. Harmeier, A. *et al.* Role of amyloid-beta glycine 33 in oligomerization, toxicity, and neuronal plasticity. *J. Neurosci.* **29,** 7582–7590 (2009).
127. Amyloid Beta Products. at <http://www.amidebio.com/030Products.html>
128. Beta Amyloids: Recombinant, Synthetic, & Labeled Peptides | rPeptide. at <https://www.rpeptide.com/products/beta-amyloid-peptides/>
129. Beta Amyloid (1-42) Recombinant Peptide - NEUROSCIENCE. at <https://store.crpinc.com/datasheet.aspx?catalogno=rPEP-590P>
130. Tickler, A. K., Clippingdale, A. B. & Wade, J. D. Amyloid-beta as a 'difficult sequence' in solid phase peptide synthesis. *Protein Pept. Lett.* **11,** 377–384 (2004).
131. Tickler, A. K., Barrow, C. J. & Wade, J. D. Improved preparation of amyloid-beta peptides using DBU as Nalpha-Fmoc deprotection reagent. *J. Pept. Sci.* **7,** 488–494 (2001).
132. Bacsa, B., Bosze, S. & Kappe, C. O. Direct solid-phase synthesis of the beta-amyloid (1-42) peptide using controlled microwave heating. *J. Org. Chem.* **75,** 2103–2106 (2010).
133. Young, J. D. *et al.* Coupling efficiencies of amino acids in the solid phase synthesis of peptides. *Pept. Res.* **3,** 194–200 (1990).

134. Reiber, D. C., Grover, T. A. & Brown, R. S. Identifying proteins using matrix-assisted laser desorption/ionization in-source fragmentation data combined with database searching. *Anal. Chem.* **70,** 673–683 (1998).
135. Sepulveda, F. J. *et al.* Synaptotoxicity of Alzheimer Beta Amyloid Can Be Explained by Its Membrane Perforating Property. *PloS one* **5,** 789–791 (2010).
136. Hensley, K. *et al.* A model for beta-amyloid aggregation and neurotoxicity based on free radical generation by the peptide: relevance to Alzheimer disease. *PNAS* **91,** 3270–3274 (1994).
137. Shearman, M. S., Hawtin, S. R. & Tailor, V. J. The intracellular component of cellular 3-(4,5-dimethylthiazol-2-yl)-2, 5-diphenyltetrazolium bromide (MTT) reduction is specifically inhibited by beta-amyloid peptides. *J. Neurochem.* **65,** 218–227 (1995).
138. Beaudoin, G. M. J. *et al.* Culturing pyramidal neurons from the early postnatal mouse hippocampus and cortex. *Nature Protocols* **7,** 1741–1754 (2012).
139. Iannuccelli, E. *et al.* NEMO: a tool for analyzing gene and chromosome territory distributions from 3D-FISH experiments. *Bioinformatics* **26,** 696–697 (2010).